学位論文

Formation of hot Jupiters and their spin-orbit evolution

(ホットジュピターの形成とその主星自転・軌道公転角の進化)

平成 28 年 12 月 博士（理学）申請

東京大学大学院理学系研究科
物理学専攻

薛　鈺新

Abstract

Ever since the first discovery of an exoplanet, 51 Pegasi b, hundreds of hot Jupiters (HJs) with Jupiter-size and semi-major axis less than 0.1 AU have been observed around main-sequence stars. Nevertheless, their origin remains one of the important unsolved puzzles in this field.

The first question addressed in this thesis is the formation of HJs. We investigate the formation of HJs in near-coplanar eccentric hierarchical triple systems via the secular interaction between an inner planet and an outer perturber (Coplanar High-eccentricity Migration; CHEM). This mechanism was originally proposed as a unique formation model of counter-orbiting HJs (the spin-orbit angle, the angle between the stellar spin and the planetary orbit axis, $\psi > 160^\circ$). We examine this mechanism in detail by performing a series of systematic numerical simulations, and consider the possibility of forming HJs, especially a counter-orbiting one under this mechanism. We incorporate quadrupole and octupole secular gravitational interaction between the two orbits, and also short-range forces (correction for general relativity, star and inner planetary tide and rotational distortion) simultaneously. We find that most of systems are tidally disrupted and that a small fraction of survived planets turns out to be prograde. The formation of counter-orbiting HJs in this scenario is possible only in a very restricted parameter region, and thus very unlikely in practice. We generalize the previous work on the analytical condition for successful CHEM for point masses interacting only through the gravity by taking into account the finite mass effect of the inner planet. We find that efficient CHEM requires that the systems should have $m_1 \ll m_0$ and $m_1 \ll m_2$. In addition to the gravity for point masses, we examine the importance of the short-range forces, and provide an analytical estimate of the migration timescale. In addition, we extend CHEM to super-Earth mass range, and show that the formation of close-in super-Earths in prograde orbits is also possible. Finally, we carry out CHEM simulation for the observed hierarchical triple and counter-orbiting HJ systems. We find that CHEM can explain a part of the former systems, but it is generally very difficult to reproduce counter-orbiting HJ systems.

The other question addressed in this thesis is the long term spin-orbit angle evolution at the realignment stage. Indeed current observations of the Rossiter-McLaughlin effect have revealed a wide range of spin-orbit misalignments for transiting HJs. We examine in detail the tidal evolution of a simple system comprising a Sun-like star and a hot Jupiter adopting the equilibrium tide and the inertial wave dissipation effects simultaneously (the Lai model). We find that the combined tidal model works as a very efficient realignment

mechanism; it predicts three distinct states of the spin-orbit angle (i.e., aligned, polar, and anti-aligned orbits) for a while, but the latter two states eventually approach the aligned spin-orbit configuration. The intermediate spin-orbit angles as measured in recent observations are difficult to be achieved. Therefore the Lai model cannot reproduce the observed broad distribution of the spin-orbit angles, at least in its simple form. This indicates that the observed diversity of the spin-orbit angles may emerge from more complicated interactions with outer planets and/or may be the consequence of the primordial misalignment between the proto-planetary disk and the stellar spin, which requires future detailed studies.

keywords: planetary migration; dynamical process; tides; numerical simulation

Acknowledgments

This dissertation would not have been possible without the guidance and the help of several individuals who in one way or another contributed and extended their valuable assistance in the preparation and completion of this study. First and foremost, I would like to express my sincere gratitude to my advisor Prof. Yasushi Suto for his incredible support of my study and research, for his patience, motivation, enthusiasm, and immense knowledge. His guidance helped me in all the time of research and writing of this thesis. I could not have finished writing this thesis without him. I am proud of being one of his students. I thank Dr. Kento Masuda for his insightful comments in my work. I thank my other collaborators, Prof. Atsushi Taruya, Dr. Teruyuki Hirano and Dr. Yuka Fujii, for their constructive comments in my work. I thank my family for their supporting throughout my entire life. Finally, I thank my fiancee, Yang Wang, for her encouragement, patient, and support.

Contents

Chapter 1

Introduction

More than 3000[1] exoplanets discovered so far have exhibited a surprising diversity in their physical properties; this diversity provides important observational clues that can be used to unveil their formation and evolution processes. In particular, unexpectedly large fraction of hot Jupiters (giant gas planets orbiting the central star with semi-major axis less than 0.1 AU) is regarded as a serious challenge to conventional models of planet formation that have been proposed to explain the properties of our Solar system. According to the standard core-accretion scenario, such gas giants are supposed to form beyond the ice line in nearly circular orbits. Thus it is widely believed that the discovered hot Jupiters should have formed at a large distance beyond the ice line, and then somehow migrated towards the orbits close to the central star (e.g., Ida & Lin 2004a,b).

The known migration scenarios include disk migration through the interaction with the proto-planetary disk (e.g., Alibert et al. 2005; Lin et al. 1996) and high-e migration, in which planets approach extremely high eccentricities and then suffer from tidal circularization. The possible mechanisms to form HJs in the latter scenario include (1) planet-planet scattering (e.g., Beauge & Nesvorny 2012; Nagasawa et al. 2008; Nagasawa & Ida 2011; Rasio & Ford 1996), (2) the Lidov-Kozai migration (e.g., Anderson et al. 2016; Fabrycky & Tremaine 2007; Kozai 1962; Lidov 1962; Naoz et al. 2011, 2012; Petrovich 2015a; Wu & Murray 2003), and (3) secular chaos (Hamers et al. 2017; Wu & Lithwick 2011).

In reality, each of these different migration mechanisms may have contributed to the observed HJ population to some degree. Each mechanism often predicts a different statistical distribution and correlations of the resulting orbital parameters of the planetary systems, and the relevant observations may provide a potential clue to distinguish different mechanisms. For example, disk migration would imply that gas giants smoothly migrate inward in a gaseous disk and thus the angle, ψ, between the stellar spin and planetary orbital axis would not significantly change from its initial value. In contrast, high-e migration mechanisms mentioned above rely on a dynamical process after the depletion

[1]Data from NASA Exoplanet Archive.

of the gas disk, which can induce a strong spin-orbit misalignment. For this reason, measurement of ψ can be a useful probe in understanding the origin of HJs.

Indeed, the Rossiter-McLaughlin effect has been very successful in measuring the sky projected spin-orbit angle, λ, for ~ 90 transiting planetary systems (McLaughlin 1924; Ohta et al. 2005; Queloz et al. 2000; Rossiter 1924; Winn et al. 2005). Approximately half of the measured systems are well-aligned ($\lambda < \pi/6$), one-third systems exhibit significant misalignment ($\lambda > \pi/4$), a dozen of systems turn out to be retrograde ($\lambda > \pi/2$), and two systems even show counter-orbiting orbits ($\lambda > 160^\circ$); HAT-P-6b with $\lambda = 165^\circ \pm 6^\circ$ (Albrecht et al. 2012) and HAT-P-14b with $\lambda = 189^\circ.1 \pm 5^\circ.1$ (Winn et al. 2011)[2]; see Figure 2.3 for example. Such unexpected and counter-intuitive discoveries imply that those HJs should have experienced violent dynamical processes.

While all three of the above dynamical migration mechanisms could produce retrograde HJs, it has proven difficult to produce counter-orbiting HJs (e.g, Fabrycky & Tremaine 2007; Liu et al. 2015; Naoz et al. 2011; Petrovich 2015b). Therefore, we consider a dynamical model that can theoretically explain counter-orbiting HJs. In chapter 4, we consider yet another possibility of high-e migration mechanism that HJs form via the secular interaction between two orbits in a near-coplanar eccentric hierarchical triple configuration. Throughout this thesis, we refer this HJ formation mechanism to *Coplanar High-eccentricity Migration (CHEM)* following Petrovich (2015b). CHEM is a potentially unique formation model of counter-orbiting HJs that no other model is known to generate. In reality, previous papers indicate that even CHEM may not so easy to produce counter-orbiting HJs. Nevertheless, even if this model is not able to produce count-orbiting HJs efficiently, it also provides a channel to produce prograde HJs. This is why we consider this model with particular emphasis on the application to the observed systems.

As mentioned in the above, CHEM was originally proposed as a potential channel to form counter-orbiting HJs by Li et al. (2014). They pointed out that the interaction due to the outer perturber can increase the eccentricity of the inner planet and flip its orbit by $\sim 180^\circ$. Such a counter-orbiting eccentric planet soon becomes circularized with subsequent tidal dissipation, and is expected to become a counter-orbiting HJ eventually. In particular, they analytically derived an extreme eccentricity condition that the eccentricity of the inner planet reaches unity, which results in its orbital flip. The condition is derived assuming the test particle limit ($m_1 \ll m_0$, $m_1 \ll m_2$), where m_0, m_1, and m_2 are the mass of the central star, inner planet, and outer perturber, respectively. Petrovich (2015b) examined generalized the extreme eccentricity condition on the basis of the conservation of the potential energy in the planetary limit ($m_1 \ll m_0$, $m_1 \leq m_2$) instead of the test particle limit by Li et al. (2014). Also, he performed the numerical simulations of CHEM with a planetary outer perturber, and found that all the resulting HJs have low spin-orbit angles in prograde orbits. The initial conditions of his simulations, how-

[2]The projected spin-orbit angle, λ, differs from the *true* spin-orbit angle, ψ, due to the projection effect. For λ observed via RM effect, $\lambda < \psi$, when $\lambda < 90^\circ$; $\lambda > \psi$, when $\lambda > 90^\circ$. Thus, planetary systems with $\lambda > 160^\circ$ may not be necessarily counter-orbiting, but just retrograde. Indeed, HAT-P-7b has $\lambda > 160^\circ$, but turns out to be not counter-orbiting after the measurement of stellar inclination with asteroseismology (Benomar et al. 2014).

ever, do not cover the relevant parameter space for the expected orbital flip. Therefore, the formation efficiency of counter-orbiting HJs and prograde HJs in CHEM is not clear. The fact motivates us to perform a comprehensive parameter survey for CHEM. Also, the analytical estimates at previous studies neglect the finite mass of the inner planet on the dynamics of the central star and short-range forces (general relativity, stellar and planetary non-dissipative tides, and stellar and planetary rotational distorttion), which may significantly affect the orbital evolution. Furthermore, it is tempting to consider the possibility of CHEM for the formation of observed possible candidate systems.

On the other hand, if the dynamical process is the major path to form hot Jupiters, one may expect that the spin-orbit angle distribution just after the formation of hot Jupiters should be very broad, and even close to random. In order to be consistent with the observed distribution with some overabundance around alignment configuration, a fairly efficient physical process of the *spin-orbit (re)alignment* is required. While the subsequent tidal interaction between the central star and the innermost planet is generally believed to be responsible for the alignment, its detailed model is still unknown. A conventional equilibrium tide model could realign the system, but inevitably accompanies the orbital decay of the planet within a similar timescale (Barker & Ogilvie 2009; Levrard et al. 2009; Matsumura et al. 2010). Therefore a simple equilibrium tide model does not explain the majority of the realigned systems with finite semi-major axis. In order to solve this problem, recently, Lai (2012) proposed a new model in which the damping timescale of the spin-orbit angle could be significantly smaller than that of the planetary orbit. Therefore, in chapter 5, we consider the possibility of the Lai model to explain the spin-orbit angle distribution and examine the tidal evolution of exoplanetary systems on a secular timescale.

The present thesis is organized as follows. In chapter 2, we briefly review the current status on the formation and evolution of hot Jupiters with particular emphasis on Coplanar High-eccentricity Migration (CHEM) and tidal models, and fix definitions of the symbols and terminology used in later chapters. The corresponding basic equations are fully described in chapter 3. We systematically examine the fate of the inner planet in CHEM and its implications both analytically and numerically in chapter 4. This chapter is based on Xue & Suto (2016) and Xue et al. (2016). In chapter 5, we present the spin-orbit evolution and its parameter dependence in the Lai model. This chapter is based on Xue et al. (2014). Finally, chapter 6 is devoted to summary and implications of the present thesis.

Chapter 2

Review on Formation and Evolution of HJs

In this chapter, first we review the migration scenarios of hot Jupiters. Then, we consider the importance of tides and show how they affect the spin and orbital evolution of the hot Jupiters.

2.1 Discovery of the Hot Jupiter

Planetary science had a revolution in 1995 when Mayor & Queloz (1995) detected the first Jupiter-like planet around the sun-like star 51 Pegasi in a four day orbit. Since then, more than 3000 confirmed planets have been detected over the past two decade and their number is quickly increasing (see Figure 2.1).

In our Solar system, all eight planets have low eccentricities; rocky planets like the Earth and Mars are found near the Sun, whereas giant gas planets such as the Jupiter and Saturn are located further away. However, unlike our Solar system, the observed exoplanetary systems exhibit a wide variety of statistical properties. In particular, about 200[1] giant planets with remarkable close-in orbits (semi-major axis less than 0.1 AU), known as "hot Jupiter" (hereafter, HJ), have been observed since the detection of 51 Pegasi b (see Figure 2.1). These are completely different from our Solar system, and thus such unexpected phenomena are particularly interesting in unveiling the formation and evolution of exoplanetary systems.

2.2 Planet Formation

The current understanding of planetary formation theory mainly comes from our Solar system. According to the Solar Nebular hypothesis (e.g., Hayashi 1981), a massive and

[1]Data from NASA Exoplanet Archive.

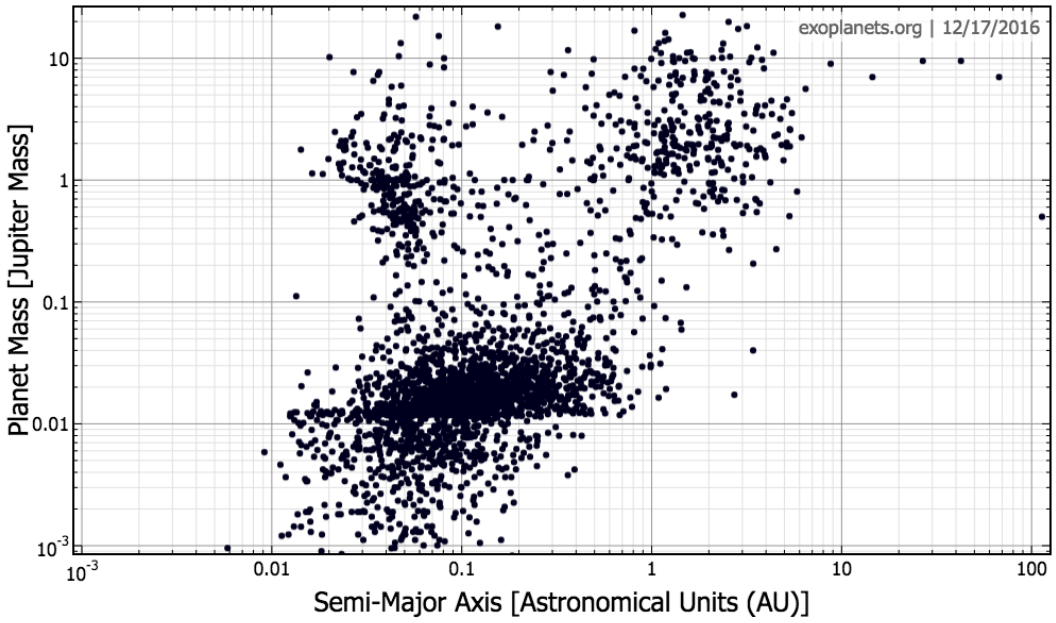

Figure 2.1: Semi-major axis (a) of the discovered exoplanets against their mass (m). Data are from http://exoplanets.org/.

gravitationally unstable molecular cloud collapses to form a star. Due to the angular momentum conservation, a part of its materials ends up with a flattened gas proto-planetary disk around the central young star. The gas and dust grains in the disk accrete to kilometer-sized planetesimals due to electrostatic and gravitational interactions, and lead to Moon- to Mars-sized planetary embryo via "oligarchic growth" (Kokubo & Ida 1998, 2000). A few terrestrial planets form near the star through a further merger stage within the snow line ($\sim$ 3 AU), where the volatile materials, such as water ice, are prevented from grains due to the high temperature (e.g., Chambers & Wetherill 2000; Kokubo et al. 2006). The formation of giant planets is a bit more complex. A widely accepted theory of giant planet formation, core accretion theory, predicts that giant planets form beyond the snow line. The low temperature allows forming a massive core with approximately $10 M_\oplus$ due to the condensation of volatile materials. After the core formation, it gathers gas from the surrounding proto-planetary disk to become a giant planet (e.g., Bodenheimer & Pollack 1986; Mizuno 1980; Pollack et al. 1996).

It is obvious that giant planet formation theory does not match the current close-in orbits of HJs. Thus, it is generally believed that HJs formed at larger distances from their host stars and subsequently migrated to their current shorter period orbits. Several migration mechanisms of HJs have been proposed and we provide a brief review.

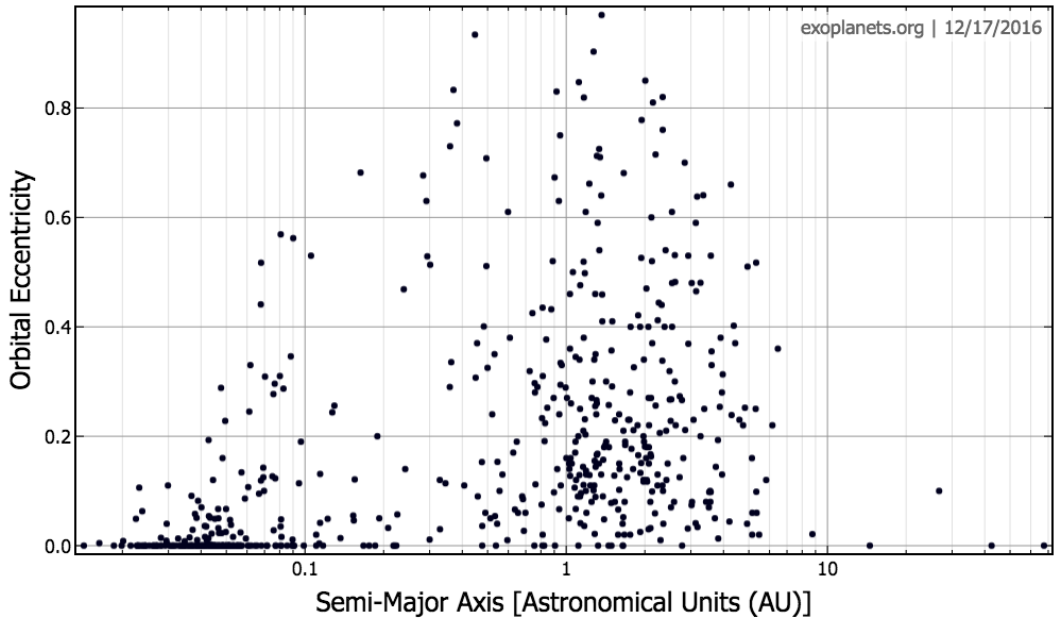

Figure 2.2: Semi-major axis (a) of the discovered exoplanets with mass $m > 0.5M_{\rm J}$ against their eccentricities (e). Data are from http://exoplanets.org/.

2.2.1 Disk Migration

One plausible model of forming HJs is disk migration. The interaction between planets and the proto-planetary disk due to the mutual angular momentum exchange leads to the orbital migration (Goldreich & Tremaine 1980). It is originally studied for the planets in our Solar system and later used to explain the origin of HJs (e.g., Alibert et al. 2005; Lin et al. 1996).

Lin & Papaloizou (1986) suggested that a sufficient massive planet ($> 10M_{\oplus}$) can clear its co-orbital region and open a deep gap around its orbit due to the tidal torque by the disk. Then the planet undergoes orbital migration on the disk viscous timescale with the continuous angular momentum transformation (see review e.g., Lubow & Ida (2010) for more detail). The migration halts at the inner region of the edge of the disk, and creates a HJ (Lin et al. 1996).

2.2.2 High-e Migration

An alternative possibility of forming HJs is high-e migration. The eccentricity of a planet is excited to an extremely high value after its disk depletion and the subsequent tides, as will be explained in section 2.5, circularize its orbit. There are several different approaches to enhance the eccentricity of a planet, and we review those mechanisms as below.

Planet-Planet Scattering

The basic idea of planet-planet scattering (e.g., Beauge & Nesvorny 2012; Nagasawa et al. 2008; Nagasawa & Ida 2011; Rasio & Ford 1996) is increase of the eccentricity by the strong scattering between gravitationally unstable planets. Giant planets tend to form at nearly maximally compact configuration by core accretion theory (Ida & Lin 2004a,b). Therefore, after disk depletion, giant planets with near circular and coplanar orbits may become gravitationally unstable, and start chaotic evolution with eccentricity growth, orbital crossing, and close encounter. When the pericenter of one planet becomes sufficiently close to the host star, subsequent tidal dissipation moves that planet into a HJ, while the other planets are left in distant orbits or even ejected from the system.

Secular Chaos

Secular chaos (Hamers et al. 2017; Wu & Lithwick 2011) provides another possibility to excite the eccentricity of the planet under the orbital evolution of two or more giant planets formed by core accretion theory. It requires initially two or more well-spaced, eccentric, and/or inclined planets not close to any strong mean-motion resonance. Secular interactions can lead to chaos due to the initial significant AMD (the angular momentum deficit; a measure for the system's angular momentum deviation from circular and coplanar orbits). Initially, most of AMD resides in the eccentric outer planets. The innermost planet gradually raises its eccentricity due to the equipartition of AMD till the starting of tidal circularization, creating a HJ. Note, the planets never cross their orbits among each other.

The Lidov-Kozai migration

The Lidov-Kozai mechanism is a large amplitude modulation between the eccentricity of the inner body and the mutual orbital inclination by the perturbation of the distant outer perturber in a hierarchical triple configuration. It requires that the initial mutual orbital inclination passes a threshold value. It is first studied by Lidov (1962) and Kozai (1962) for the evolution of a highly inclined asteroid (near-Earth satellite) on the perturbation of Jupiter's (Moon's) orbit.

For a planetary system with an inner planet and a distant outer inclined perturber, the Lidov-Kozai mechanism drives a periodic variation between the mutual orbital inclination and the eccentricity of the inner planet. The maximum eccentricity during each oscillation cycle can reach to near unity, thus HJ systems can form with following tidal dissipation (e.g., Anderson et al. 2016; Fabrycky & Tremaine 2007; Naoz et al. 2011; Petrovich 2015a; Wu & Murray 2003). A more detailed review is presented in Appendix C.

Coplanar High-eccentricity Migration

Coplanar High-eccentricity Migration (CHEM) works in hierarchical triple systems with initially eccentric and near-coplanar orbits. The eccentricity of the inner planet can be enhanced to near unity by the perturbation of the outer perturber, and subsequent tides circularize the inner orbit to create a HJ (e.g., Li et al. 2014; Petrovich 2015b; Xue & Suto 2016; Xue et al. 2016). A more detailed review is presented in section 2.4. And we comprehensively examine this model in chapter 4, which is our own work.

2.3 Observation to Distinguish HJ Migration Mechanisms

Each of those different migration mechanisms may have contributed to the observed HJs population to some degree, so the main question is their relative contribution. The observation provides a potential window in answering this question. Indeed, the observation results are in favor of high-e migration mechanisms in general. We review several observational signatures as below.

2.3.1 Eccentricity Distribution

One observational signature is the eccentricity distribution of Jupiter-like exoplanets ($m > 0.5M_{\rm J}$). As shown in Figure 2.2, HJs with semi-major axis less than 0.1 AU tend to have circular orbit due to tidal circularization; about half planets with period larger than 10 days have moderate to high eccentricities ($e > 0.2$). In disk migration, Papaloizou et al. (2001) found that the planet remains in a circular orbit with a disk for mass less than $10M_{\rm J}$, and can generate a moderate eccentricity up to ~ 0.25 for mass more than $20M_{\rm J}$. This result implies that disk migration itself is difficult to reproduce the current eccentricity distribution. On the other hand, high-e migration is natural to generate high eccentricities. Indeed, the current eccentricity distribution can be reproduced by the secular configuration of two-planet systems and/or planet-planet scattering with a wide range of initial conditions (e.g., Chatterjee et al. 2008; Petrovich 2015a; Timpe et al. 2012).

2.3.2 Chemical Compositions

The chemical properties, in particular, the carbon/oxygen (C/O) ratio of planetary atmospheres, provide an important hint in distinguishing those different migration mechanisms. Current giant planet formation models indicate a strong correlation between the composition of a planetary atmosphere and its location where the planet gathers gas in the disk (Madhusudhan et al. 2014). Since different chemical compositions, such as H_2O, CO, and CO_2, have different snow lines, planets formed at larger distances beyond the

snow line of H_2O and migrated without disk in high-e migration tend to have higher C/O ratio of atmosphere than in disk migration. Indeed, the current high C/O ratio of HJs significantly prefers high-e migration (Brewer et al. 2016; Madhusudhan et al. 2014).

2.3.3 Companion of HJs

Steffen et al. (2012) found the lack of the observed close companions in HJ systems. This result favors high-e migration, but in stark contrast with disk migration, because a HJ clears its nearby region in high-e migration due to the violent dynamical evolution but not in disk migration. More recent follow-up radial velocity observation found possible massive distant companions for about half HJ systems (Knutson et al. 2014). The presence of those distant companions also supports high-e migration, since high-e migration predicts one or a few planetary/stellar distant companions to excite the eccentricity of the planet.

2.3.4 Spin-orbit Angle Distribution

Yet another, may be more important observational signature comes from the measurement of the projected spin-orbit angle, the sky-projected angle between the spin of the central star and the orbit of the planet, λ, mainly through the Rossiter-McLaughlin effect for many transiting HJs. The Rossiter-McLaughlin effect is an anomalous Doppler shift due to that the planet hides part of the rotating star that is rotating towards or away from the observer. The observed distribution of the projected spin-orbit angles, λ, is plotted in Figure 2.3 on the basis of the Holt-Rossiter-McLaughlin Encyclopedia compiled by René Heller[2]; the radial coordinate of each symbol corresponds to the logarithm of the orbital period of the planet ($P \propto a^{3/2}$), and its angular coordinate represents the observed value of λ. Black and red circles indicate the innermost planets in single transiting systems, and the largest planets in the multi-transiting systems, respectively. The range of the Solar system planets is plotted in a blue region.

Among the differences between the proposed mechanisms is that high-e migration would predict broad even close to random distribution of the spin-orbit angle, but disk migration would preserve the relative orientation (most likely very close to zero, but it is possible that the spin axis of the central star is moderately misaligned with the normal vector of the primordial disk (e.g., Bate et al. 2010; Batygin 2012; Foucart & Lai 2011; Lai 2014)). For this reason, measuring the spin-orbit angle has attracted attention as a potential window into learning about the evolution of HJs. As shown in Figure 2.3, the projected spin-orbit angle, λ, has been measured for more than 90 transiting planets. More than half of them are aligned, and about 40% of them exhibit significant misalignment. Furthermore, there are 13 retrograde ($\lambda > 90°$) and 2 counter-orbiting ($\lambda > 160°$, just for definiteness in this thesis) planets; HAT-P-6b with $\lambda = 165° \pm 6°$ (Albrecht et al. 2012)

[2]http://www.physics.mcmaster.ca/~rheller/

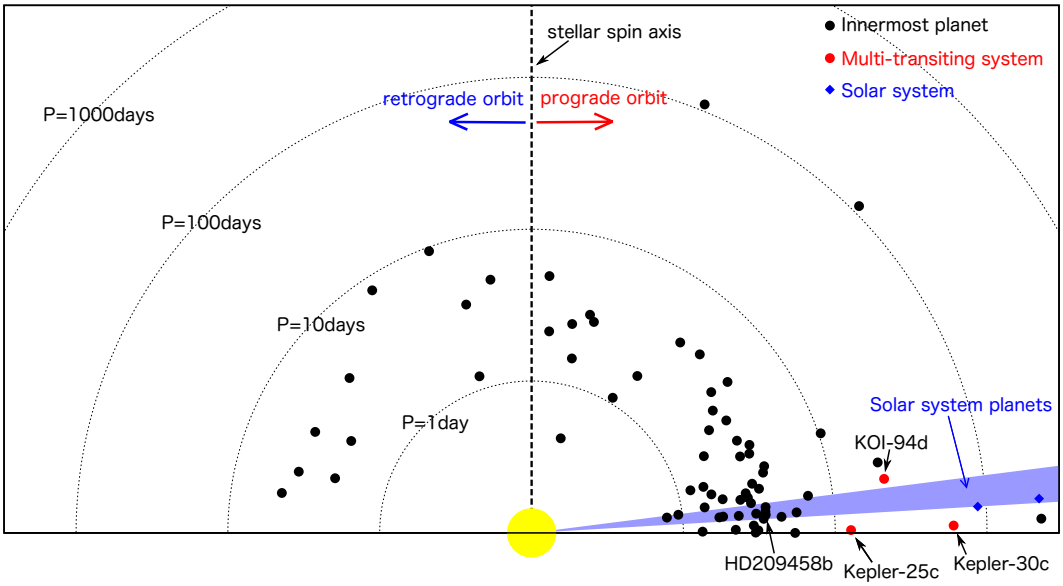

Figure 2.3: Projected spin-orbit angles λ for transiting planets. Black circles indicate innermost planets in single transiting systems, while red circles denote the largest planets in the three multi-transiting systems, Kepler-25c (Albrecht et al. 2013), Kepler-30c (Sanchis-Ojeda et al. 2012), and KOI-94d (Hirano et al. 2012; Masuda et al. 2013).

and HAT-P-14b with $\lambda = 189°.1 \pm 5°.1$ (Winn et al. 2011). These unexpected, counter-intuitive discoveries imply that some of HJs should have experienced high-e migration to tilt the spin.

The above two candidates of counter-orbiting HJ systems are particularly interesting, since they cannot be explained by most of the above models. Disk migration predicts a low spin-orbit angle due to the quasi-Keplerian motion in a gaseous disk. In contrast, planet-planet scattering, secular chaos, and the Lidov-Kozai migration predict broadly distributed, even retrograde, spin-orbit angles. Even in those cases, however, counter-orbiting HJ systems are known to be difficult to form. Figure 14 of Nagasawa & Ida (2011), for instance, indicates that there is no counter-orbiting HJ in all the 241 HJs produced by planet-planet scattering. The simulations by Hamers et al. (2017) show that all the HJs formed by secular chaos have the spin-orbit angle less than 120° (see their Figure 10). Finally, Figure 3 of Naoz et al. (2012) also illustrates that no counter-orbiting HJ is produced by the Lidov-Kozai migration for their ten thousand runs with a stellar perturber.

Note the observed λ differs from the *true* spin–orbit angle ψ; they are related in terms of the orbital inclination $i_{\rm orb}$ and the obliquity of the stellar spin-axis $i_\star$ as

$$\cos\psi = \cos i_\star \cos i_{\rm orb} + \sin i_\star \sin i_{\rm orb} \cos\lambda \approx \sin i_\star \cos\lambda. \tag{2.1}$$

The above approximation holds for transiting systems with $i_{\rm obs} \approx \pi/2$. Since the stellar

axis is usually defined so that $0 < i_\star < \pi/2$, equation (2.1) implies that $\psi \geq \lambda$ if $0 < \lambda < \pi/2$ while $\psi \leq \lambda$ if $\pi/2 < \lambda < \pi$.

The true spin-orbit angle ψ is not so easy to obtain, but can be estimated by combining the measurement of $i_\star$ via asteroseismology (Campante 2014; Christensen-Dalsgaard 2014; Gizon 2003; Huber et al. 2013; Unno et al. 1989). Benomar et al. (2014) performed the first quantitative determination of ψ for transiting planetary systems around main-sequence stars. For HAT-P-7, their asteroseismology analysis yields $i_\star \approx 30°$, and they obtain $\psi \approx 120°$ from the joint analysis of the Rossiter-McLaughlin measurement of $\lambda \approx 180°$. For Kepler-25c, they obtain $i_\star = 65°.4^{+10°.6}_{-6°.4}$, and $\psi = 26°.9^{+7°.0}_{-9°.2}$, which should be compared with $\lambda = 9°.4 \pm 7°.1$. Indeed these results demonstrate the importance of the projection effect mentioned above. More importantly, planetary systems with $\lambda \approx 180°$ may not be necessarily counter-orbiting, but just retrograde. This may also be the case for HAT-P-6b with $\lambda = 165° \pm 6°$(Albrecht et al. 2012), and HAT-P-14b with $\lambda = 189°.1 \pm 5°.1$(Winn et al. 2011).

Therefore the existence of the counter-orbiting planets has not yet been established observationally so far. Nevertheless, it is tempting to consider a dynamical model that can theoretically explain the counter-orbiting HJs if exist at all. One promising mechanism, Coplanar High-eccentricity Migration (CHEM), has been recently proposed by Li et al. (2014). Indeed, CHEM is a potentially unique formation model of counter-orbiting HJs that no other model is known to generate. We review CHEM in the next section.

2.4 Coplanar High-eccentricity Migration (CHEM)

As briefly described in subsection 2.2.2, CHEM is one of high-e migration mechanisms to form HJs. In this section, we review the previous studies of CHEM.

2.4.1 Orbital Flip

Li et al. (2014) considered a near-coplanar hierarchical triple system, and pointed out that the interaction due to the outer perturber can increase the eccentricity of the inner planet and flip its orbit by $\sim 180°$. A typical example is shown in Figure 2.4. They found that e_1 increases monotonically and the mutual orbital inclination between the two bodies, i_{12}, remains low just before the flip, and then the orbital flip of the inner planet proceeds in a very short timescale when the eccentricity of the inner planet, e_1, becomes very close to unity, $1 - e_1 \sim 10^{-3} - 10^{-4}$. In that case, the angular momentum of the inner planet is roughly given as $m_1\sqrt{Gm_0(1-e_1^2)} \approx m_1\sqrt{2Gm_0(1-e_1)}$, where m_0 and m_1 are the mass of the central body and inner body, and even a small perturbative torque may easily change the angular momentum of the inner planet, and thus flip its orbit if the value of $1 - e_1$ is sufficiently small.

In particular, they derived an *extreme eccentricity condition* that e_1 reaches unity in a near-coplanar hierarchical triple system under the secular perturbation up to the

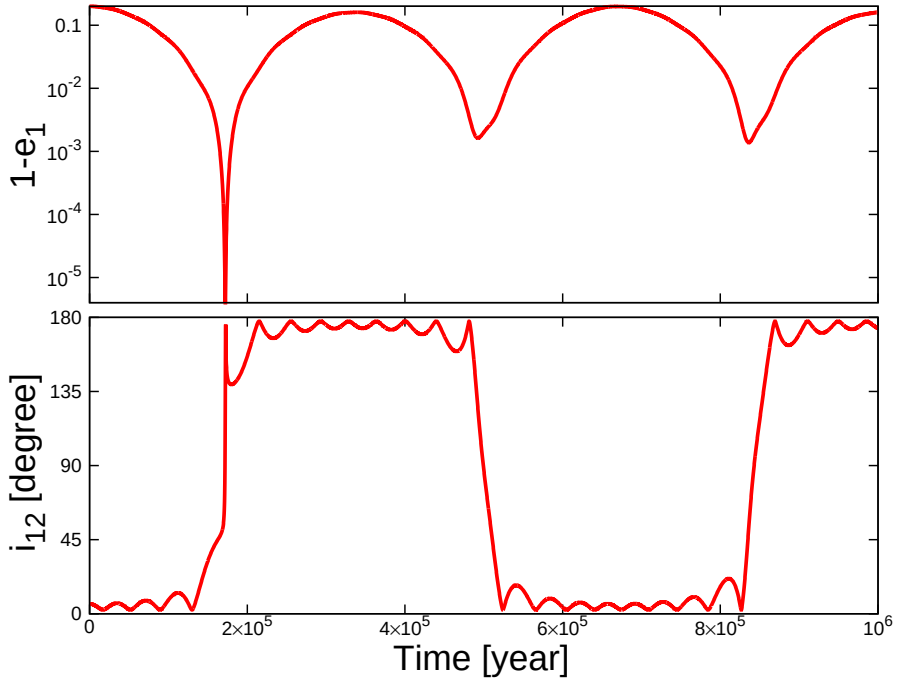

Figure 2.4: Example of the orbital flip during the extremely high eccentricity excursion in a near-coplanar hierarchical triple configuration. The initial condition is $m_0 = 1M_\odot$, $m_1 = 1M_\mathrm{J}$, $m_2 = 0.03M_\odot$, $e_1 = 0.8$, $e_2 = 0.6$, $a_1 = 5$ AU, $a_2 = 50$ AU, and $i_{12} = 6°$. Upper panel: eccentricity e_1; Bottom panel: mutual orbital inclination i_{12}.

octupole order of the gravitational potential of the outer perturber. To be more specific, their extreme eccentricity condition is written as

$$\epsilon_\mathrm{pl} > \frac{8}{5}\frac{1-e_{1,i}^2}{7-e_{1,i}(4+3e_{1,i}^2)\cos(\omega_{1,i}+l_{1,i})}, \tag{2.2}$$

in terms of

$$\epsilon_\mathrm{pl} \equiv \frac{a_1}{a_2}\frac{e_2}{1-e_2^2} \tag{2.3}$$

which characterizes the ratio of the orbit-averaged octupole to quadrupole terms in the test particle limit ($m_1 \ll m_0, m_1 \ll m_2$). In the above expressions, e, a, ω, l, and m denote the eccentricity, semi-major axis, argument of pericenter, longitude of ascending node with the subscripts 1 and 2 indicating the inner and outer body, respectively. In the test particle limit, a_1, a_2, and e_2 are conserved, and thus ϵ_pl defined by equation (2.3) is also a constant of motion. The other orbital elements are time-dependent, and we use the subscript i in equation (2.2) in order to indicate their initial values. Li et al. (2014) numerically computed the evolution of such coplanar triple systems in the test particle

limit, and confirmed that the extreme eccentricity condition is very well described by equation (2.2).

Petrovich (2015b) presented a more general form of the extreme eccentricity condition in the planetary limit ($m_1 \ll m_0$, $m_1 \leq m_2$) on the basis of the conservation of the energy (the orbit-averaged quadrupole and octupole potential terms) for the coplanar hierarchical triple configuration. His result, equation (11) of Petrovich (2015b), can be written as

$$\epsilon_{\rm L} < \epsilon_{\rm pl} \equiv \frac{a_1}{a_2}\frac{e_2}{1-e_2^2} < \epsilon_{\rm U}, \tag{2.4}$$

which reduces to equation (2.2) in the test particle limit of the inner planet. The lower and upper boundaries, $\epsilon_{\rm L}$ and $\epsilon_{\rm U}$, defining the boundary of the extreme eccentricity region are determined by the value of the final angle $\varpi_f \equiv \cos^{-1}\hat{\mathbf{e}}_{1,f}\cdot\hat{\mathbf{e}}_{2,f}$ between the inner and outer orbital unit Lenz vectors. Specifically $\epsilon_{\rm L}$ and $\epsilon_{\rm U}$ correspond to $\varpi_f = 0$ and π, respectively. A more detailed consideration of the extreme eccentricity condition is presented in subsection 4.2.1.

2.4.2 Short-range Forces

Short-range forces (SRFs) include general relativity (GR), stellar and planetary non-dissipative tides, and stellar and planetary rotational distortion. Indeed, those SRFs may significantly affect the dynamical evolution of the inner planet. Liu et al. (2015) found that SRFs (GR, planetary non-dissipative tides, and planetary rotational distortion) suppress the extreme value of e_1 that otherwise could be achieved due to the octupole term in hierarchical triple systems with large mutual orbital inclination (i.e., not coplanar configuration) in the Lidov-Kozai oscillation. These additional forces induce a precession of the Lenz vector of the inner planet, and impose a strict upper limit on the maximum achievable value of e_1; as the SRFs become stronger, the orbital flips are more confined to the region where the mutual orbital inclination i_{12} is close to 90°. This result strongly implies that one needs to incorporate those SRFs in order to describe properly the dynamics of near-coplanar hierarchical triple systems, which is not taken into account in the analytical consideration of Li et al. (2014).

Petrovich (2015b) examined the effect of GR and planetary non-dissipative tides on the maximum achievable eccentricity of the inner planet, and compared it with the extreme eccentricity condition ($e_1 = 1$) without SRFs in CHEM. He found that SRFs effectively limit the maximum eccentricity. Also, the maximum eccentricity is higher for larger initial semi-major axis of the inner planet, a_1, because the potential of SRFs increases with decrease of a_1, while that of the octupole term remains constant at fixed a_1/a_2.

2.4.3 Numerical Experiments: Forming Counter-orbiting HJs?

Li et al. (2014) first proposed CHEM for the formation of counter-orbiting HJs. One example is shown in Figure 2.5. The inner planet flips by $\sim 180°$ at $t \sim 5\times10^6$ yr,

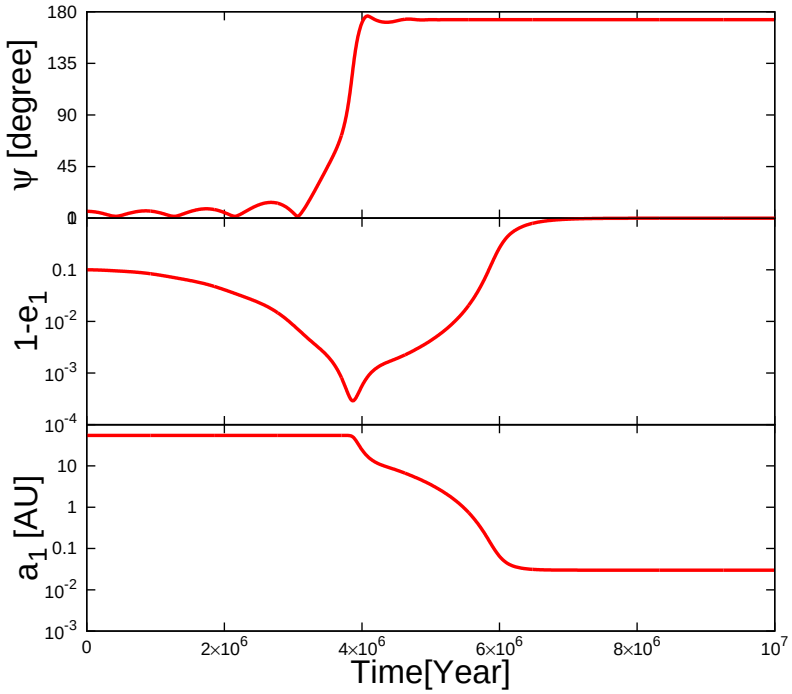

Figure 2.5: One example for the formation of the counter-orbiting HJ in CHEM. The initial condition adopts $m_0 = 1M_\odot$, $m_1 = 1M_\mathrm{J}$, $m_2 = 0.03M_\odot$, $a_1 = 59.35$ AU, $a_2 = 500$ AU, $e_1 = 0.9$, $e_2 = 0.6$, and $i_{12} = 6°$. The tidal quality factor of the central star and inner planet are set to $Q_\mathrm{s} \sim 10^6$ and $Q_\mathrm{p} \sim 10^5$. Tides circularize the orbit after the orbit flip. The final equilibrium state of the system has $a_{1,f} \sim 0.032$ AU, $e_{1,f} \sim 0$, and $\psi \sim 172°$.

before tidal circularization. Such a counter-orbiting eccentric planet soon becomes circularized with subsequent tidal dissipation, and is expected to become a counter-orbiting HJ eventually.

Petrovich (2015b) performed a series of simulations in CHEM including GR and planetary tides. He considered a sun-like central star and a Jupiter-like inner planet with $m_0 = 1M_\odot, m_1 = 1M_\mathrm{J}$. For the perturber mass, he chose m_2 as a planetary perturber uniformly distributed in [1.3,1.7] M_J. In his simulations, the most common outcome is non-migrating planets without experiencing significant migration; a few percent end up with HJs; very few become disruption or migrating. He found that the resulting HJs have relatively low spin-orbit angles in prograde orbits and the distribution of the semi-major axis of resulting HJs is in good agreement with the observation.

Petrovich (2015b) concluded that CHEM can produce HJs with low spin-orbit angles in prograde orbits, but no counter-orbiting HJ. This result is in contrast to Li et al. (2014), who found that CHEM is a possible mechanism to produce counter-orbiting HJs. Petrovich (2015b) claimed that the necessary condition for the orbital flip is the extremely high eccentricity of the inner planet. Therefore, the initial semi-major axis of the inner planet has to be large enough to avoid of being tidal disrupted and overcome the

suppression due to SRFs. Indeed, most of his initial conditions do not satisfy $\epsilon_{\rm pl} < \epsilon_{\rm U}$ in the extreme eccentricity condition equation (2.4) even when they satisfy $\epsilon_{\rm pl} > \epsilon_{\rm L}$. Therefore his set of simulations does not cover the relevant parameter space for the formation of counter-orbiting HJs. A more detailed consideration of this discrepancy is presented in chapter 4.

2.4.4 Our Approaches

Those interesting previous results motivated us to systematically explore the fate of the inner planet in near-coplanar hierarchical triple systems. In this thesis, we generalize the planetary limit by Petrovich (2015b) taking into account the finite mass of the inner planet on the dynamics of the central star. Then, we present a more general form of the extreme eccentricity condition. We perform the numerical simulation including up to the octupole order of the gravitational potential, SRFs, and dissipative tides; we systematically explore the fate of the inner planet in CHEM for both a sub-stellar outer perturber and a planetary outer perturber. Such a configuration is expected from dynamically unstable multi-planetary systems. Our initial condition homogeneously covers the relevant extreme eccentricity condition, and thus differs from Petrovich (2015b). We provide an analytical estimate of the migration timescale including the SRFs effect that significantly change the dynamics of the orbital evolution (Liu et al. 2015). This estimate is useful in interpreting the present simulation results, and also in predicting the migration timescale for different situations analytically. Furthermore, while all previous studies of CHEM focus on the HJ formation, several super-Earths with semi-major axis less than 0.1 AU have been observed, and their origin still remains unknown. Therefore, we extend our simulation to an inner planet of super-Earth mass to see if CHEM can account for those very close-in super-Earths. We also apply our simulations to the observed systems and examine to what extent CHEM can explain the existence of close-in planets in hierarchical triple and counter-orbiting HJ systems.

The basic equations for point masses interacting only through the gravity up to the octupole order and SRFs are fully presented in section 3.1 and 3.2. The tidal model we adopt here is the conventional equilibrium tide model, which is described in section 2.5 and the corresponding equations are presented in section 3.3.

We find that most of the systems are tidally disrupted and a fraction of survived planets remains mainly as prograde HJs; the formation of counter-orbiting HJs is possible only in a very restricted parameter range, which implies that even CHEM is not so easy to produce counter-orbiting HJs. Nevertheless, this is also a promising channel to produce prograde HJs. In addition, we find that CHEM can reproduce a reasonable fraction of close-in prograde planets in the observed hierarchical triple systems, but are very difficult to reproduce counter-orbiting HJ systems. Here we consider the formation of HJ until the fully tidal circularization ($e < 0.01$), and term as *formation stage*.

2.5 Tidal Evolution

Tide is raised on one body by another due to the effect of differential and inelastic deformations. Such deformations are generally accompanied by the dissipation. In a planetary system, the star and planet are referred to as extended fluid bodies with non-spherical structure in a non-uniform gravitational field. The tidal dissipation continuously affects the spin and orbital evolution, until reaching an equilibrium configuration with circularization, synchronization, and spin-orbit alignment. In this section, we review the basic structure of tides and the tidal models we adopt in the present thesis.

2.5.1 Equilibrium Tide Model

Consider a star-planet system, the tidal potential of the planet over its surface periodically varies as the orbital rotation. Each component of the tidal potential generates its tidal bulge at the corresponding frequency with fixed amplitude. The height of the tidal bulge depends on the internal structure and the self-gravity. The sum up of all the tidal bulge determines the total tidal response of the planet. The equilibrium tide model assumes that the deformation of the planet is determined by the tidal potential following the equipotential bulge (MacDonald 1964).

Indeed, due to the imperfect elasticity, the phase angle of the tidal bulge at planetary surface lags behind that of the tidal potential by an angle δ. This lag angle is determined by the combination of tidal forcing frequency (σ) and the delay time (Δt) as (Kaula 1964):

$$\delta(\sigma) = \sigma \Delta t(\sigma). \tag{2.5}$$

The forcing frequency is a linear combination of the spin rate $\Omega_{\rm p}$ and mean motion n. For example, $\sigma = 2|\Omega_{\rm p} - n|$ corresponds to the semi-diurnal tide, and $\sigma = |2\Omega_{\rm p} - n|$ refers to the annual tide.

In order to describe the dissipation efficiency of tides, it is well accepted to introduce a control parameter, which can be the tidal quality factor (Q) or delay time (Δt).

A commonly used tidal quality factor is defined as the specific dissipation function as (Goldreich 1963):

$$Q \equiv \frac{2\pi E}{\Delta E} = \frac{1}{\tan \delta(\sigma)}, \tag{2.6}$$

where E refers to the peak energy stored in the system during one tidal cycle, and ΔE is the energy dissipated in each cycle.

A higher Q means a lower dissipation rate, and vice versa. The estimated values for main-sequence stars are $> 10^6$ (e.g., Trilling et al. (1998)), and for Jupiter and Neptune are $> 10^4$ (e.g, Lainey et al. 2009; Zhang & Hamilton 2009). Given $Q \gg 1$, a correlation between Q and Δt can be obtained as follows,

$$Q \approx \frac{1}{\delta(\sigma)} = \frac{1}{\sigma \Delta t(\sigma)}. \tag{2.7}$$

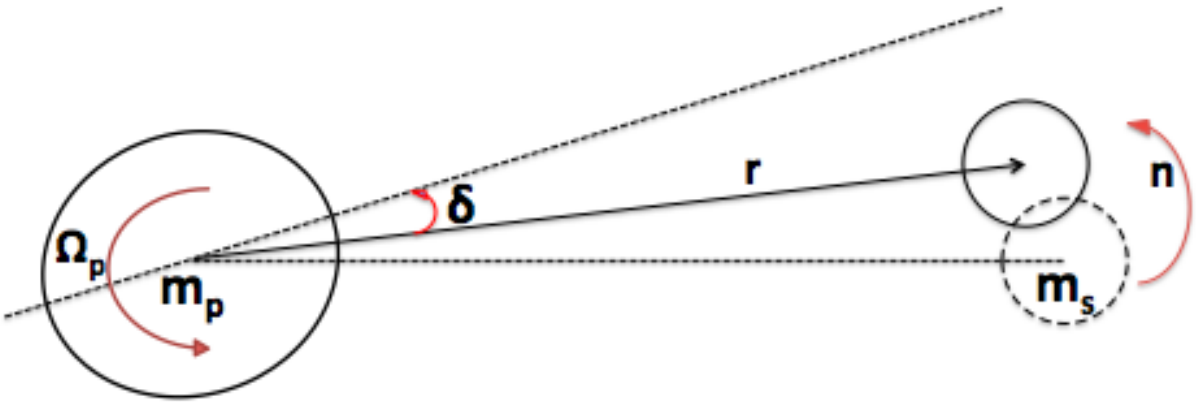

Figure 2.6: Schematic figure of the tidal lag in the equilibrium tide model. The tidal lag is determined by the difference of the spin rate of the planet ($\Omega_{\rm p}$) and its mean motion (n). The lag angle δ is $(\Omega_{\rm p} - n)\Delta t$, where Δt is the delay time.

In particular, the dominate term of tidal dissipation is generally the semidiurnal tide for systems beyond the synchronization (Ferraz-Mello et al. 2008), and the corresponding tidal quality factor in this case is

$$Q \approx \frac{1}{2|\Omega_{\rm p} - n|\Delta t}. \tag{2.8}$$

The detail of tidal dissipation and tidal response are still not well understood. Many different approaches have been proposed and we briefly introduce two popular models. One common approach to estimate the tidal dissipation efficiency is adopting constant Q. In this assumption, the dissipation rate is independent of the tidal forcing frequency. This assumption becomes invalid for large eccentricity (Greenberg 2009). Also, the discontinuities happen for $\sigma = 0$ (e.g., Correia & Laskar (2010)). An alternative approach is assuming systems with constant Δt. This model becomes linear as $\sigma\Delta t \ll 1$ (Mignard 1979). It is valid to arbitrary eccentricity and inclination (Greenberg 2009). In this thesis, we always adopt constant Δt model. The sets of equations are fully described in subsection 3.3.1.

2.5.2 Equilibrium Tide Problem

Independently of the formation channels, HJs are currently subject to strong tidal interactions with their host stars. Therefore, the observation of the projected spin-orbit angle, λ, provides possible constraints on the tidal theories. Winn et al. (2010) found a possible trend that the central stars hotter than $T_{\rm eff} \sim 6250$ K tend to have misaligned orbits, while cooler stars have aligned orbits (see Figure 2.7). This critical temperature is also an approximate boundary that above it the mass in the convective envelopes becomes very

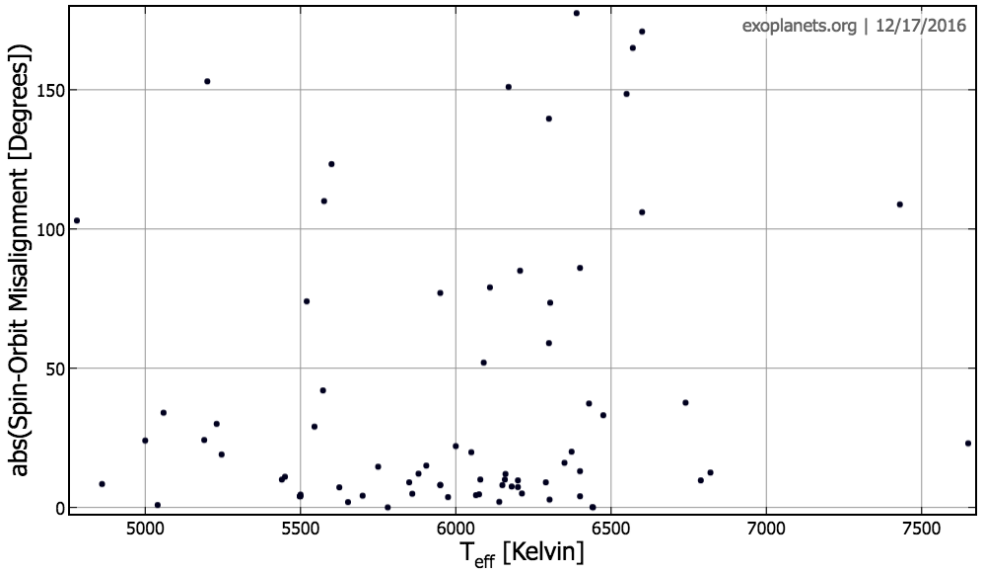

Figure 2.7: Projected spin-orbit angle, λ, as a function of the stellar effective temperature, $T_{\rm eff}$. Data are from http://exoplanets.org/.

thin or absent for the main-sequence stars. The mass of the convective zone is decreased by a factor of 120 between types G0 and F5 (5940 and 6650 K). Indeed, the presence of convective zone is essential for the tidal dissipation, since the energy transportation is much more effective for a thick convective envelope. Therefore, they proposed that HJs form via high-e migration with broadly distributed spin-orbit angle, and then tides modify the spin-orbit angle distribution, align the systems around cool stars but keep their original value for systems around hot stars. Triaud (2011) found an empirical evidence that older systems (> 2.5 Gyr) show a higher fraction of spin-orbit alignment, which also implies the importance of tides.

In the conventional equilibrium tide model, the orbital separation between the interacting bodies, the central star and innermost planet is roughly constant and slowly varied tides generate an equilibrium figure. The viscosity due to tides leads to dissipation. And the followed energy and angular momentum exchange leads to circularization, synchronization, and spin-orbit alignment. Equilibrium tides effectively realign the spin-orbit angle, however, it has been shown that the equilibrium tide model results in the orbital decay at a comparable timescale (Barker & Ogilvie 2009); see equations (3.54) to (3.56). HJs in the realigned systems quickly fall into their central stars, thus are very unlikely to be observed. Therefore, the equilibrium tide model itself can not explain the majority of the realigned systems with finite semi-major axis and $\lambda - T_{\rm eff}$ correlation.

2.5.3 Decouple Model

In order to solve this problem, Winn et al. (2010) proposed a model by considering a much smaller effective stellar moment of inertial. They assume that only the convective envelope, the outer layers of the star, synchronizes and aligns with the planetary orbit by the tidal dissipation. The inner radiative zone is weakly coupled to the outer convective zone and to the planet. In this model, the planet aligns in a much shorter timescale than the orbital decay. In reality, however, it is not clear to what extent the decoupling model can explain the observed distribution since there is no systematic and quantitative study of this model. From the theoretical point of view, the core-envelope decoupling has been discussed mainly in the young star regime, but it is controversial for the main-sequence stars. In addition, our sun is known to have a strong coupling between the convective and radiative zones (e.g., Howe 2009). Thus, the theoretical support for this model seems weak.

2.5.4 Lai Model

Recently, Lai (2012) proposed a new model in which the damping timescale of the spin-orbit angle can be significantly smaller than that of the planetary orbit. When the stellar spin is misaligned with respect to the planetary orbital axis, one component in the tidal potential may excite inertial waves driven by the Coriolis force in the convective zone and provide a dynamical tidal response (Goodman & Lackner 2009). This effect increases the efficiency of the realignment process without contributing to the orbital decay.

The model was studied in detail by Rogers & Lin (2013), who numerically integrated a set of simplified equations for the semi-major axis a, the spin angular frequency of the central star $\Omega_{\rm s}$, and the spin-orbit angle ψ, originally derived by Lai (2012). They found that planetary systems with initially arbitrary spin-orbit angles have three stable configurations; aligned, polar, and anti-aligned orbits.

In this thesis, we focus on the Lai model by considering the additional tidal torque excited by inertial waves. The basic equations of the Lai model are presented in subsection 3.3.2 and Appendix D. We confirm the conclusion of Rogers & Lin (2013) that the Lai model predicts three distinct stable configurations–aligned, polar, and anti-aligned. In reality, however, the latter two turn out to be metastable and approach aligned orbits over a longer timescale as the equilibrium tide effect exceeds that of the inertial wave dissipation. We present a detailed comparison with the previous results by Rogers & Lin (2013), and argue that the full set of equations we adopt is important in understanding the long term evolution of the tidal model.

Chapter 3

Basic Equations

In this chapter, we present the basic equations we adopt in our simulation. We review the secular approximation on both for point masses interacting only through the gravity in section 3.1 and SRFs effect in section 3.2, and two tidal models in planetary systems, the equilibrium tide model and the Lai model, in section 3.3.

3.1 Hierarchical Triple System

Hierarchical triple system consists of an inner binary and an outer distant perturber. A schematic configuration of near-coplanar hierarchical triple systems is illustrated in Figure 3.1. A central star of mass m_0 and radius R_0 is located at the origin of the coordinate. The normal vector of the invariable plane is the total orbital angular vector $\mathbf{G}_{\rm tot} = \mathbf{G}_1 + \mathbf{G}_2$ of the inner and outer bodies. Thus the mutual orbital inclination is given by $i_{12} = i_1 + i_2$ where i_1 and i_2 are the inclinations of each orbit with respect to the invariable plane.

Hierarchical triple systems are common in our universe, and the recent discoveries of exoplanetary systems with diverse orbital architectures have reactivated the research of such a configuration. As described in chapter 2, in a hierarchical triple system, the eccentricity of the inner planet can be enhanced to near unity by the perturbation of the outer perturber, and subsequent tides circularize the inner orbit to create a HJ. The mechanisms to form HJs in hierarchical triple systems are mainly divided into two categories: the Lidov-Kozai migration at a high mutual inclination configuration (see Appendix C for more detail) and CHEM at a near-coplanar configuration. In the current thesis, we systematically examine CHEM in detail as presented in chapter 4.

The methodology we adopt in studying hierarchical triple systems is the well accepted secular approximation. In doing simulations, although the direct integration of the full equations of motion can always track the evolution of such systems accurately, the analytical approach as the secular approximation is also useful and necessary to understand the physical process and significantly save the computational time.

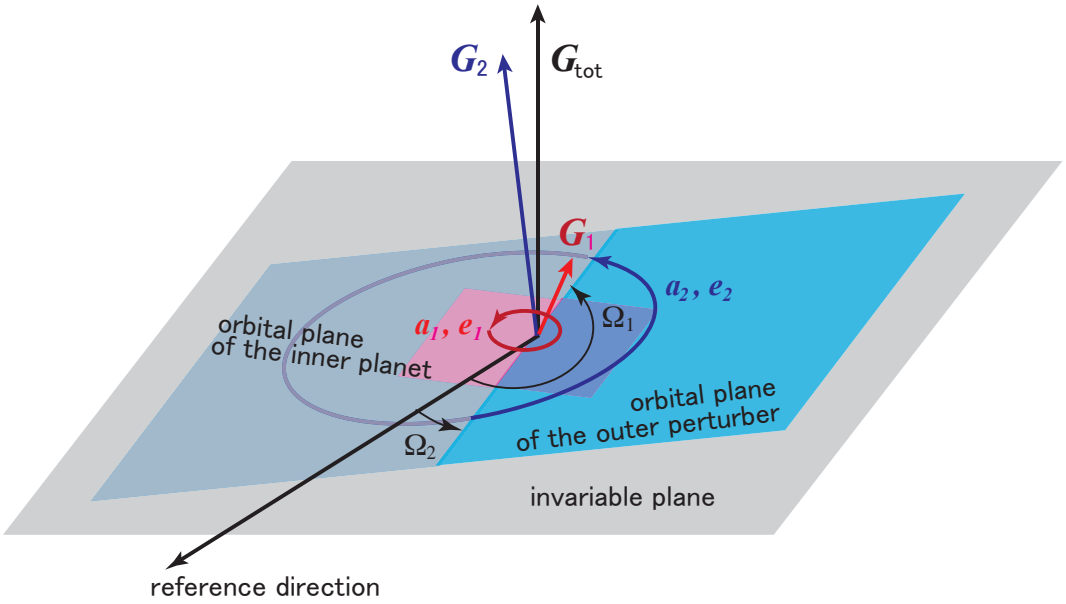

Figure 3.1: Schematic configuration of a near-coplanar hierarchical triple system in Jacobi coordinate.

In this section, we review the set of basic equations in secular approximation for point masses interacting only through the gravity in subsection 3.1.1, and its application on the extreme eccentricity condition under CHEM in subsection 3.1.2. In this thesis, we mainly focus on the formation of close-in planets in CHEM at an initial near-coplanar configuration. And the basic set of equations can be applied to a wide range of astrophysical systems, such as warm Jupiter systems presented in Appendix E, which needs further study.

3.1.1 Secular Approximation

Background

Secular approximation is based on series expansions in terms of the orbital elements. A traditional secular approximation is developed by Lagrange and Laplace in which the orbital elements change slowly over time. The variations can be obtained by expanding the Hamiltonian in terms of the eccentricity e and inclination i of each planet. However, it becomes not appropriate for very eccentric and/or inclined orbits. The pioneering work by Lidov (1962) and Kozai (1962) first studied the expansion in the ratio of the semi-major axis up to the second order, $(a_1/a_2)^2$, called the quadrupole approximation, in the limit of the restricted inner problem (the inner body is a test particle). They found large variations between the eccentricity and inclination of the inner test particle.

Recently, the importance of the octupole order, $(a_1/a_2)^3$, has been recognized. In

the octupole approximation, the inner orbit can flip between prograde ($i_{12} < 90°$) and retrograde ($i_{12} > 90°$) and the eccentricity of the inner body can reach extremely higher value than in the quadrupole approximation (Naoz et al. 2011). Throughout this thesis, we adopt the secular equations in the octupole approximation in our simulation.

Secular Equations in Octupole Approximation

Following Liu et al. (2015) and Correia et al. (2011), we present the secular equations up to the octupole order in a vectorial formalism. They considered a hierarchical triple system consisting of the central pair with mass m_0 and m_1, radius R_0 and R_1, and distant perturber with mass m_2. They derived the equations in Jacobi coordinates with $\mathbf{r}_1$ being the relative position from m_0 to m_1, $\mathbf{r}_2$ being the relative position from the central mass of m_0 and m_1 to m_2. The complete Hamiltonian can be written as follows (e.g., Harrington et al. 1968):

$$\begin{aligned}\mathbf{H} &= H_1 + H_2 + \Phi \\ &= -\frac{Gm_0m_1}{2a_1} - \frac{Gm_2(m_0+m_1)}{2a_2} - \frac{G}{a_2}\sum_{l=2}^{\infty}(\frac{a_1}{a_2})^l M_l(\frac{|\mathbf{r}_1|}{a_1})^l(\frac{a_2}{|\mathbf{r}_2|})^{l+1}P_l(\cos\theta), \quad (3.1)\end{aligned}$$

where H_1 and H_2 are the individual Hamiltonians of the inner and outer orbits, Φ is the interaction potential, a refers to the semi-major axis, θ is the angle between $\mathbf{r}_1$ and $\mathbf{r}_2$, M_l is a coefficient depending on m_0, m_1, m_2, and l, and $P_l(x)$ is the Legendre polynomial. The subscript 0, 1, and 2 refer to the central star, inner body, and outer perturber, respectively.

In the octupole approximation ($l = 3$), the interaction potential becomes

$$\Phi = \Phi_{\rm quad} + \Phi_{\rm oct}. \quad (3.2)$$

In equation (3.2), $\Phi_{\rm quad}$ and $\Phi_{\rm oct}$ refer to the quadrupole and octupole potential:

$$\Phi_{\rm quad} = -\frac{Gm_0m_1m_2}{(m_0+m_1)r_2}[\frac{3}{2}\frac{(\mathbf{r}_1\cdot\mathbf{r}_2)^2}{r_2^4} - \frac{r_1^2}{2r_2^2}], \quad (3.3)$$

$$\Phi_{\rm oct} = -\frac{Gm_0m_1m_2(m_0-m_1)}{(m_0+m_1)^2r_2}[\frac{5}{2}\frac{(\mathbf{r}_1\cdot\mathbf{r}_2)^3}{r_2^6} - \frac{3}{2}\frac{r_1^2(\mathbf{r}_1\cdot\mathbf{r}_2)}{r_2^4}]. \quad (3.4)$$

Double averaging the equations of motion over the mean anomalies of the inner and outer bodies (see Appendix B for more detail), the following equations for the averaged quadrupole and octupole potential are obtained:

$$\langle\Phi_{\rm quad}\rangle = \frac{\phi_0}{(1-e_2^2)^{3/2}}[\frac{1}{2}(1-e_1^2)(\hat{\mathbf{k}}_1\cdot\hat{\mathbf{k}}_2)^2 + (e_1^2 - \frac{1}{6}) - \frac{5}{2}(\mathbf{e}_1\cdot\hat{\mathbf{k}}_2)^2], \quad (3.5)$$

$$\begin{aligned}\langle\Phi_{\rm oct}\rangle &= \frac{25\epsilon\phi_0}{16(1-e_2^2)^{3/2}}\{\mathbf{e}_1\cdot\hat{\mathbf{e}}_2[(\frac{1}{5} - \frac{8}{5}e_1^2) - (1-e_1^2)(\hat{\mathbf{k}}_1\cdot\hat{\mathbf{k}}_2)^2 + 7(\mathbf{e}_1\cdot\hat{\mathbf{k}}_2)^2] \\ &\quad -2(1-e_1^2)(\hat{\mathbf{k}}_1\cdot\hat{\mathbf{k}}_2)(\mathbf{e}_1\cdot\hat{\mathbf{k}}_2)(\hat{\mathbf{k}}_1\cdot\mathbf{e}_2)\}, \quad (3.6)\end{aligned}$$

where

$$\phi_0 = \frac{3G}{4}\frac{m_0 m_1 m_2}{m_0+m_1}\frac{a_1^2}{a_2^3}, \tag{3.7}$$

$$\epsilon = \frac{m_0-m_1}{m_0+m_1}\frac{a_1}{a_2}\frac{e_2}{1-e_2^2}. \tag{3.8}$$

In the above expressions, ϵ gives the relative significance of the octupole term in the potential.

The orbital evolution can be tracked by two parameters. One is the orbital angular momentum:

$$\mathbf{G}_i = \beta_i\sqrt{\mu_i a_i(1-e_i^2)}\hat{\mathbf{k}}_i, \tag{3.9}$$

where $i = 1, 2$ refer to the inner and outer orbits, and $\hat{\mathbf{k}}_i$ is the unit vector of $\mathbf{G}_i$ with $\beta_1 = m_0 m_1/(m_0+m_1)$, $\beta_2 = (m_0+m_1)m_2/(m_0+m_1+m_2)$, $\mu_1 = G(m_0+m_1)$ and $\mu_2 = G(m_0+m_1+m_2)$, respectively. The other is the Lenz vector of the inner and outer orbits, which points along the direction of the pericenter with the magnitude e:

$$\mathbf{e}_i = \frac{(\dot{\mathbf{r}}_i \times \mathbf{G}_i)}{\beta_i\mu_i} - \frac{\mathbf{r}_i}{r_i}. \tag{3.10}$$

The corresponding equations of motion of the orbital vectors $\mathbf{G}_1$, $\mathbf{G}_2$, $\mathbf{e}_1$, and $\mathbf{e}_2$ for the conservative motion are

$$\dot{\mathbf{G}}_1 = -\left(\frac{\mathbf{G}_1}{\beta_1\sqrt{\mu_1 a_1}} \times \bigtriangledown_{\frac{\mathbf{G}_1}{\beta_1\sqrt{\mu_1 a_1}}}\langle\Phi\rangle + \mathbf{e}_1 \times \bigtriangledown_{\mathbf{e}_1}\langle\Phi\rangle\right), \tag{3.11}$$

$$\dot{\mathbf{G}}_2 = -\left(\frac{\mathbf{G}_2}{\beta_2\sqrt{\mu_2 a_2}} \times \bigtriangledown_{\frac{\mathbf{G}_2}{\beta_2\sqrt{\mu_2 a_2}}}\langle\Phi\rangle + \mathbf{e}_2 \times \bigtriangledown_{\mathbf{e}_2}\langle\Phi\rangle\right), \tag{3.12}$$

$$\dot{\mathbf{e}}_1 = -\frac{1}{\beta_1\sqrt{\mu_1 a_1}}\left(\frac{\mathbf{G}_1}{\beta_1\sqrt{\mu_1 a_1}} \times \bigtriangledown_{\mathbf{e}_1}\langle\Phi\rangle + \mathbf{e}_1 \times \bigtriangledown_{\frac{\mathbf{G}_1}{\beta_1\sqrt{\mu_1 a_1}}}\langle\Phi\rangle\right), \tag{3.13}$$

$$\dot{\mathbf{e}}_2 = -\frac{1}{\beta_2\sqrt{\mu_2 a_2}}\left(\frac{\mathbf{G}_2}{\beta_2\sqrt{\mu_2 a_2}} \times \bigtriangledown_{\mathbf{e}_2}\langle\Phi\rangle + \mathbf{e}_2 \times \bigtriangledown_{\frac{\mathbf{G}_2}{\beta_2\sqrt{\mu_2 a_2}}}\langle\Phi\rangle\right). \tag{3.14}$$

In the above expressions, nabla is a vector differential operator in the direction of the subscript vector. The result is a vector perpendicular to the subscript vector. Substituting the averaged potential in equations (3.5) and (3.6) to equations (3.11) to (3.14), the

equations of motion up to the octupole order can be obtained as

$$\begin{aligned}
\dot{\mathbf{G}}_{1,\mathrm{oct}} &= -\gamma(1-e_1^2)\cos i_{12}\hat{\mathbf{k}}_2\times\hat{\mathbf{k}}_1+5\gamma(\mathbf{e}_1\cdot\hat{\mathbf{k}}_2)\hat{\mathbf{k}}_2\times\mathbf{e}_1 \\
&\quad -\frac{25}{16}\epsilon_{\mathrm{pl}}\gamma\Bigg\{\Big[2(1-e_1^2)[(\mathbf{e}_1\cdot\hat{\mathbf{e}}_2)\cos i_{12}+(\mathbf{e}_1\cdot\hat{\mathbf{k}}_2)(\hat{\mathbf{k}_1}\cdot\hat{\mathbf{e}}_2)]\hat{\mathbf{k}}_1 \\
&\quad +2[(1-e_1^2)(\hat{\mathbf{k}_1}\cdot\hat{\mathbf{e}}_2)\cos i_{12}-7(\mathbf{e}_1\cdot\hat{\mathbf{k}}_2)(\mathbf{e}_1\cdot\hat{\mathbf{k}}_2)]\mathbf{e}_1\Big]\times\hat{\mathbf{k}}_2 \\
&\quad +\Big[2(1-e_1^2)(\mathbf{e}_1\cdot\hat{\mathbf{k}}_2)\cos i_{12}\hat{\mathbf{k}}_1+[\frac{8}{5}\mathbf{e}_1^2-\frac{1}{5} \\
&\quad -7(\mathbf{e}_1\cdot\hat{\mathbf{k}}_2)^2+(1-e_1^2)\cos^2 i_{12}]\mathbf{e}_1\Big]\times\hat{\mathbf{e_2}}\Bigg\}, \qquad (3.15)
\end{aligned}$$

$$\begin{aligned}
\dot{\mathbf{G}}_{2,\mathrm{oct}} &= -\gamma(1-e_1^2)\cos i_{12}\hat{\mathbf{k}}_1\times\hat{\mathbf{k}}_2+5\gamma(\mathbf{e}_1\cdot\hat{\mathbf{k}}_2)\mathbf{e}_1\times\hat{\mathbf{k}}_2 \\
&\quad +\frac{25}{16}\epsilon_{\mathrm{pl}}\gamma\Bigg\{\Big[2(1-e_1^2)[(\mathbf{e}_1\cdot\hat{\mathbf{e}}_2)\cos i_{12}+(\mathbf{e}_1\cdot\hat{\mathbf{k}}_2)(\hat{\mathbf{k}_1}\cdot\hat{\mathbf{e}}_2)]\hat{\mathbf{k}}_1 \\
&\quad +2[(1-e_1^2)(\hat{\mathbf{k}_1}\cdot\hat{\mathbf{e}}_2)\cos i_{12}-7(\mathbf{e}_1\cdot\hat{\mathbf{k}}_2)(\mathbf{e}_1\cdot\hat{\mathbf{k}}_2)]\mathbf{e}_1\Big]\times\hat{\mathbf{k}}_2 \\
&\quad +\Big[2(1-e_1^2)(\mathbf{e}_1\cdot\hat{\mathbf{k}}_2)\cos i_{12}\hat{\mathbf{k}}_1+[\frac{8}{5}\mathbf{e}_1^2-\frac{1}{5} \\
&\quad -7(\mathbf{e}_1\cdot\hat{\mathbf{k}}_2)^2+(1-e_1^2)\cos^2 i_{12}]\mathbf{e}_1\Big]\times\hat{\mathbf{e_2}}\Bigg\}, \qquad (3.16)
\end{aligned}$$

$$\begin{aligned}
\dot{\mathbf{e}}_{1,\mathrm{oct}} &= -\frac{\gamma(1-e_1^2)}{||\mathbf{G}_1||}\Big[\cos i_{12}\hat{\mathbf{k}}_2\times\mathbf{e}_1-2\hat{k}_1\times\mathbf{e}_1-5(\mathbf{e}_1\cdot\hat{\mathbf{k}}_2)\hat{\mathbf{k}}_2\times\hat{\mathbf{k}}_1\Big] \\
&\quad -\frac{25}{16}\epsilon_{\mathrm{pl}}\gamma\Bigg\{2\sqrt{(1-e_1^2)}\Big[(\mathbf{e}_1\cdot\hat{\mathbf{k}}_2)\cos i_{12}\mathbf{e}_1 \\
&\quad +[\frac{8}{5}\mathbf{e}_1^2-\frac{1}{5}-7(\mathbf{e}_1\cdot\hat{\mathbf{k}}_2)^2+(1-e_1^2)\cos^2 i_{12}]\hat{\mathbf{k}}_1\Big]\times\hat{\mathbf{e_2}} \\
&\quad +2\sqrt{(1-e_1^2)}\Big[[(\mathbf{e}_1\cdot\hat{\mathbf{e}}_2)\cos i_{12}+(\mathbf{e}_1\cdot\hat{\mathbf{k}}_2)(\hat{\mathbf{k}_1}\cdot\hat{\mathbf{e}}_2)]\mathbf{e}_1 \\
&\quad +[(\hat{\mathbf{k}_1}\cdot\hat{\mathbf{e}}_2)\cos i_{12}-7(\mathbf{e}_1\cdot\hat{\mathbf{k}}_2)(\mathbf{e}_1\cdot\hat{\mathbf{e}}_2)]\hat{\mathbf{k}}_1\Big]\times\hat{\mathbf{k}}_2 \\
&\quad +\frac{16}{5}(\mathbf{e}_1\cdot\hat{\mathbf{e}}_2)\sqrt{(1-e_1^2)}\mathbf{k}_1\times\mathbf{e}_1\Bigg\}, \qquad (3.17)
\end{aligned}$$

$$\begin{aligned}
\dot{\mathbf{e}}_{2,\rm oct} &= \frac{\gamma}{\sqrt{1-e_2^2}}\frac{\beta_1\sqrt{\mu_1 a_1}}{\beta_2\sqrt{\mu_2 a_2}}\Big[(1-e_1^2)\cos i_{12}\mathbf{e}_2\times\ \hat{\mathbf{k}}_1 - 5(\mathbf{e}_1\cdot\hat{\mathbf{k}}_2)\mathbf{e}_2\times\mathbf{e}_1 \\
&\quad -[\frac{1}{2}-3e_1^2+\frac{25}{2}(\mathbf{e}_1\cdot\hat{\mathbf{k}}_2)^2-\frac{5}{2}(1-e_1^2)\cos^2 i_{12}]\hat{\mathbf{k}}_2\times\mathbf{e}_2\Big] \\
&\quad -\frac{25}{16}\epsilon_{\rm pl}\gamma\sqrt{1-e_2^2}\frac{\beta_1\sqrt{\mu_1 a_1}}{\beta_2\sqrt{\mu_2 a_2}}\Bigg\{2(1-e_1^2)\Big[(\mathbf{e}_1\cdot\hat{\mathbf{k}}_2)(\hat{\mathbf{k}}_1\cdot\mathbf{e}_2)\hat{\mathbf{e}}_2 \\
&\quad +\frac{1-e_2^2}{e_2}[\frac{8}{5}\mathbf{e}_1^2-\frac{1}{5}-7(\mathbf{e}_1\cdot\hat{\mathbf{k}}_2)^2+(1-e_1^2)\cos^2 i_{12}]\hat{\mathbf{k}}_2\Big]\times\mathbf{e}_1 \\
&\quad -\Big[2(\frac{1}{5}-\frac{8}{5}\mathbf{e}_1^2)(\mathbf{e}_1\cdot\hat{\mathbf{e}}_2)\mathbf{e}_2+14(1-e_1^2)(\mathbf{e}_1\cdot\hat{\mathbf{k}}_2)(\hat{\mathbf{k}}_1\cdot\hat{\mathbf{e}}_2)(\hat{\mathbf{k}}_1\cdot\hat{\mathbf{k}}_2)\mathbf{e}_2 \\
&\quad +7(\mathbf{e}_1\cdot\hat{\mathbf{e}}_2)[\frac{8}{5}\mathbf{e}_1^2-\frac{1}{5}-7(\mathbf{e}_1\cdot\hat{\mathbf{k}}_2)^2+(1-e_1^2)\cos^2 i_{12}]\mathbf{e}_2\Big]\times\hat{\mathbf{k}}_2)\Bigg\}, \quad (3.18)
\end{aligned}$$

where

$$\gamma = \frac{3Gm_2\beta_1 a_1^2}{4a_2^3(1-e_2^2)^{3/2}}. \quad (3.19)$$

The mutual orbital inclination, i_{12}, is defined by

$$\cos i_{12} = \hat{\mathbf{k}}_1\cdot\hat{\mathbf{k}}_2. \quad (3.20)$$

Since equations (3.15) to (3.18) are ordinary differential equations, $\mathbf{G}_1$, $\mathbf{G}_2$, $\mathbf{e}_1$ and $\mathbf{e}_2$ can be integrated numerically by the Embedded Runge-Kutta method described in Appendix I once initial values are given.

Validity of Double Average

Double average method removes the short-term effects which have period smaller than the outer orbit. Therefore, any modulation over this timescale is neglected. The validity of double average method has been tested by many authors. Very recently, Luo et al. (2016) found that double averaged equations are in good agreement with the direct N-body integration when $m_2/(m_0+m_1) < 0.1$. However, itself fails to characterize the orbital evolution for a relatively massive perturber when m_2 is comparable with (m_0+m_1) due to the long term accumulation of the short-term errors. Throughout this thesis, the perturber mass we adopt satisfies the criterion $m_2/(m_0+m_1) < 0.1$, thus double average method is robust in our simulation.

3.1.2 Extreme Eccentricity Condition in CHEM

As described in subsection 2.4.1, Li et al. (2014) found that in a near-coplanar eccentric hierarchical triple configuration, the secular interaction between two orbits leads the eccentricity of the inner planet reaching an extremely high value, and the inner orbit flips by $\sim 180^\circ$. Subsequent tides circularize the inner orbit to create a HJ.

Such orbit flip behavior are accompanied with the extremely high eccentricity of the inner body, which can be understood analytically. The extreme eccentricity condition is defined such that the eccentricity of the inner planet, e_1, reaches unity in a near-coplanar hierarchical triple system. Since the extreme eccentricity is associated with the $\sim 180^\circ$ orbital flip for point masses interacting only through the gravity (Li et al. 2014), the above condition is often referred to as the flip condition, but we do not use the latter in order to avoid confusion.

Petrovich (2015b) derived the extreme eccentricity condition from the double time-averaged gravitational interaction potential. In the coplanar limit ($\hat{\mathbf{k}}_i \cdot \hat{\mathbf{k}}_j = 1$, $\mathbf{e}_i \cdot \hat{\mathbf{k}}_j = 0$, for $i, j = 1, 2$), the averaged potential in equations (3.5) and (3.6) reduce to

$$\tilde{\phi} \equiv \frac{\langle \Phi \rangle}{\phi_0} = \frac{e_1^2 + 2/3}{2(1-e_2^2)^{3/2}} - \frac{5\epsilon}{16} \frac{4 + 3e_1^2}{(1-e_2)^{3/2}} e_1 \cos\varpi, \tag{3.21}$$

where ϖ is defined as $\varpi \equiv \cos^{-1} \hat{\mathbf{e}}_1 \cdot \hat{\mathbf{e}}_2$, the angle between the inner and outer unit Lenz vectors. Here we assume the exact coplanarity of the system just for simplicity. The extreme eccentricity condition can be derived from the conservation of the potential energy up to the octupole order combined with the total orbital angular momentum conservation.

The ratio to characterize the total orbital angular momentum departure from circularity is defined as

$$J = \frac{\mu\alpha^{1/2}(1-e_1^2)^{1/2} + (1-e_2^2)^{1/2}}{\mu\alpha^{1/2} + 1}, \tag{3.22}$$

where μ is the mass ratio between the inner and outer body m_1/m_2, α is the semi-major axis ratio between the inner and outer body a_1/a_2. This ratio, J, is a constant in the octupole approximation.

In the test particle limit ($m_1 \ll m_0$, $m_1 \ll m_2$), e_2 is constant since the effect of m_1 on m_2 is neglected. Thus, the extreme eccentricity condition can be obtained by simply setting $e_{1,f} = 1$ in equation (3.21). The result becomes

$$\epsilon_{\rm pl} > \frac{8}{5} \frac{1 - e_{1,i}^2}{7\cos\varpi_f - e_{1,i}(4 + 3e_{1,i}^2)\cos\varpi_i}, \tag{3.23}$$

where

$$\epsilon_{\rm pl} \equiv \frac{a_1}{a_2} \frac{e_2}{1 - e_2^2}. \tag{3.24}$$

Here $\epsilon_{\rm pl}$ is the reduced version of ϵ in equation (3.8) in the limit of $m_1 \ll m_0$. The subscripts i and f refer to the initial and final states, respectively. Equation (3.23) is first derived by Li et al. (2014) using a slightly different approach.

Petrovich (2015b) generalized the extreme eccentricity condition in the planetary limit ($m_1 \ll m_0$, $m_1 \leq m_2$). In this limit, equation (3.21) reduces to equation (1) of

Petrovich (2015b):

$$\tilde{\phi}_{\rm pl} = \frac{e_1^2 + 2/3}{2(1-e_2^2)^{3/2}} - \frac{5\epsilon_{\rm pl}}{16}\frac{4+3e_1^2}{(1-e_2)^{3/2}} e_1 \cos\varpi. \tag{3.25}$$

Assuming the conservation of the potential up to the octupole order, the extreme eccentricity condition where $e_{1,f}$ reaches unity is written as

$$\tilde{\phi}_{\rm pl}(e_{1,i}, e_{2,i}, \epsilon_{\rm pl,i}, \varpi_i = \pi) \;=\; \tilde{\phi}_{\rm pl}(e_{1,f} = 1, e_{2,f}, \epsilon_{\rm pl,f}, \varpi_f), \tag{3.26}$$

where we set $\varpi_i = \pi$ for definiteness. Equation (3.26) can be numerically solved along with the angular momentum conservation. Then, we obtain the range of $\epsilon_{\rm pl,i}$ such that $e_{1,f}$ can reach unity as the function of $e_{1,i}$, $e_{2,i}$, and ϖ_f. The lower and upper boundaries of the condition correspond to $\varpi_f = 0$ and π in practice. Thus, equation (3.26) puts constraints on $\epsilon_{\rm pl,i}$ as:

$$\epsilon_{\rm L} < \epsilon_{\rm pl,i} \equiv \frac{a_{1,i}}{a_{2,i}}\frac{e_{2,i}}{1-e_{2,i}^2} < \epsilon_{\rm U}. \tag{3.27}$$

Petrovich (2015b) examined equation (3.26) and found that the required $e_{2,i}$ for $e_{1,f} \to 1$ decreases with increasing of $a_{1,i}/a_{2,i}$ and $e_{1,i}$. He also realized the existence of the upper boundary for the extreme eccentricity condition, corresponding to $\epsilon_{\rm U}$ in equation (3.27). Nevertheless, he did not examine it in detail. In reality, however, $\epsilon_{\rm U}$ is very important to determine the extreme eccentricity region when m_1 is comparable to m_2 as we will present in subsection 4.2.1.

3.2 Basic Equations of SRFs

Short-range forces (SRFs) include general relativity (GR), stellar and planetary non-dissipative tides, and stellar and planetary rotational distortion. As described in subsection 2.4.2, those short-range forces may significantly affect the dynamical evolution of the inner planet. Therefore, incorporating SRFs is necessary to properly describe the orbital evolution in CHEM. In this section, we review the basic equations of SRFs following Liu et al. (2015) and Correia et al. (2011).

The first order post-Newtonian potential can be written as

$$\langle \Phi_{\rm GR} \rangle = -\frac{3G^2 m_0 m_1 (m_0+m_1)}{a_1^2 c^2}\frac{1}{(1-e_1^2)^{1/2}}, \tag{3.28}$$

where c is the speed of light. The correction due to GR induces the precession of the pericenter:

$$\dot{\mathbf{e}}_{1,\rm GR} = \frac{3\mu_1 n_1}{c^2 a_1 (1-e_1^2)}\hat{\mathbf{k}}_1 \times \mathbf{e}_1, \tag{3.29}$$

where n_1 is mean motion of the inner orbit.

The potential associated with the non-dissipative tidal bulge on the inner binary is:

$$\langle \Phi_{\rm tide,i} \rangle = -\frac{G}{a_1^6} \frac{1+3e_1^2+\frac{3}{8}e_1^4}{(1-e_1^2)^{9/2}} (m_{1-i}^2 k_{2,i} R_i^5), \tag{3.30}$$

where $i = 0, 1$ denote the central star and inner planet. The additional pericenter precession of $\mathbf{e}_1$ due to non-dissipative tides is

$$\dot{\mathbf{e}}_{1,\rm nd-tide} = \sum_i \frac{15}{2} k_{2,i} n_1 \left(\frac{m_{1-i}}{m_i}\right) \left(\frac{R_i}{a_1}\right)^5 \frac{1+3e^2/2+e^4/8}{(1-e^2)^5} \hat{\mathbf{k}}_1 \times \mathbf{e}_1. \tag{3.31}$$

The potential energy due to the rotation-induced oblateness of the inner binary are

$$\langle \Phi_{\rm rot,i} \rangle = -\frac{G m_0 (I_3 - I_1)_1}{2 a_1^3 (1-e_1^2)^{3/2}}. \tag{3.32}$$

In the above expressions,

$$(I_3 - I_1)_1 = k_{2,i} m_1 R_1^2 (\frac{\Omega_i^2}{3Gm_i/R_i^3}), \tag{3.33}$$

where Ω_i refers to the spin rate, and $k_{2,i}$ is the second Love number that characterizes the deformation property of each body.

In the quadrupole approximation, the precession due to rotational distortion can be derived following Correia et al. (2011). The gravity coefficients $J_{2,i}$ for the star ($i = 0$) and inner planet ($i = 1$) are written as

$$J_{2,i} = k_{2,i} \frac{\Omega_i^2 R_i^3}{3Gm_i}. \tag{3.34}$$

The spin angular momentum is

$$\mathbf{L}_i = C_i \Omega_i \hat{\mathbf{s}}_i, \tag{3.35}$$

where $\hat{\mathbf{s}}_i$ is the unit vector of $\mathbf{L}_i$, and C_i is the principal moment of inertia. The averaged equation of rotational distortion can be written as

$$\dot{\mathbf{G}}_{1,\rm rot} = -\sum_i \alpha_{1i} (\hat{\mathbf{s}}_i \cdot \hat{\mathbf{k}}_1) \hat{\mathbf{s}}_i \times \hat{\mathbf{k}}_1, \tag{3.36}$$

$$\dot{\mathbf{G}}_{2,\rm rot} = -\sum_i \alpha_{2i} (\hat{\mathbf{s}}_i \cdot \hat{\mathbf{k}}_2) \hat{\mathbf{s}}_i \times \hat{\mathbf{k}}_2, \tag{3.37}$$

$$\dot{\mathbf{e}}_{1,\rm rot} = -\sum_i \frac{\alpha_{1i}}{||\mathbf{G}_1||} \left[(\hat{\mathbf{s}}_i \cdot \hat{\mathbf{k}}_1) \hat{\mathbf{s}}_i \times \mathbf{e}_1 + \frac{1}{2} (1 - 5(\hat{\mathbf{s}}_i \cdot \hat{\mathbf{k}}_1)^2) \hat{\mathbf{k}}_1 \times \mathbf{e}_1 \right], \tag{3.38}$$

$$\dot{\mathbf{L}}_{i,\mathrm{rot}} = \alpha_{1i}(\hat{\mathbf{s}}_i \cdot \hat{\mathbf{k}}_1)\ \hat{\mathbf{s}}_i \times \hat{\mathbf{k}}_1 + \alpha_{2i}(\hat{\mathbf{s}}_i \cdot \hat{\mathbf{k}}_2)\hat{\mathbf{s}}_i \times \hat{\mathbf{k}}_2, \tag{3.39}$$

where

$$\alpha_{1i} = \frac{3Gm_0m_1J_{2i}R_i^2}{2a_1^3(1-e_1^2)^{3/2}}, \tag{3.40}$$

$$\alpha_{2i} = \frac{3Gm_2m_iJ_{2i}R_i^2}{2a_2^3(1-e_2^2)^{3/2}}. \tag{3.41}$$

In addition to SRFs effect, the magnetic braking as a spin-down process of the central star may also potentially play an important role on the dynamical evolution. It is modeled as (Barker & Ogilvie 2009):

$$\dot{\mathbf{L}}_{0,\mathrm{mb}} = -\alpha_{\mathrm{mb}}C_0\Omega_0^3\hat{\mathbf{s}}_0, \tag{3.42}$$

where the spin-down rate α_{mb} is set to 1.66×10^{-13} yr according to Barker & Ogilvie (2009).

3.3 Basic Equations of Tides

As described in section 2.5, tides play an important role on the spin and orbital evolution of planetary systems. In this section, we review the basic equations of two tidal models in planetary systems: the conventional equilibrium tide model and the Lai model.

3.3.1 Equilibrium Tide Model

As described in subsection 2.5.1, in the equilibrium tide model, the orbital separation between the interacting bodies, the central star and innermost planet, is roughly constant and slowly varied tides generate an equilibrium figure. The viscosity due to tides leads to dissipation. And the followed energy and angular momentum exchange lead to circularization, synchronization, and spin-orbit alignment. The dissipation of the mechanical energy can be parameterized as the tidal delay time Δt_i. In this subsection, we review the basic equations of the equilibrium tide model following Correia et al. (2011) and Lai (2012).

The tidal potential for the inner pair is (Kaula 1964):

$$U_T = -\frac{G}{r_1^3}\sum_{i=0,1} k_{2,i}m_{(1-i)}^2\frac{R_i^5}{r_1'^3}P_2(\hat{\mathbf{r}}_1 \cdot \hat{\mathbf{r}}_1'), \tag{3.43}$$

where $\hat{\mathbf{r}}_1'$ is the position at Δt_i time delay. This can be made linear (Mignard 1979):

$$\hat{\mathbf{r}}_1' \approx \hat{\mathbf{r}}_1 + \Delta t_i(\Omega_i\hat{\mathbf{s}}_i \times \hat{\mathbf{r}}_1 - \dot{\mathbf{r}}_1). \tag{3.44}$$

Then, the equations of tidal evolution can be obtained by averaging the equations of motion over the mean anomaly (Correia et al. 2011):

$$\dot{\mathbf{G}}_{1,\rm tide} = -\dot{\mathbf{L}}_0 - \dot{\mathbf{L}}_1, \qquad \dot{\mathbf{G}}_{2,\rm tide} = 0, \tag{3.45}$$

$$\begin{aligned}
\dot{\mathbf{e}}_{1,\rm tide} &= \sum_i \frac{15}{2} k_{2,i} n_1 \left(\frac{m_{(1-i)}}{m_i}\right)\left(\frac{R_i}{a_1}\right)^5 f_4(e_1)\hat{\mathbf{k}}_1 \times \mathbf{e}_1 \\
&\quad - \sum_i \frac{K_i}{\beta_1 a_1^2}\left[f_4(e_1)\frac{\Omega_i}{2n_1}(\mathbf{e}_1\cdot\hat{\mathbf{s}}_i)\hat{\mathbf{k}}_1 - \left(\frac{11}{2}f_4(e_1)(\hat{\mathbf{s}}_i\cdot\hat{\mathbf{k}}_1)\frac{\Omega_i}{n_1} - 9f_5(e_1)\right)\mathbf{e}_1\right] \qquad (3.46)\\
\dot{\mathbf{L}}_{i,\rm tide} &= K_i n_1 \left[f_4(e_1)\sqrt{1-e_1^2}\frac{\Omega_i}{2n_1}(\hat{\mathbf{s}}_i - (\hat{\mathbf{s}}_i\cdot\hat{\mathbf{k}}_1)\hat{\mathbf{k}}_1)\right. \\
&\quad \left. - f_1(e_1)\frac{\Omega_i}{n_1}\hat{\mathbf{s}}_i + f_2(e_1)\hat{\mathbf{k}}_1 + \frac{(\mathbf{e}_1\cdot\hat{\mathbf{s}}_i)(6+e_1^2)}{4(1-e_1^2)^{9/2}}\frac{\Omega_i}{n_1}\mathbf{e}_1\right], \qquad (3.47)
\end{aligned}$$

where

$$K_i = \Delta t_i \frac{3k_{2,i}Gm_{(1-i)}^2 R_i^5}{a_1^6}, \tag{3.48}$$

$$f_1(e) = \frac{1+3e^2+3e^4/8}{(1-e^2)^{9/2}}, \tag{3.49}$$

$$f_2(e) = \frac{1+15e^2/2+45e^4/8+5e^6/16}{(1-e^2)^6}, \tag{3.50}$$

$$f_3(e) = \frac{1+31e^2/2+255e^4/8+185e^6/16+25e^8/64}{(1-e^2)^{15/2}}, \tag{3.51}$$

$$f_4(e) = \frac{1+3e^2/2+e^4/8}{(1-e^2)^5}, \tag{3.52}$$

$$f_5(e) = \frac{1+15e^2/4+15e^4/8+5e^6/64}{(1-e^2)^{13/2}}. \tag{3.53}$$

In the above expressions, the subscript tide refers to the term of the equilibrium tide with constant Δt model.

For various theoretically based motivations, the characteristic parameter of equilibrium tides can be parameterized as the quality factor Q_i or the viscous timescale $t_{v,i}$ instead of the tidal delay time Δt_i, where $1/Q_i = 2|\Omega_i - n_1|\Delta t_i$[1], and $t_{v,i} = 3(1+k_{2,i})R_i^3/(Gm_i\Delta t_i)$.

It is difficult to determine the viscous timescale (also the tidal delay time and the tidal quality factor) in the equilibrium tide model since it is related to the internal structure. The constraint from Jupiter-Io system gives that the lower limit on the viscous timescale

[1]The forcing frequency $2|\Omega_i - n_1|$ corresponds to the semi-diurnal tides, which are dominant for the eccentric orbit.

of Jupiter is $t_{v,J} > 15$ yr. However, Socrates et al. (2012) claimed that for an initially highly eccentric planetary orbit at $a \sim 5$ AU, an upper limit for the viscous timescale of the planet $t_{\rm v,p} < 1.5$ yr is required to circularize the orbit into a final $a = 0.06$ AU within 10 Gyr. Nevertheless, given the uncertainties in the models of tidal dissipation and the physical properties of the exoplanets, this discrepancy between the results of Socrates et al. (2012) and Jupiter-Io system may not pose a severe problem for high-e migration.

If one neglects the eccentricity, GR, and non-dissipative tides, they lead to the following simplified equations for the semi-major axis a, the spin angular frequency $\Omega_{\rm s}$, and the spin-orbit angle ψ in the equilibrium tide model (e.g., Lai 2012):

$$\frac{(\dot{a})_{\rm e}}{a} = -\frac{1}{\tau_{\rm e}}\left(1 - \frac{\Omega_{\rm s}}{\Omega_{\rm orb}}\cos\psi\right), \tag{3.54}$$

$$\frac{(\dot{\Omega}_{\rm s})_{\rm e}}{\Omega_{\rm s}} = \frac{1}{\tau_{\rm e}}\left(\frac{G}{2L}\right)\left[\cos\psi - \frac{\Omega_{\rm s}}{2\Omega_{\rm orb}}(1+\cos^2\psi)\right], \tag{3.55}$$

$$(\dot{\psi})_{\rm e} = -\frac{1}{\tau_{\rm e}}\left(\frac{G}{2L}\right)\sin\psi\left[1 - \frac{\Omega_{\rm s}}{2\Omega_{\rm orb}}\left(\cos\psi - \frac{L}{G}\right)\right], \tag{3.56}$$

where subscript e refers to the term of the equilibrium tide model, $\Omega_{\rm orb}$ is the orbital angular frequency, $\Omega_{\rm s}$ is the spin rotation rate of the central star, and G and L refer to the value of the orbital and stellar spin angular momentum. $\tau_{\rm e}$ is the damping timescale, which is written as

$$\begin{aligned}\tau_{\rm e} &= \left(\frac{Q_{\rm e}}{3k_2}\right)\left(\frac{m_{\rm s}}{m_{\rm p}}\right)\left(\frac{a}{R_{\rm s}}\right)^5\Omega_{\rm orb}^{-1} \\ &\approx 1.3\left(\frac{Q_{\rm e}/3k_2}{2\times10^6}\right)\left(\frac{m_{\rm s}}{10^3 m_{\rm p}}\right)\left(\frac{\bar{\rho}_{\rm s}}{\bar{\rho}_\odot}\right)^{5/3}\left(\frac{P_{\rm p}}{1{\rm day}}\right)^{13/3}{\rm Gyr},\end{aligned} \tag{3.57}$$

where $m_{\rm s}$ and $R_{\rm s}$ correspond to the mass and radius of the central star, $P_{\rm p}$ is the orbital period of the planet, $Q_{\rm e}$ is the tidal quality factor of the central star, $\bar{\rho}_{\rm s}$ is the mean density of the central star, and k_2 is the second Love number of the central star.

3.3.2 Lai Model

Lai (2012) pointed out the importance of inertial wave dissipation of the star that are driven by the Coriolis force. The inertial wave excitation becomes important when the stellar spin angular momentum $\mathbf{L}$ is misaligned with the orbital angular momentum $\mathbf{G}$. As described in subsection 2.5.4, the Lai model was proposed to track the equilibrium tide problem. In this subsection, we review the basic equations of the inertial wave dissipation as below.

For a star-planet system in circular orbit, the tidal potential has two components to the quadrupole order in the spherical coordinate system with the z-axis along $\mathbf{G}$, with frequencies $\omega_{m'} = m'\Omega_{\rm orb}$, where $m' = 0, 2$, and $\Omega_{\rm orb}$ is the orbital mean motion. In the co-rotating frame of the star, the forcing frequencies become

$$\tilde{\omega}_{mm'} = m'\Omega_{\rm orb} - m\Omega_{\rm s}, \tag{3.58}$$

where $m = 0, \pm 1, \pm 2$, and $\Omega_{\rm s}$ is the spin rotation rate of the central star.

The tidal potential produced by the planet orbiting at $\mathbf{r}$ in terms of spherical harmonics in a frame centered at the star with the z-axis along the stellar spin $\mathbf{L}$:

$$U_2(\mathbf{r}, t) = -\sum_{m,m'} U_{mm'}(m_{\rm p}, \psi) r^2 Y_{2m}(\theta, \phi) e^{-im'\Omega_{\rm orb}t}, \tag{3.59}$$

where the index $m' = 0, \pm 2$ refer to that of spherical harmonics $Y_{2m'}(\theta_{\rm L}, \phi_{\rm L})$ defined in the coordinate with its z-axis along the planetary orbital angular momentum $\mathbf{L}$, ψ is the spin-orbit angle, and $m_{\rm p}$ corresponds to the planetary mass. Lai (2012) pointed out that in the limit of $\Omega_{\rm orb} \gg \Omega_{\rm s}$, the only tidal forcing component for exciting inertial waves in the star is that associated with $(m, m') = (1, 0)$. The tidal torque associated with this component contributes to spin-orbit angle realignment but not orbital decay.

The corresponding tidal torque components due to such dynamical tides are given in Lai (2012) as

$$T_{10,x} = \frac{3k_{10}}{4Q_{10}} T_0 \sin\psi \cos^3\psi, \tag{3.60}$$

$$T_{10,y} = -\frac{3k_{10}}{16} T_0 \sin 4\psi, \tag{3.61}$$

$$T_{10,z} = -\frac{3k_{10}}{4Q_{10}} T_0 (\sin\psi \cos\psi)^2, \tag{3.62}$$

where k_{10} and Q_{10} are the dimensionless tidal Love number and tidal quality factor corresponding to the (1,0) component, and

$$T_0 = G \left(\frac{m_{\rm p}}{a^3}\right)^2 R_{\rm s}^5 \tag{3.63}$$

(c.f., Murray & Dermott 1999).

We note here that Lai (2012) chooses the y-direction along the direction $\mathbf{L} \times \mathbf{G}$. Thus $T_{10,y}$ does not change the spin-orbit elements, contributing to the spin precession, but we compute $T_{10,y}$ on the basis of equation (20) of Lai (2012) in any case. Up to the leading-order of the delay time, $T_{10,y}$ does not depend on Q_{10} unlike $T_{10,x}$ nor $T_{10,z}$.

From the corresponding tidal torques due to the inertial wave dissipation described above, Lai (2012) derived the following equations for a, $\Omega_{\rm s}$, and ψ:

$$(\dot{a})_{10} = 0, \tag{3.64}$$

$$\frac{(\dot{\Omega}_{\rm s})_{10}}{\Omega_{\rm s}} = -\frac{1}{\tau_{10}} (\sin\psi \cos\psi)^2, \tag{3.65}$$

$$(\dot{\psi})_{10} = -\frac{1}{\tau_{10}} \sin\psi \cos^2\psi \left(\cos\psi + \frac{L}{G}\right). \tag{3.66}$$

In the above equations, τ_{10} is the characteristic tidal damping timescale corresponding to the (1,0) component[2]:

$$\begin{aligned}\tau_{10} &= \left(\frac{4Q_{10}}{3k_{10}}\right)\left(\frac{m_{\rm s}}{m_{\rm p}}\right)\left(\frac{a}{R_{\rm s}}\right)^5\left(\frac{L}{G}\right)\Omega_{\rm p}^{-1} \\ &= 4\left(\frac{Q_{10}}{Q_{\rm e}}\right)\left(\frac{k_2}{k_{10}}\right)\left(\frac{L}{G}\right)\tau_{\rm e}. \end{aligned} \tag{3.67}$$

Thus, the inertial wave dissipation adds the damping terms with the timescale of τ_{10} for ψ and Ω_s, while the planetary orbit is unaffected since the (1,0) component of the tidal potential is static in the inertial frame (Lai 2012). Thus in this model the spin-orbit angle aligns faster before the planet falls into the central star, or more strictly, closer to its Roche limit $\approx 2.7R_{\rm s}(\bar{\rho}_{\rm s}/\bar{\rho}_{\rm p})^{1/3}$, if τ_{10} is much smaller than $\tau_{\rm e}$.

Combing equations (3.54) to (3.56) and equations (3.64) to (3.66), the evolution equations for a, $\Omega_{\rm s}$, and ψ in the equilibrium tides plus the inertial wave dissipation can be written as follows:

$$\dot{a} = (\dot{a})_{\rm e}, \tag{3.68}$$

$$\dot{\Omega}_{\rm s} = (\dot{\Omega}_{\rm s})_{\rm e} + (\dot{\Omega}_{\rm s})_{10} - (\dot{\Omega}_{\rm s})_{10,{\rm e}}, \tag{3.69}$$

$$\dot{\psi} = (\dot{\psi})_{\rm e} + (\dot{\psi})_{10} - (\dot{\psi})_{10,{\rm e}}, \tag{3.70}$$

where

$$\frac{(\dot{\Omega}_{\rm s})_{10,{\rm e}}}{(\dot{\Omega}_{\rm s})_{10}} = \frac{(\dot{\psi})_{10,{\rm e}}}{(\dot{\psi})_{10}} = \left(\frac{Q_{10}}{Q_{\rm e}}\right)\left(\frac{k_2}{k_{10}}\right). \tag{3.71}$$

The model was studied by Rogers & Lin (2013), who numerically integrated a set of simplified equations (3.68) to (3.70). They found that planetary systems with initially arbitrary spin-orbit angles have three stable configurations; aligned, anti-aligned, and polar orbits. A more detailed consideration of the Lai model is presented in chapter 5.

[2]We adopt the definition of τ_{10} by Rogers & Lin (2013), which corresponds to t_{s10} of Lai (2012).

Chapter 4

Coplanar High-eccentricity Migration (CHEM)

4.1 Introduction

As described in section 2.4, Coplanar High-eccentricity Migration (CHEM) is a promising channel to form HJs, in particular, counter-orbiting HJs. In this chapter, we systematically explore the fate of the inner planet in CHEM both analytically and numerically.

The rest of this chapter is organized as follows. In section 4.2, we present our generalization of the extreme eccentricity condition. In section 4.3, we perform the numerical simulations for a giant gas inner planet with a sub-stellar outer perturber including the short-range forces and dissipative tides. In section 4.4, we consider a planetary outer perturber. In this case, we also analytically estimate the migration timescale. In section 4.5, we consider the case with an inner planet of super-Earth mass in CHEM. Section 4.6 presents the formation of close binaries in CHEM. Section 4.3 to 4.6 consider hypothetical systems for the systematic parameter survey. Instead, section 4.7 presents our application to the observed systems that may result from CHEM. Section 4.8 is devoted to summary and discussion of the present chapter. This chapter is based on Xue & Suto (2016) and Xue et al. (2016).

4.2 Analytical Approach to Extreme Eccentricity Condition

4.2.1 Generalization of Extreme Eccentricity Condition

As described in subsection 3.1.2, Petrovich (2015b) presented the extreme eccentricity condition ($e_1 \to 1$) in the planetary limit ($m_1 \ll m_0$, $m_1 \leq m_2$). In this subsection, we generalize the results of Petrovich (2015b) in two aspects. First, we consider the system

in which the inner planet and the outer perturber have comparable masses. In that case, the upper boundary of the extreme eccentricity condition, $\epsilon_{\rm U}$, becomes important, which is not carefully examined in Petrovich (2015b). Second, we take account of the dynamical effect of the inner body on both the central star and the outer perturber.

We repeat the similar analysis as in subsection 3.1.2 following Petrovich (2015b). The potential in the coplanar limit is given by

$$\tilde{\phi} \equiv \frac{\phi}{\phi_0} = \frac{e_1^2 + 2/3}{2(1-e_2^2)^{3/2}} - \frac{5\epsilon}{16}\frac{4+3e_1^2}{(1-e_2)^{3/2}} e_1 \cos\varpi, \tag{4.1}$$

where

$$\epsilon = \frac{m_0 - m_1}{m_0 + m_1}\frac{a_1}{a_2}\frac{e_2}{1-e_2^2}. \tag{4.2}$$

Unlike in the planetary limit as considered in Petrovich (2015b), we retain the term $(m_0 - m_1)/(m_0 + m_1)$ to include the dynamical interaction of m_1 on m_0. Then, the constraints on $\epsilon_{\rm i}$ should be

$$\epsilon_{\rm L} < \epsilon_{\rm i} \equiv \left(\frac{m_0 - m_1}{m_0 + m_1}\right)\frac{a_{1,i}}{a_{2,i}}\frac{e_{2,i}}{1-e_{2,i}^2} < \epsilon_{\rm U}. \tag{4.3}$$

The region of ϵ_i satisfying equation (4.3) is referred to as the extreme eccentricity region.

In the left panel of Figure 4.1, we compare the analytical and numerical results of the extreme eccentricity condition with $m_0 = 1M_\odot$, $m_1 = 1M_{\rm J}$, and $m_2 = 5M_{\rm J}$. The numerical simulation is basically identical to that described in 4.4.1, but for point masses interacting only through the gravity. The black, green, and magenta lines indicate the analytic boundaries derived from equation (4.3), in the planetary limit taken from equation (3.27), and in the test particle limit derived from equation (3.23), respectively. The solid and dashed lines represent $\epsilon_{\rm L}$ and $\epsilon_{\rm U}$. In the simulation runs, we set the maximum simulation time $T_{\rm max} = 10^{10}$ yr ($\sim 10^9$ orbital period) and stop each run before $T_{\rm max}$ if the system encounters the orbital flip. Here we use the orbital flip as the signal for the system reaching extreme eccentricity following Li et al. (2014). The red crosses indicate the flipped runs and the blue crosses are the non-flipped runs. Our simulations homogeneously sample different $e_{1,i}$ and $a_{1,i}$ on ($e_{1,i}$, ϵ_i) plane. We observe that the analytical criterion derived from equation (4.3) and in the planetary limit both are in good agreement with the numerical results, but the extreme eccentricity condition in the test particle limit is not sufficiently accurate; in the test particle limit, the predicted $\epsilon_{\rm L}$ is larger than the corresponding boundary in simulation and $\epsilon_{\rm U}$ does not exist.

As shown in the left panel of Figure 4.1, $\epsilon_{\rm U}$ significantly limits the extreme eccentricity region with $m_1 = 1M_{\rm J}$ and $m_2 = 5M_{\rm J}$. Then we consider the different choice of m_2 with particular emphasis on the importance of $\epsilon_{\rm U}$. The result is shown in the right panel of Figure 4.1 with solid and dashed lines representing $\epsilon_{\rm L}$ and $\epsilon_{\rm U}$. The red, black, and green lines are derived from equation (4.3) and correspond to $m_2 = 1M_{\rm J}$, $5M_{\rm J}$, and $10M_{\rm J}$ with $m_0 = 1M_\odot$ and $m_1 = 1M_{\rm J}$, respectively. The magenta line is the extreme eccentricity

condition in the test particle limit. The difference of the analytical estimate of equation (4.3) against that of equation (3.23) in the test particle limit increases as m_1/m_2 increases as expected. In particular, $\epsilon_{\rm U}$ does not show up in the test particle limit, but affects the extreme eccentricity region when taking account of the effect of m_1 on m_2. This modification becomes more important as m_1/m_2 increases; $\epsilon_{\rm U}$ only affects a small region for $m_2 = 10M_{\rm J}$ ($m_1/m_2 = 0.1$), but significantly shrinks the extreme eccentricity region for $m_2 = 5M_{\rm J}$ ($m_1/m_2 = 0.2$), and $1M_{\rm J}$ ($m_1/m_2 = 1.0$). This implies that $\epsilon_{\rm U}$ can be safely neglected when $m_1 \ll m_2$, but should be carefully considered when m_1 becomes not negligible compared to m_2 ($m_1/m_2 > 0.1$). When the inner plant reaches the extreme eccentricity, the back reaction on e_2 increases with both m_1/m_2 and a_1 due to the orbital angular momentum conservation. Thus, both $\epsilon_{\rm L}$ and $\epsilon_{\rm U}$ shift towards smaller a_1 regions as m_1/m_2 increases.

Next, we consider the dependence of the extreme eccentricity condition derived from equation (4.3) on m_1/m_0, which is illustrated in Figure 4.2. We present four different cases with $m_1/m_0 = 0.001$, 0.1, 0.3, and 0.9, so as to basically cover the range of a gas giant, sub-stellar object, M-dwarf and sun-like star with a sun-like central star, respectively. The lower and upper boundaries of ϵ are indicated by the solid and dashed lines. The red and blue lines correspond to $m_1/m_2 = 0.2$ and 0.5, respectively. The green lines present the boundaries in the planetary limit. In the left upper panel with $m_1/m_0 = 0.001$, the resulting extreme eccentricity region derived from equation (4.3) and from equation (3.27) in the planetary limit are almost identical. As m_1/m_0 increases, the planetary limit becomes less accurate. As shown in the other three panels, for $m_1/m_0 \geq 0.1$, the extreme eccentricity region tends to be significantly narrower and shifted towards higher $e_{1,i}$ regime. Since the relative importance of the octupole term is proportional to $(m_0 - m_1)/(m_0 + m_1)$, increasing of m_1/m_0 corresponds to decreasing of the octupole effect. Therefore, in order to reach the extreme eccentricity, the inner orbit requires a higher $e_{1,i}$ to compensate the relatively smaller octupole term.

In summary, $\epsilon_{\rm U}$ limits the extreme eccentricity region when m_1 becomes comparable with m_2. In section 4.4, we consider the systems with a giant gas inner planets and a planetary outer perturber, where the effect of $\epsilon_{\rm U}$ should be carefully considered. The planetary limit is a reasonably good approximation for $m_1 \ll m_0$, but is not sufficiently accurate when $m_1/m_0 \geq 0.1$. Indeed, increasing m_1/m_0 and m_1/m_2 both shrink the extreme eccentricity region. Therefore, it is very difficult to form close-in orbit in CHEM for system with a relatively massive inner body, for example, triple star system.

4.2.2 SRFs Effect

So far, we have presented the extreme eccentricity condition neglecting the short-range forces (SRFs). In reality, general relativity (GR), stellar and planetary non-dissipative tides, and stellar and planetary rotational distortion should be included as the SRFs. Indeed, those SRFs may significantly affect the dynamical evolution of the inner planet as described in subsection 2.4.2. Adopting the methodology similar to Petrovich (2015b),

we analytically consider the SRFs effect including GR, planetary non-dissipative tides and planetary rotational distortion[1]. In this case, the total dimensionless potential is given by

$$\tilde{\phi}_{\rm total} = \tilde{\phi} + \tilde{\phi}_{\rm GR} + \tilde{\phi}_{\rm TD} + \tilde{\phi}_{\rm PRD}. \tag{4.4}$$

In equation (4.4), $\tilde{\phi}_{\rm GR}$, $\tilde{\phi}_{\rm TD}$, and $\tilde{\phi}_{\rm PRD}$ refer to the dimensionless potential due to GR, planetary non-dissipative tides, and planetary rotational distortion:

$$\tilde{\phi}_{\rm GR} = \frac{4Gm_0^2a_2^3}{c^2a_1^4m_2}\frac{1}{(1-e_1^2)^{1/2}}, \tag{4.5}$$

$$\tilde{\phi}_{\rm TD} = \frac{4k_{2,1}}{3}\left(\frac{m_0^2m_2}{m_1}\right)\left(\frac{a_2^3R_1^5}{a_1^8}\right)\frac{1+3e_1^2+3e_1^4/8}{(1-e_1^2)^{9/2}}, \tag{4.6}$$

$$\tilde{\phi}_{\rm PRD} = \frac{2k_{2,1}}{9G}\left(\frac{m_0}{m_1m_2}\right)\left(\frac{a_2^3R_1^5}{a_1^5}\right)\frac{\Omega_{\rm p}^2}{(1-e_1^2)^{3/2}}, \tag{4.7}$$

where c is the speed of light, $k_{2,1}$ is the second Love number of the inner planet, R_1 is the radius of the inner planet, and $\Omega_{\rm p}$ is the spin rate of the inner planet. The potential energy we consider differs from Petrovich (2015b) by including the effect of planetary rotational distortion, equation (4.7). Although $\tilde{\phi}_{\rm PRD}$ turns out to make a minor contribution (see Figure 4.5 for reference), we include it for completeness.

Then, we repeat the similar analysis as in subsection 3.1.2 including those three SRFs. The eccentricity of the inner planet, e_1, cannot reach exactly unity due to the SRFs effect (equations (4.5) to (4.7)). Instead, the maximum eccentricity of the inner planet, $e_{1,f}$, can be determined by the conservation of the potential as follows,

$$\tilde{\phi}_{\rm total}(e_{1,i}, e_{2,i}, \epsilon_i, \varpi_i = \pi) = \tilde{\phi}_{\rm total}(e_{1,f}, e_{2,f}, \epsilon_f, \varpi_f). \tag{4.8}$$

The corresponding minimum pericenter distance of the inner planet, $q_{1,\rm min}$, can be inferred from $e_{1,f}$ as

$$q_{1,\rm min} = a_1(1-e_{1,f}). \tag{4.9}$$

Here $q_{1,\rm min}$ is related to the fate of the system, since tides are very sensitive to the pericenter distance. In order to produce HJ, the inner planet must reach a sufficiently small pericenter distance, such that tidal dissipation can reduce the planet's semi-major axis within a few Gyrs, and its pericenter distance should be larger than the Roche limit to avoid disruption.

We compute the lower and upper boundaries of ϵ_i that correspond to a given value of $q_{1,\rm min}$ as follows. We substitute the value of $e_{1,f}$ corresponding to $q_{1,\rm min}$ into equation (4.8). Combining with the orbital angular momentum conservation, we obtain $\epsilon_{\rm L}$ for $\varpi_f = 0$, and $\epsilon_{\rm U}$ for $\varpi_f = \pi$ by solving equation (4.8) for ϵ_i. The example of $\epsilon_{\rm L}$ and $\epsilon_{\rm U}$ for $q_{1,\rm min}$ are plotted in Figure 4.16 below.

As demonstrated by previous studies, the SRFs effect significantly affects the orbital evolution. Thus, it is necessary to include the SRFs effect to analytically interpret the numerical results. The detailed consideration will be presented in subsection 4.4.2.

[1]We neglect the central stellar tides and rotational distortion, because their effects are indeed negligible in practice.

4.3 Giant Gas Inner Planet with a Sub-stellar Outer Perturber

So far, we have presented the extreme eccentricity condition analytically. In this section, we perform a series of numerical simulations to study the orbital evolution of hierarchical triple systems in CHEM with a giant gas inner planet and a sub-stellar outer perturber. The equations of motions that we adopt are fully described in chapter 3, in which SRFs, GR, spin rotation and tidal effects for both star and inner planet are included in addition to the octupole term of the orbit-average gravitational potential of the outer body. The subsection 4.3.1 describes the basic configuration of the hierarchical near-coplanar triple systems that we simulate. The simulation results in fiducial case of sub-stellar perturber are presented and discussed in subsection 4.3.2. The subsection 4.3.3 presents the SRFs effects. The detail parameter dependence is shown in subsection 4.3.4. Finally, the subsection 4.3.5 presents the spin-orbit angle distribution in this scenario.

4.3.1 Initial Setup

We consider the evolution of near-coplanar hierarchical triple systems consisting of a sun-like central star ($m_0 = 1M_\odot$ and $R_0 = 1R_\odot$), a giant gas inner planet ($m_1 = 1M_{\rm J}$ and $R_1 = 1R_{\rm J}$), and a distant outer perturber (m_2). Specifically, we adopt $a_{2,i} = 500$ AU, $m_2 = 0.03M_\odot$, $e_{2,i} = 0.6$, $i_{12,i} = 6°$, the viscous timescale for the inner planet, $t_{\rm v,p} = 0.03$yr, and $f = 2.7$. The choice of those values for the fiducial parameters is admittedly rather arbitrary because it is very difficult to estimate their joint probability for actual near-coplanar hierarchical triples. Therefore we consider a variety of simulation models with fixed m_2, $a_{2,i}$, $e_{2,i}$, $i_{12,i}$, $t_{\rm v,p}$, and f as listed in Table 5.1, instead of sampling those parameters from their assumed distribution function. Therefore our purpose is not to produce a mock distribution of real near-coplanar hierarchical triples, but to understand the parameter dependence of their dynamical evolution in a systematic fashion.

In each model, we perform ~ 1800 different runs by varying $(e_{1,i}, \epsilon_i)$ systematically; $e_{1,i}$ is varied between 0.6 and 0.96 with a constant interval of 0.02, and ϵ_i is varied between $\epsilon_{\rm crit,i}$ and 0.15 with a constant interval of 0.001. Thus the value of $a_{1,i}$ in each run is uniquely computed from ϵ_i through equation (4.3). The upper limit of 0.15 guarantees the validity of the secular approximation. We note that in all the models, both a_2 and e_2 are practically constant, i.e., $a_2 = a_{2,i}$, and $e_2 = e_{2,i}$, although a_1 and e_1 significantly change from their initial values in most cases.

We fix the initial spin periods of the central star and inner planet as 25 day and 10 day, the viscous timescale of the star $t_{\rm v,s}$ as 50 yr, and the Love numbers for the star and inner planet as 0.028 and 0.5, respectively. The dimensionless principal moment of inertia $I/(MR^2)$ of the star and inner planet are set to 0.08 and 0.26, respectively. We do not randomly choose the initial phase angles so that $\epsilon_{\rm crit,i}$ is independent of them in our parameter survey; we adopt $\omega_{1,i} = 0$, $\omega_{2,i} = 0$, $l_{1,i} = \pi$, and $l_{2,i} = 0$. Since planets are generally expected to form within a proto-planetary disk that is perpendicular to the

spin angular vector of the central star, the initial stellar inclination with respect to the orbit of the inner planet is set to $\psi_i = 0$.

In the simulation, we track the evolution of the planetary systems with the Embedded Runge-Kutta method described in Appendix I by the inner and outer orbital angular momentum vectors, $\mathbf{G}_1$ and $\mathbf{G}_2$, the inner and outer Lenz vectors, $\mathbf{e}_1$, $\mathbf{e}_2$, and the central stellar and inner planetary spin angular momentum vectors, $\mathbf{L}_1$, $\mathbf{L}_2$. The equations for the pure orbital gravity are equations (3.15) to (3.18), for short-range forces are equations (3.29), (3.31), (3.36)-(3.39), (3.42), for tides are equations (3.45)-(3.47).

We perform each simulation up to the maximum simulation time, $T_{\rm max} = 10^{10}$ yr. Even before $T_{\rm max}$, we stop the simulation when the inner planet satisfies both $a_{1,f} < 0.1$ AU and $e_{1,f} < 0.01$, which we regard to be a HJ. We also stop the simulation when the pericenter distance of the inner planet, $q_1 = a_1(1-e_1)$, reaches less than the Roche limit. The time at which the simulation is stopped is referred to as the stopping time, $T_{\rm s}$. Following Petrovich (2015a), the outcomes of our simulations are divided into four categories as follows:

(i) PHJ (prograde HJ) : $a_{1,f} < 0.1$ AU, $e_{1,f} < 0.01$ and $i_{12,f} < \pi/2$.

(ii) RHJ (retrograde HJ) : $a_{1,f} < 0.1$ AU, $e_{1,f} < 0.01$ and $i_{12,f} > \pi/2$.

(iii) TD (tidally disrupted within the Roche limit of the central star) : The inner planet is tidally disrupted if its pericenter distance $q_1 \equiv a_1(1-e_1)$ is less than the Roche limit:

$$q_1 < R_{\rm roche} \equiv f R_1 (m_0/m_1)^{1/3} = 0.0126 \left(\frac{f}{2.7}\right) {\rm AU} \sim 2.71 \left(\frac{f}{2.7}\right) R_\odot. \quad (4.10)$$

The appropriate value for the Roche limit is somewhat uncertain. Thus while our fiducial value of f is 2.7 (e.g, Guillochon et al. 2011), we consider $f = 2.16$ (Faber et al. 2005) and $f = 1.66$ (Naoz et al. 2012) as well. Note, however, that $f \approx 1$ corresponds to the radius of the central star itself, and the planet infalls to the star for $f < 1$.

(iv) NM (non-migrating planet) If the inner planet does not experience a significant migration, and stays at an orbit with $a_{1,f} \sim a_{1,i}$ until $T_{\rm max} = 10^{10}$yr.

In near-coplanar hierarchical triple systems as considered here, all the survived PHJs and RHJs turn out to be very well aligned ($i_{12} < 10^\circ$) and counter-orbiting HJs ($i_{12} \sim \pi$), respectively.

Table 5.1 summarizes the model parameters of our simulations as well as the fraction of their final states. We should emphasize that the fraction of the final states listed in Table 5.1 is computed assuming the uniform distribution over the surveyed region of $(e_{1,i}, \epsilon_i)$ plane. In reality, it is unlikely that $e_{1,i}$ and ϵ_i (or equivalently $a_{1,i}$) are distributed uniformly. Nevertheless this is inevitable because we do not assume any model-dependent

model	a_2(AU)	e_2	$m_2(M_\odot)$	i_{12}	$t_{\rm v,p}$(yr)	f	PHJ	RHJ	NM	TD
fiducial	500	0.6	0.03	6°	0.03	2.7	9.0%	0.4%	1.8%	88.7%
m001	500	0.6	0.01	6°	0.03	2.7	21.0%	2.6%	3.1%	73.2%
m010	500	0.6	0.1	6°	0.03	2.7	4.6%	0.1%	1.1%	94.2%
m100	500	0.6	1	6°	0.03	2.7	1.3%	0.0%	0.2%	98.5%
a200	200	0.6	0.03	6°	0.03	2.7	8.4%	0.0%	1.8%	89.8%
a100	100	0.6	0.03	6°	0.03	2.7	7.7%	0.0%	1.1%	91.2%
a050	50	0.6	0.03	6°	0.03	2.7	10.6%	0.0%	0.0%	89.4%
e03	500	0.3	0.03	6°	0.03	2.7	2.1%	0.2%	1.4%	96.4%
e04	500	0.4	0.03	6°	0.03	2.7	3.7%	0.2%	0.7%	95.4%
e05	500	0.5	0.03	6°	0.03	2.7	6.0%	0.4%	1.3%	92.3%
e07	500	0.7	0.03	6°	0.03	2.7	13.5%	0.5%	3.1%	82.9%
e08	500	0.8	0.03	6°	0.03	2.7	21.0%	0.6%	0.6%	72.9%
i30	500	0.6	0.03	30°	0.03	2.7	2.9%	0.4%	1.0%	95.7%
i15	500	0.6	0.03	15°	0.03	2.7	4.6%	0.7%	1.5%	93.1%
i00	500	0.6	0.03	0°	0.03	2.7	13.4%	0.0%	0.7%	85.9%
t03000	500	0.6	0.03	6°	0.3	2.7	3.4%	0.0%	2.2%	94.4%
t00030	500	0.6	0.03	6°	0.003	2.7	55.3%	25.3%	1.8%	17.6%
t00003	500	0.6	0.03	6°	0.0003	2.7	63.1%	35.0%	1.8%	0.1%
f216	500	0.6	0.03	6°	0.03	2.16	53.5%	32.5%	1.8%	11.9%
f166	500	0.6	0.03	6°	0.03	1.66	60.6%	37.6%	1.8%	0.0%
f000	500	0.6	0.03	6°	0.03	0.0	60.6%	37.6%	1.8%	0.0%

Table 4.1: Summary of parameters and fates of our simulation runs. All the models adopt $m_0 = 1M_\odot$, $R_0 = 1R_\odot$, $m_1 = 1M_{\rm J}$, $R_1 = 1R_{\rm J}$, $\omega_{1,i} = 0$, $\omega_{2,i} = 0$, $l_{1,i} = \pi$, $l_{2,i} = 0$, and $\psi_i = 0$. The final states are divided into four categories: Prograde HJ (PHJ; $a < 0.1$ AU, $e < 0.01$, and $i_{12} < \pi/2$), Retrograde HJ (RHJ; $a < 0.1$ AU, $e < 0.01$, and $i_{12} > \pi/2$), Non-migrating planets (NM) and Tidally disrupted planets (TD; $q < R_{\rm roche}$). We performed 1800 runs over the grids of ($e_{1,i}$, ϵ_i) plane for each model.

and very uncertain prior distribution function for $e_{1,i}$ and ϵ_i in this chapter. Therefore the values of *fraction* referred to throughout the present chapter needs to be interpreted with caution, but still provide an important measure of the fate of the systems.

4.3.2 Fiducial Case

Figure 4.3 plots the final states of the inner planet in our fiducial model for coplanar hierarchical triple systems. In this particular example, we first explore the range of $0.005 < \epsilon_i < 0.15$ to ensure the validity of the analytical extreme eccentricity conditions (equation (3.23) by Li et al. (2014) and equation (3.27) by Petrovich (2015b)). Figure 4.3 clearly shows that the region below those extreme eccentricity conditions agree with that of non-migrating planets in our runs. So their conditions are accurate in distinguishing

the significant migration and non-migration boundary, even if they do not necessarily lead to RHJs; see discussion below. Its most important conclusion is that retrograde HJs are very difficult to form, despite the fact that the plotted region of $(e_{1,i}, \epsilon_i)$ is chosen so as to satisfy the extreme eccentricity condition (3.23) in the test particle limit; $\sim 90\%$ of the systems are tidally disrupted, and $\sim 10\%$ survive as prograde HJs. The fraction of retrograde HJs turn out to be less than 1%. Since this may be a rather unexpected result, we plot the dynamical evolution of typical systems for $e_{1,i} = 0.9$ in six panels of Figure 4.4. While we adopt 10 days as the spin rotation period of the inner planet throughout the current analysis, it may be more relevant to use 10 hours as in the case of Jupiter. In reality, however, the result turns out to be fairly insensitive to the value as shown in subsection 4.3.6 below.

The lower limit of the analytical extreme eccentricity condition (3.23) by Li et al. (2014), $\epsilon_{\rm crit,i}$ is a very good approximation for the *necessary condition*, but obviously not a sufficient condition because it is derived on the basis of orbital dynamics without SRF effect. Our simulation shows that $\epsilon_{\rm crit,i}$ becomes slightly larger, especially for large $e_{1,i}$ (small $a_{1,i}$). The detail of SRFs effect is described in subsection 4.3.3. One example of the behavior in the region between the $\epsilon_{\rm crit,i}$ we adopted and the real flip boundary including the SRFs effect for $\epsilon_i = 0.025 (a_{1,i} = 13.21{\rm AU})$ is illustrated in Figure 4.4a. The system exhibits an oscillation both in $1-e_1$ and i_{12}, but the resulting pericenter distance q_1 is not small enough for the tidal effect to operate. Thus the semi-major axis a_1 stays constant, and no significant migration occurs for 10^{10} yrs. All the other systems with $\epsilon_i < \epsilon_{\rm crit,i}$, therefore not simulated in the present thesis, show the same behavior.

If ϵ_i is slightly larger than $\epsilon_{\rm L}$, the amplitude of oscillation in $1 - e_1$ becomes larger as plotted in Figure 4.4b for $\epsilon_i = 0.028 (a_{1,i} = 14.81{\rm AU})$. In this case, the maximum eccentricity reaches 0.998, rather than 0.990 in the non-migrating example. This large-amplitude oscillations allow the inner planet reaching a minimum pericenter distance of $a_1(1 - e_1) \sim 0.03$ AU where tidal dissipation efficiently extracts orbital energy, which results in gradual damping of a_1 at each maximum eccentricity (minimum pericenter distance). Thus PHJ systems form via multiple close approaches within a typical timescale of several 10^9 yr. The example of Figure 4.4b results in a HJ at $a \sim 0.065$ AU with $i_{12} \sim 4^\circ$. Indeed this slow coplanar migration is systematically studied by Petrovich (2015b), who proposes this as a potential path to PHJs, and our results are in agreement with his proposal.

As ϵ_i increases further, the octupole potential starts to dominate and drives e_1 very close to unity. At the same time, the orbit flip happens if the dissipative tide is neglected. Along the line of $e_1 = 0.9$, we observe two continuous regions where PHJs form (9.0%) via CHEM. One example in this region is shown in Figure 4.4c for $\epsilon_i = 0.034 (a_{1,i} = 18.01{\rm AU})$. Its suggests that this path to PHJ happens over a much smaller timescale than that of Figure 4.4b; note the different scales of time in each panel. In this case, $1-e_1$ monotonically decreases and becomes close to $\sim 10^{-3}$ where the tidal effect becomes important. Therefore in the middle of increasing i_{12}, the system starts to be circularized and becomes PHJ with $a_{1.f} \sim 0.035$ AU within $< 10^7$ yrs. The mutual orbital inclination oscillates with gradually increasingly the amplitude in the range of $i_{12} \sim 0^\circ - 30^\circ$, and

then damps from $\sim 22^\circ$ to $\sim 9^\circ$ during the circularization stage. Since the eccentricity increases until the end of orbit flip if no SRFs effect are taken into account, such HJs have relatively low i_{12}. In total, the resulting PHJs (PHJ 9.0%) are preferentially located in the low ϵ region. Most of them are formed through CHEM within a very short timescale ($\sim 10^7$ yr), while a few result from secular tidal damping via eccentricity-inclination oscillation.

Beyond that value of ϵ_i, the orbit of the inner planet is indeed flipped, but the fate changes very sensitively due to the subtle competition between the flipped condition and the tidal disruption as illustrated in Figure 4.4d to f. As a result, the system behavior looks chaotic, and there seems no systematic parameter region for the formation of RHJs (see Figure 4.3).

Evolution for the formation of RHJs similar to Figure 4.4d and e happens only in a very narrow parameter range; $\epsilon_i = 0.070 (a_{1,i} = 37.21\mathrm{AU})$ and $\epsilon_i = 0.103 (a_{1,i} = 54.81\mathrm{AU})$, respectively. The former is circularized at the second closest point of $1 - e_1$. The orbit suffers from tidal circularization during an orbit flip process within a timescale of a few 10^7 yr. Since the eccentricity of the inner orbit increases in the orbit flip stage, the system suffers from tidal circularization in the beginning of the orbit flip stage in order not to be tidally disrupted. Thus, this system ends with $i_{12,f} = 162^\circ$, only slightly smaller than the highest i_{12} ever reached, 177°. While the latter is circularized at the first closest point due to the stronger perturbation of the outer body. The tidal circularization starts when the orbit flip process is completed. Since the tidal circularization does not modify i_{12} significantly, $i_{12,f}$ remains almost unchanged in the counter-orbiting regime, 172° with $\pm 1^\circ$ oscillation. Such a high value of i_{12} suggests that the counter-orbiting HJ can be formed via CHEM, which supports the conclusion of Li et al. (2014).

Figure 4.4f presents an example of a tidally disrupted inner planet for $\epsilon_i = 0.113 (a_{1,i} = 60.10\mathrm{AU})$. Its pericenter falls into the Roche limit at the second extreme eccentricity approach when $1 - e_1$ reaches $\sim 2 \times 10^{-4}$. Such a state is preferentially found in systems in which the inner planet has a relatively large semi-major axis, since the gravitationally interaction between two orbits are stronger when the inner orbit reaches the extreme eccentricity. The comparison among the panels d, e and f as well as Figure 4.3 strongly indicates that the fate of the systems is very sensitive to the parameters. Nevertheless the conclusion that most of the systems satisfying the extreme eccentricity condition (3.23) are tidally disrupted, instead of forming counter-orbiting HJs, is quite general.

Since most of systems become disrupted via the orbital flip in our simulation, the condition of forming retrograde or counter-orbiting HJs is fairly fine-tuned. Considering the two successful examples of RHJs as shown above, a subtle change of initial condition may singnificantly modify the evolution and tidally disrupt the system as shown in Figure 4.3. So we may need to fine-tune the parameter sets in order to successfully make RHJs, which seems to be unlikely. Based on the low ratio (RHJ 0.4%) and such an uncertainty, it is difficult to form retrograde or counter-orbiting HJs via CHEM.

4.3.3 SRFs Effect

Liu et al. (2015) showed that the pericenter precessions due to SRFs effect suppress the growth of eccentricity of the inner planet, and reduce the flip region of i_{12} for systems under the Lidov-Kozai oscillation. In this subsection, we show that the similar suppression works also for the near-coplanar triple systems.

A small area around the bottom-right region of Figure 4.3 corresponds to non-migrating planets despite the fact that they satisfy the flip criterion equation (3.23) initially. Indeed this comes from the SRFs effect. In order to see their effects separately, we consider the NM (non-migrating) planet example of Figure 4.4a ($\epsilon_i = 0.025(a_{1,i} = 13.21\mathrm{AU}), e_{1,i} = 0.9$).

The left and right panels of Figure 4.5 plot the evolution of the mutual orbital inclination, i_{12}, and the pericenter distance of the inner planet in units of its initial semi-major axis. Since this example corresponds to the NM case, the latter is almost equivalent to $1 - e_1$. We show the results for the secular orbital perturbation effect alone, orbital and general relativistic (GR) correction, orbital and planetary rotational distortion (PRD), orbital and planetary tide (PT)[2], and orbital and all the SRFs effect, from top to bottom.

As expected, the case without the short-ranges forces (top panels) flips the orbital inclination each time $1 - e_1$ becomes less than $\sim 10^{-3}$. The flip repeats periodically since no other dissipational effects are included. If only the PRD is included, the system still shows the orbital flip, but the maximum value of e_1 is slightly suppressed relative to the purely orbital case.

The precession due to PT could effectively limit the orbital flip with maximum eccentricity less than 0.999. On the other hand, the effect of GR is very effective in suppressing the eccentricity; the maximum value of e_1 under the GR correction barely reaches ~ 0.99. Thus the system stays outside the tidal circularization region for 10^{10} yr, and the PT never becomes important in reality, as shown in the bottom panels of Figure 4.5.

The above behavior can be understood by comparing the precession timescales of the Lenz vector $\hat{\mathbf{e}}_1$ for those SRFs, which we plot in Figure 4.6 on the basis of the expressions in section 3.2. Clearly the GR plays a dominant role for $e_1 < 0.995$, while PT becomes dominant for $e_1 > 0.995$; PRD is sub-dominant in either case. This is in good agreement with our simulation result shown in Figure 4.5, and therefore the precession induced by the SRFs, in particular GR, prevents the orbital flip. Since the SRFs become stronger for the smaller semi-major axis, the NM planets are located around the high-$e_{1,i}$ and low-ϵ_i region.

[2]we include the central stellar tide and rotational distortion as well in our simulation, but their effects are indeed negligible.

4.3.4 Dependence on the Model Parameters

The previous section has presented the result for our fiducial model, and discussed the dynamical behavior for several examples. Next we consider the dependence of parameters employed in the fiducial model, separately in each subsection below. The full list of different models is summarized in Table 5.1, and we plot the two models in each subsection as examples. Since we already confirmed that planets with $\epsilon_i < \epsilon_{\rm crit}$ do not migrate in practice, we run the models for $\epsilon_{\rm crit} < \epsilon_i < 0.15$ in what follows.

Mass of the Outer Perturber

We adopt $m_2 = 0.03 M_\odot$ as our fiducial value, but one might wonder if the larger mass would be more relevant as (sub-)stellar perturbers. While this sounds reasonable, the larger m_2 significantly increases the tidal disruption ratio, and there is no chance to form retrograde planets in practice.

This is clearly shown in the left and right panels of Figure 4.7 for $m_2 = 1 M_\odot$ and $0.1 M_\odot$, respectively. Since we focus on the parameter space satisfying the analytic flip condition (3.23), the gravitational perturbation due to the outer body is sufficiently strong to produce the orbital flip potentially. Under such circumstances, the larger m_2 results in the larger e_1 (extremely closer to unity) in which leads to the stronger tidal effect. Therefore in order to survive the tidal disruption, the inner planet should have the smaller $a_{1,i}$ for the larger m_2. This is why the fractions of both PHJs and RHJs decreases as m_2 increases.

Thus it is very difficult to form RHJs via the near-coplanar flip mechanism if the outer perturber has a stellar mass $m_2 > 0.1 M_\odot$. This is why we adopt $m_2 = 0.03 M_\odot$ as our fiducial value.

Semi-major Axis of the Outer Perturber

Consider next the dependence on a_2. Again the proper choice of this parameter is not easy. If a_2 is larger, the near-coplanar configuration is unlikely. On the other hand, the sub-stellar perturber closer to the central star may be difficult to form either. As a compromise, we select $a_2 = 500$, 200, 100 and 50 AU in Table 5.1 with $a_2 = 500$ AU being the fiducial value. Figure 4.8 presents the results for $a_2 = 200$ AU and 50 AU. There are two important messages from Figure 4.8.

First, RHJs do not form for $a_2 \leq 200$ AU. In order to become a RHJ, the inner planet needs to experience the orbital flip before the tidal circularization. This prefers larger $a_{1,i}$ because the inner planet suffers from less tidal dissipation before reaching the extreme eccentricity for the orbital flip. Even larger $a_{1,i}$, however, results in stronger gravitational perturbation from the outer body, and thus the inner planet is tidally disrupted. Due to that subtle competition, RHJs in our fiducial model are confined in the narrow region of $0.07 < \epsilon_i < 0.11$. As a_2 decreases, the entire system becomes more compact for the

same value of ϵ_i. Thus the stronger gravitational perturbation of the outer body brings the inner planet to the orbit within the Roche limit more easily because the pericenter distance at the same maximum eccentricity is smaller. This is why RHJs disappear for the smaller a_2 models. For the same reason, PHJs are limited for the lower ϵ_i region.

Second, NM planet fraction drops as a_2 decreases; 1.8%, 1.8%, 1.1%, and 0.0% for a_2 = 500, 200, 100, and 50 AU, respectively. In the fiducial model, SRFs suppress the the maximum eccentricity and the inner planet does not flip nor is tidally circularized around the high-$e_{1,i}$ and very low-ϵ_i region. The same value of e_i, however, corresponds to the smaller a_1 for the smaller a_2 models. Thus the pericenter distance for those systems becomes smaller, which enhances the tidal dissipation and thus circularizes the orbit. As a result, systems gradually migrate and finally become PHJs via the secular eccentricity-inclination oscillation as illustrated in Figure 4.4b. In any case, the formation of RHJs is more difficult for the smaller a_2 than the fiducial model.

Eccentricity of the Outer Perturber

Sub-stellar perturbers may exhibit a broad range of eccentricity, and we run six simulation sets with $e_{2,i}$ = 0.3, 0.4, 0.5, 0.6 (fiducial), 0.7, and 0.8, and two examples out of those models are plotted in Figure 4.9. We find that the fraction of PHJs monotonically increases for the more eccentric outer perturber. PHJs tend to form preferentially in low $a_{1,i}$ where tidal dissipation becomes effective. Since we consider the same range of ϵ_i for all the models, the corresponding value of $a_{1,i}$ for the same ϵ_i becomes smaller as $e_{2,i}$ increases. Thus the dependence of the fraction on e_2 is mainly due to the scaling. While RHJs are very rare, their fraction also increases slightly as e_2, but it would be mainly due to the scaling of $a_{1,i}$ with respect to ϵ_i.

Mutual Orbital Inclination of the Inner and Outer Orbits

The initial orbits of the inner and outer bodies are naturally expected to be inclined to some extent. While our fiducial model adopts $i_{12,i} = 6°$, we examine more inclined cases of $i_{12,i} = 15°$ and 30° as well as an idealized coplanar case ($i_{12,i} = 0°$). The Lidov-Kozai mechanism starts to work for more inclined cases, and we do not consider here because the orbital flip does not happen in those cases as mentioned in Introduction.

The left and right panels of Figure 4.10 present the results for $i_{12} = 0$ and $i_{12} = 15°$. In the exact coplanar case, the net force normal to the orbital plane always vanishes, and the orbits cannot flip. Thus RHJs cannot form, but PHJs can.

As $i_{12,i}$ increases, the fraction of PHJs decreases monotonically, and they are confined around the narrow region with high-$e_{1,i}$ and low ϵ_i. In rare cases, RHJs form in a scatter manner over the on $(e_{1,i}, \epsilon_i)$ plane, probably due to the chaotic nature of the system.

Viscous Time-scale of the Inner Planet

Unfortunately it is well known that the viscous timescale of planets, $t_{\rm v,p}$, (equivalently, the tidal delay time and tidal quality factor) is the most uncertain parameter in the equilibrium tidal theory. The observational data for the Jupiter – Io system put an empirical lower limit on that of Jupiter as $t_{\rm v,J} > 15$ yr. On the other hand, Socrates et al. (2012) stated that $t_{\rm v,p} < 1.5$ yr for an initially highly eccentric planetary orbit with semi-major axis of ~ 5 AU to be circularized into < 0.06 AU within 10 Gyr. They argued that the discrepancy between their upper limit and the empirical lower limit for Jupiter should not be taken seriously given various theoretical uncertainties concerning the tidal dissipation model and diversities of the physical properties of the exoplanets.

For instance, more recent work by Storch & Lai (2014) examined a possibility of tidal dissipation in solid cores of giant planets, and claimed that tidal dissipation in the core can reconcile the Jupiter-Io tidal constraint and very efficient high-eccentricity migration simultaneously.

Given a somewhat confusing situation, we decided to adopt $t_{\rm v,p} = 0.03$ as our fiducial value, simply following Li et al. (2014). Our purpose of the present thesis is not to find a suitable value for $t_{\rm v,p}$ but to understand the role of $t_{\rm v,p}$ in the orbit flip of near-coplanar triple systems. Thus we examine the other three cases with $t_{\rm v,p} = 0.3$, 0.003, and 0.0003 yr as well.

The results are plotted in Figure 4.11. As expected, the fate of the inner planet is very sensitive to the very uncertain value of $t_{\rm v,p}$. When $t_{\rm v,p}$ is smaller, the tide on the planet becomes stronger and the planet suffers from very efficient circularization even at a larger pericenter distance. Thus the majority of the tidally disrupted planets for $t_{\rm v,p} = 0.3$ yr survive as PHJs and RHJs for $t_{\rm v,p} = 0.003$yr. The lower-right region of Figure 4.11 corresponds to planets at a relatively larger pericenter distance, and thus insensitive to the value of $t_{\rm v,p}$.

Of course, the value of $t_{\rm v,p} = 0.003$yr is very extreme and unrealistic; even the paucity of the observed RHJs is inconsistent with the choice. Nevertheless Figure 4.11 clearly illustrates that the uncertainty of the tidal dissipation model is the key to understanding the formation and dynamical evolution of HJs in general.

The Proportional Constant for the Roche Limit

Finally we consider the criterion of the tidal disruption itself. As discussed in subsection 4.3.1, the proportional factor f of the Roche limit in equation (4.10) is not precisely determined. While we adopt $f = 2.7$ following Guillochon et al. (2011) from hydrodynamical simulations, $f = 2.16$ is reported by Faber et al. (2005) and $f = 1.66$ is adopted in simulations by Naoz et al. (2012).

As shown in the previous subsection, the efficiency of the tidal disruption is the most important in determining the fate of the inner planet. Thus we plot the cases of $f = 2.16$ and $f = 1.66$ in the left and right panels of Figure 4.12, respectively.

Similarly to Figure 4.11, SRFs are effective and suppress the growth of the eccentricity of the inner planet in the lower-right region of Figure 4.12. Thus the pericenter distance of the inner planets around the region is larger than $R_{\rm roche}$ in any case, and the fudge factor f hardly changes the evolution of those planets.

On the other hand, tidally disrupted planets in our fiducial model are sensitive to the value of f. As is clear from Figure 4.12, those planets turn out to survive as PHJs and RHJs for the smaller value of f, and there are no tidally disrupted planets for $f = 1.66$. Indeed the result with $f = 1.66$ is already virtually indistinguishable with the case where the tidal disruption happens only when the inner planet falls into the central star.

4.3.5 Spin-orbit Angle Distribution

So far we have classified the survived HJs into prograde or retrograde according to the mutual orbital inclination angle i_{12} of the inner and outer orbits, i.e., $i_{12} < 90^\circ$ or $> 90^\circ$, respectively. In reality, however, i_{12} cannot be measured directly since the possible outer perturbers of the observed HJs are hardly identified. Thus observationally the distinction between prograde and retrograde HJs is made from the the value of λ, the sky-projected angle of ψ, obtained from the Rossiter-McLaughlin effect. Since our current simulation runs solve the evolution of the stellar spin axis as well, we can address the validity of a somewhat conventional assumption of $i_{12} = \psi$. The result is plotted in Figure 4.13, which basically confirms that i_{12} can be used as a proxy for ψ as long as the stellar spin vector is completely aligned with the orbital angular momentum vector of the inner planet initially ($\psi_i = 0$) as we adopted in the present runs.

Now we show the distribution of ψ in Figure 4.14. These plots indicate that PHJs and RHJs in our simulations correspond almost exclusively to well-aligned ($i_{12} < 20^\circ$) and counter-orbiting ($180^\circ - i_{12} < 20^\circ$) planets. This is not the case, however, for models with very strong tidal interaction (t00030 and f216), which exhibit a very broad distribution of i_{12} and thus of ψ.

In CHEM, the planetary orbit suffer from tidal circularization after the orbit flip. Thus the system end up with PHJs if the tidal circularization happens before the orbit flip, and RHJs if the orbit flip occurs before the circularization. On the other hand, the tidally disrupted planets have a very broad distribution of ψ that we define at the epoch when the pericenter distance of the inner planet reaches the Roche limit. The result implies that those planets fall into the Roche limit in a very short timescale less than that of the orbit flip.

4.3.6 Effect of the Spin Rotation Period of the Inner Planet in CHEM

Throughout the analysis in this section, we have adopted $T_{\rm p} = 10$ days as the spin rotation period of the inner planet. If one considers Jupiter as a typical planet, 10 hours, instead

of 10 days, may be more relevant. Therefore we repeat our fiducial run using the 10 hour period while keeping all the other parameters unchanged. Figure 4.15 shows the result, which is basically identical with Figure 4.3. Just for more quantitative comparison, we show the branching ratios of the final outcomes; PHJ 8.5%, RHJ 0.4%, NM 2.1%, and TD 89.0%. Thus we conclude that the final result is very insensitive to the choice of the planetary spin period in this range.

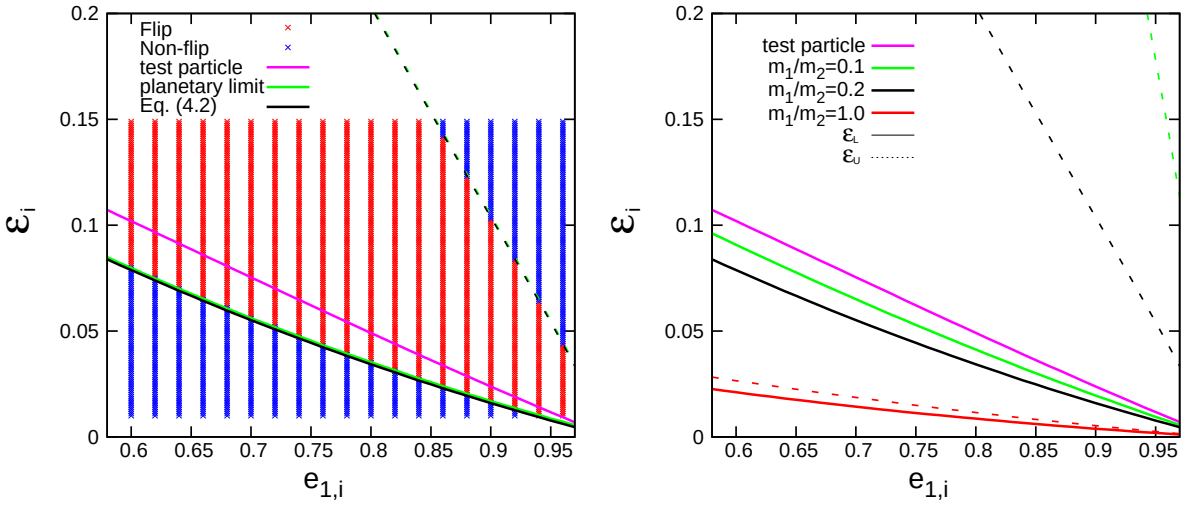

Figure 4.1: Left Panel: Comparison of the numerical results of the orbital evolution and the analytic expressions. The initial condition of the numerical simulation is $m_0 = 1M_\odot$, $m_1 = 1M_\mathrm{J}$, $m_2 = 5M_\mathrm{J}$, $a_2 = 50$ AU, $e_{2,i} = 0.6$, $i_{12,i} = 6°$, $\omega_{1,i} = 0$, $\omega_{2,i} = 0$, $l_{1,i} = \pi$, $l_{2,i} = 0$. The red crosses represent the flipped runs and the blue crosses are the non-flipped runs within $T_\mathrm{max} = 10^{10}$ yrs. The black solid and dashed lines (Eq. (4.3)) indicate the lower and upper boundaries of ϵ from equation (4.3), the green solid and dashed lines (planetary limit) plot the lower and upper boundaries of ϵ_pl in the planetary limit taken from equation (3.27), and the magenta line (test particle limit) is the extreme eccentricity condition in the test particle limit obtained from equation (3.23). Right panel: The extreme eccentricity condition from equation (4.3) for different values of m_2 with $m_0 = 1M_\odot$, $m_1 = 1M_\mathrm{J}$. The red, black, and green lines represent $m_2 = 1M_\mathrm{J}$ ($m_1/m_2 = 1.0$), $5M_\mathrm{J}$ ($m_1/m_2 = 0.2$), and $10M_\mathrm{J}$ ($m_1/m_2 = 0.1$); the solid and dashed lines refer to the lower and upper boundaries, respectively. The magenta line is the extreme eccentricity condition in the test particle limit.

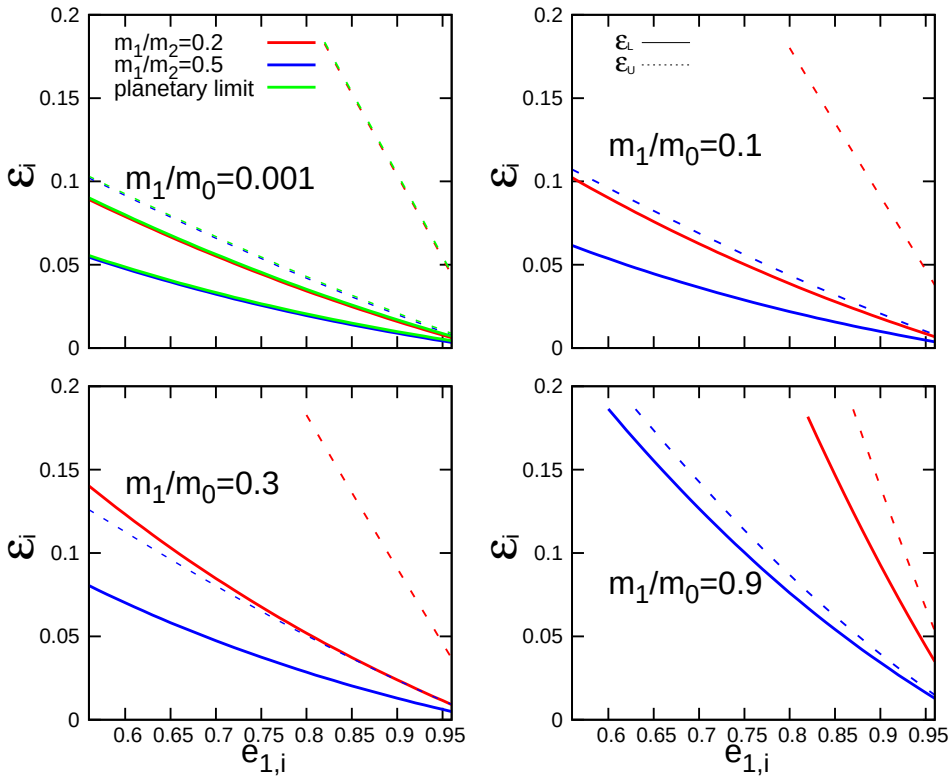

Figure 4.2: Extreme eccentricity condition for the different ratio of m_1/m_0 taken from equation (4.3). Four different cases with $m_1/m_0 = 0.001$, 0.1, 0.3, and 0.9 are presented, from left to right, upper to bottom, respectively. The red and blue lines correspond to $m_1/m_2 = 0.2$, and 0.5; the solid and dashed lines refer to the lower and upper boundaries of ϵ, respectively. The green lines in the left upper panel represent the boundaries of $\epsilon_{\rm pl}$ in the planetary limit.

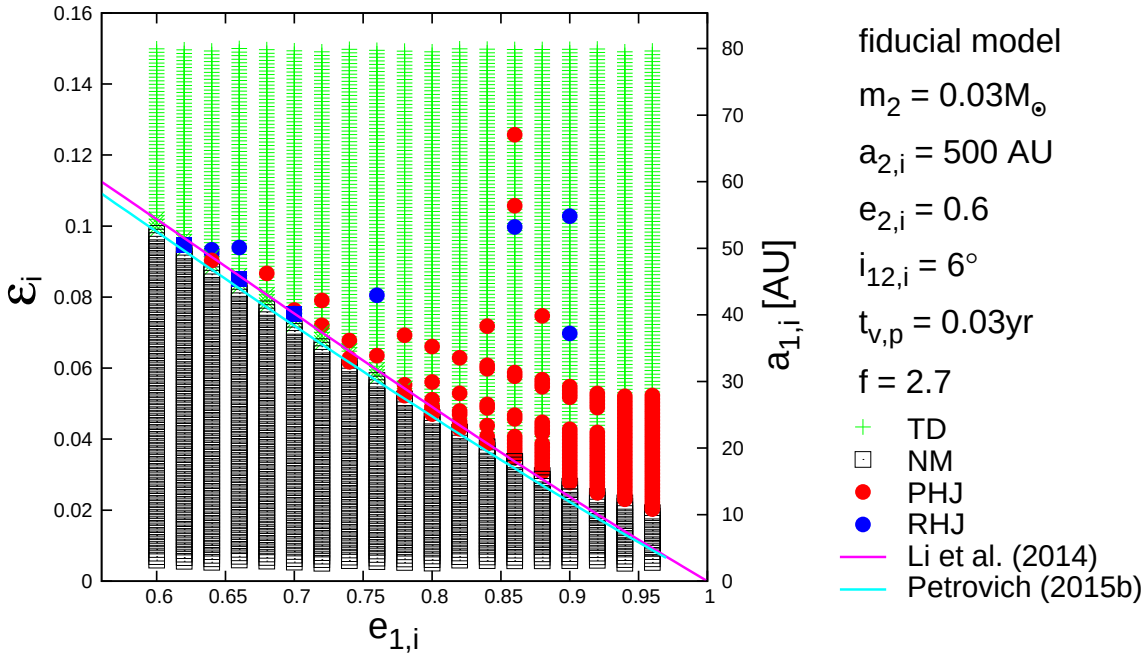

Figure 4.3: Fate of the inner planet on the $(e_{1,i}, \epsilon_{1,i})$ plane for our fiducial model; $a_{2,i} = 500$ AU, $m_2 = 0.03 M_\odot$, $e_{2,i} = 0.6$, $t_{\rm v,p} = 0.03$ yr. The values of $e_{1,i}$ are chosen from 0.6 to 0.96 with a constant interval of 0.02, and ϵ_i, from 0.005 to 0.15 with a constant interval of 0.001. The final states are indicated by green crosses for Disrupted planets (TD), black open squares for Non-migrating planets (NM), red filled circles for Prograde HJs (PHJ), and blue filled circles for Retrograde HJs (RHJ), respectively.

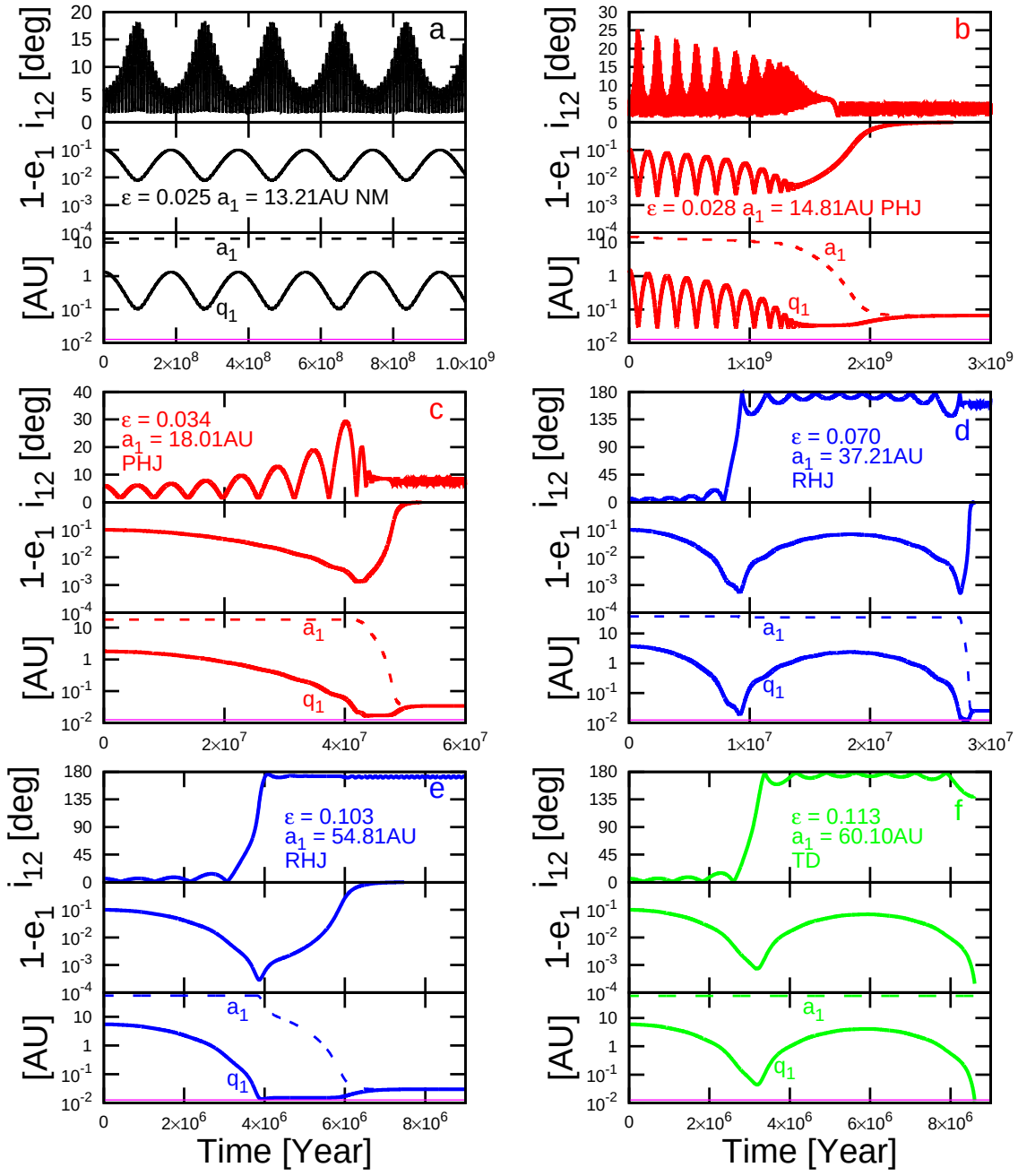

Figure 4.4: Evolution of our fiducial model with $e_{1,i} = 0.9$ for different initial semi-major axis $a_{1,i}$. The final outcomes, Disrupted (TD), Non-migrating (NM), Prograde HJ (PHJ), and Retrograde HJ (RHJ) are shown in green, black, red, and blue line, respectively. For each time evolution, the evolution of i_{12}, e_1, and a_1, q_1 are shown in the top, middle and bottom panel, while a_1 is shown in dashed line, i_{12}, e_1, and q_1 are shown in solid line, and Roche limit is shown in the bottom panel with pink solid line, respectively.

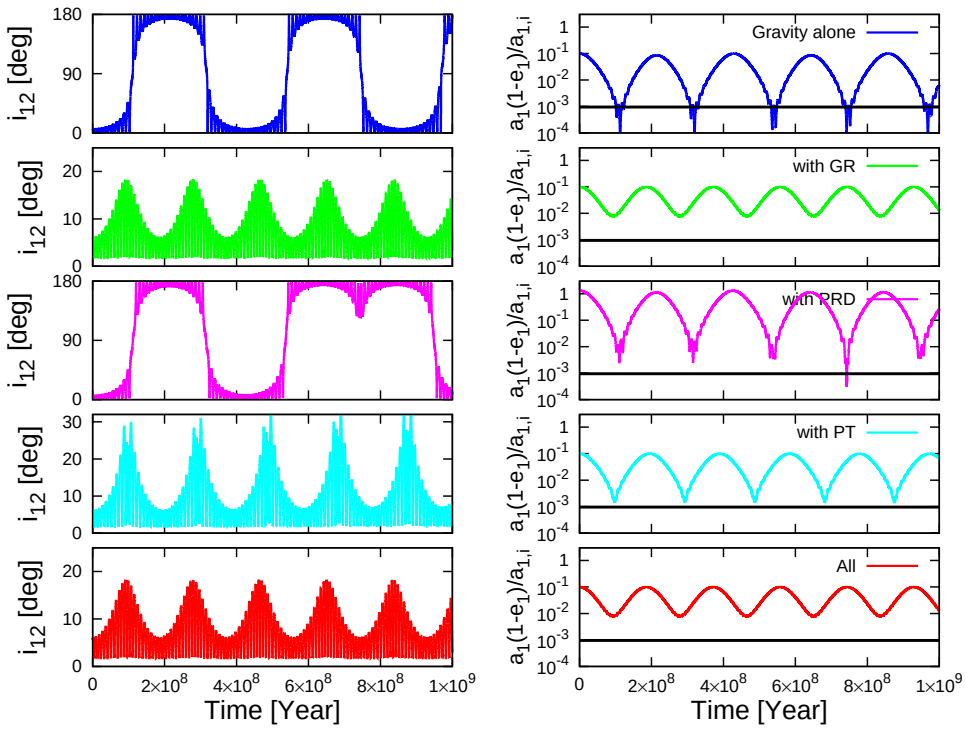

Figure 4.5: An illustrative example indicating the SRFs effect. The initial condition of this example corresponds to that of Figure 4.4a; $a_{1,i} = 13.21$ AU ($\epsilon_i = 0.025$), and $e_{1,i} = 0.9$. Orbital evolution of 10^9 yr with different SRFs effect is plotted separately. From top to bottom, we plot quadrupole and octupole gravitational force alone in blue, gravity plus correction for general relativity (GR) in green, gravity plus planetary rotational distortion (PRD) in magenta, gravity plus tides (PT) in cyan, and finally gravity plus all the three SRFs (All) in red. The black line corresponds to the Roche limit with $f = 2.7$.

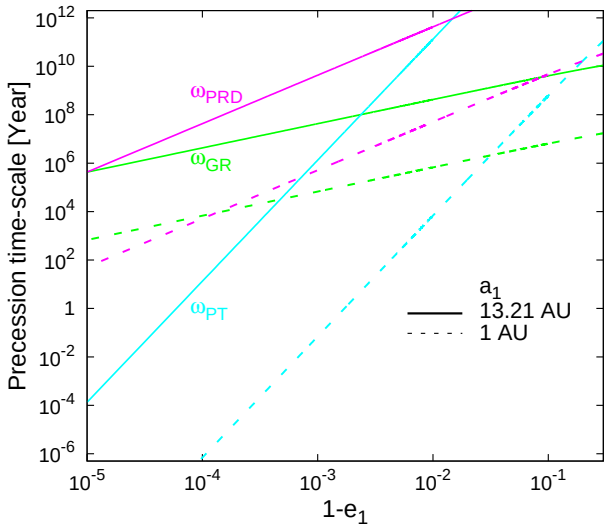

Figure 4.6: Analytical precession timescales for the three SRFs on $\hat{\mathbf{e}}_1$ as a function of $1-e_1$ (instead of $1-e_1^2$). The solid and dashed lines correspond to $a_1 = 13.21$AU (corresponding to Figure 4.5) and $a_1 = 1$AU, respectively. The analytical expressions are explicitly given as equations (4.5) $\sim$ (4.7) in subsection 4.2.2.

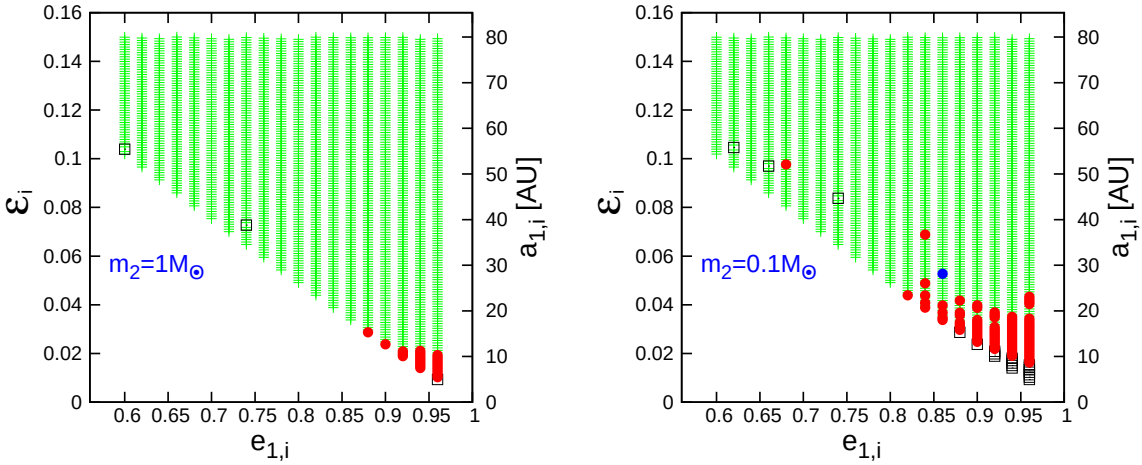

Figure 4.7: Fate of the inner planet on the $(e_{1,i}, \epsilon_i)$ plane of m100 with $m_2 = 1M_\odot$ (left) and m010 with $m_2 = 0.1M_\odot$ (right).

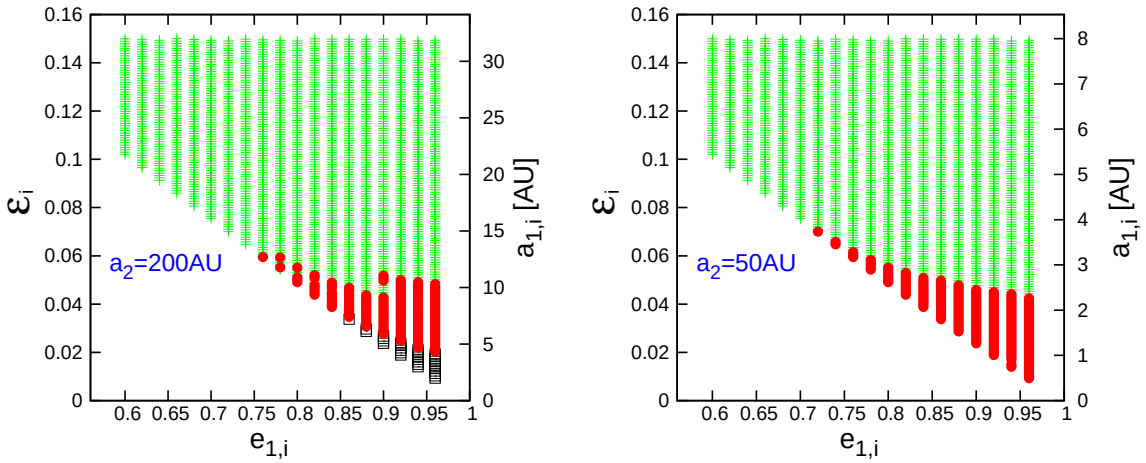

Figure 4.8: Fate of the inner planet on the $(e_{1,i}, \epsilon_i)$ plane of a200 with $a_2 = 200$AU (left) and a050 with $a_2 = 50$AU (right).

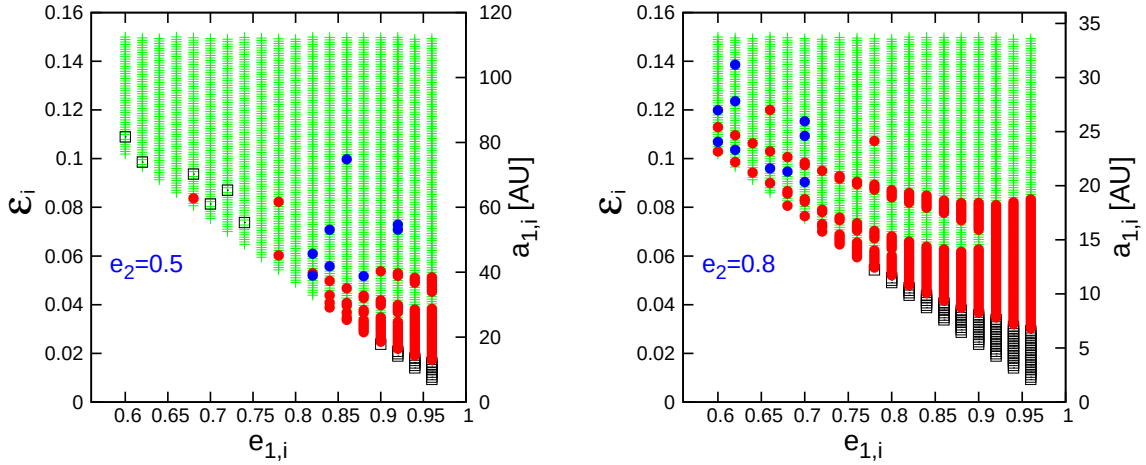

Figure 4.9: Fate of the inner planet on the $(e_{1,i}, \epsilon_i)$ plane of e05 with $e_{2,i} = 0.5$ (left) and e08 with $e_{2,i} = 0.8$ (right).

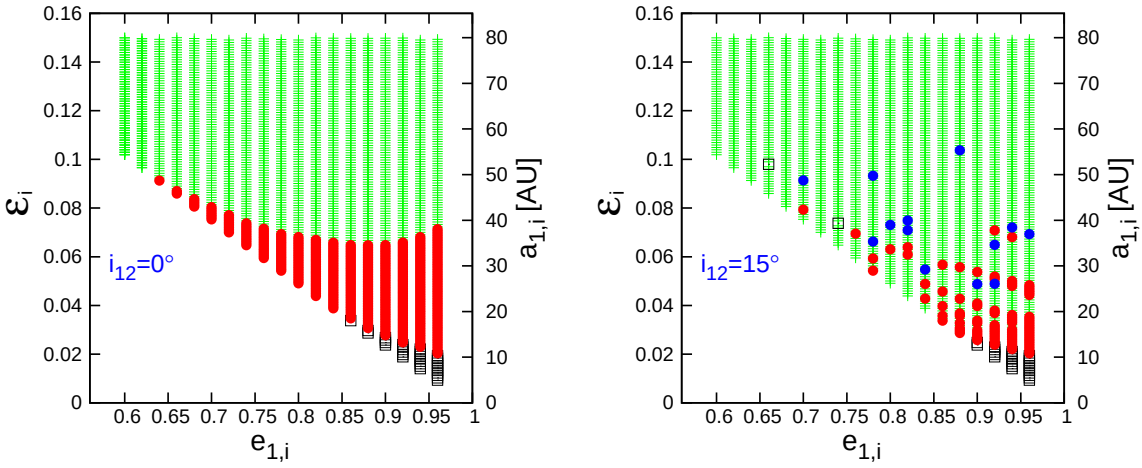

Figure 4.10: Fate of the inner planet on the $(e_{1,i}, \epsilon_i)$ plane of i00 with $i_{12,i} = 0$ (left) and i15 with $i_{12,i} = 15°$ (right).

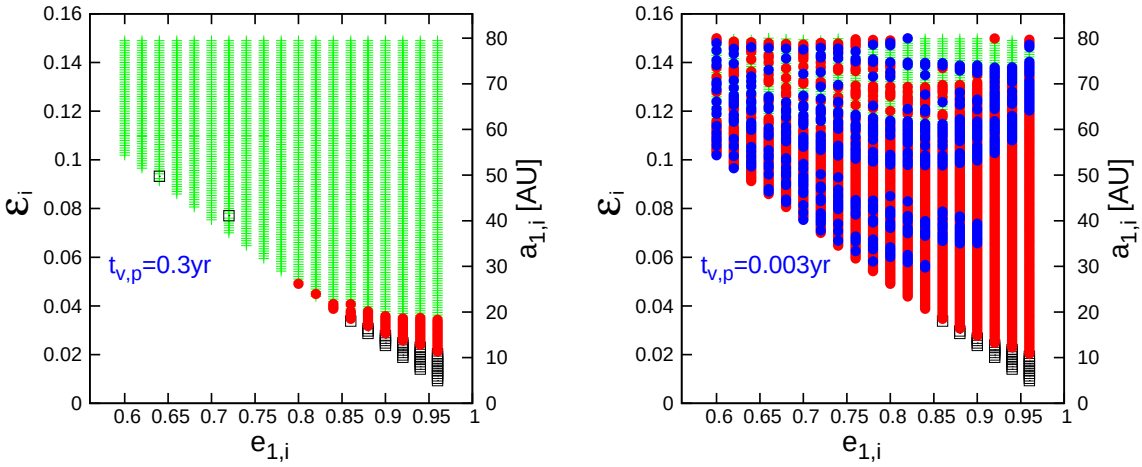

Figure 4.11: Fate of the inner planet on the $(e_{1,i}, \epsilon_i)$ plane of t03000 with $t_{\rm v,p} = 0.3$yr (left) and t00030 with $t_{\rm v,p} = 0.003$yr (right).

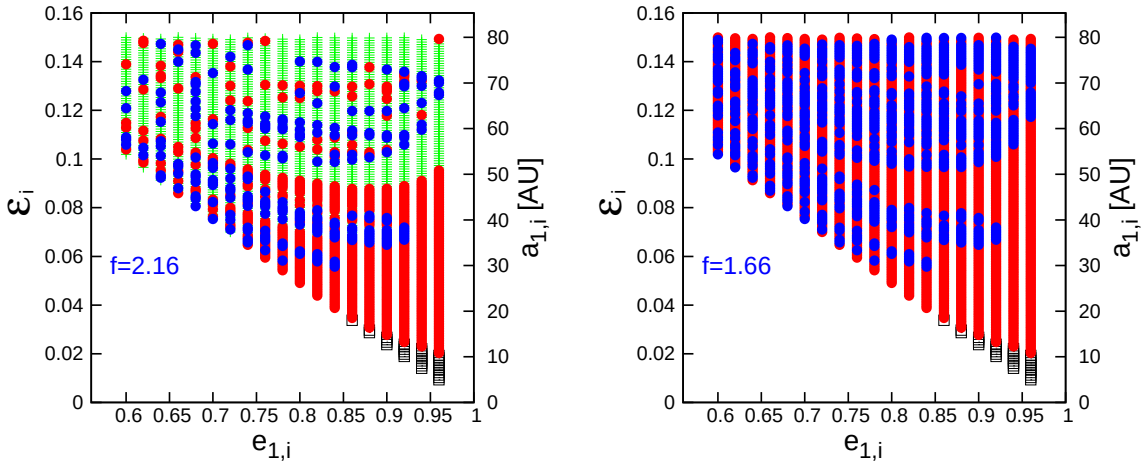

Figure 4.12: Fate of the inner planet on the $(e_{1,i}, \epsilon_i)$ plane of f216 with $f = 2.16$ (left) and f166 with $f = 1.66$ (right).

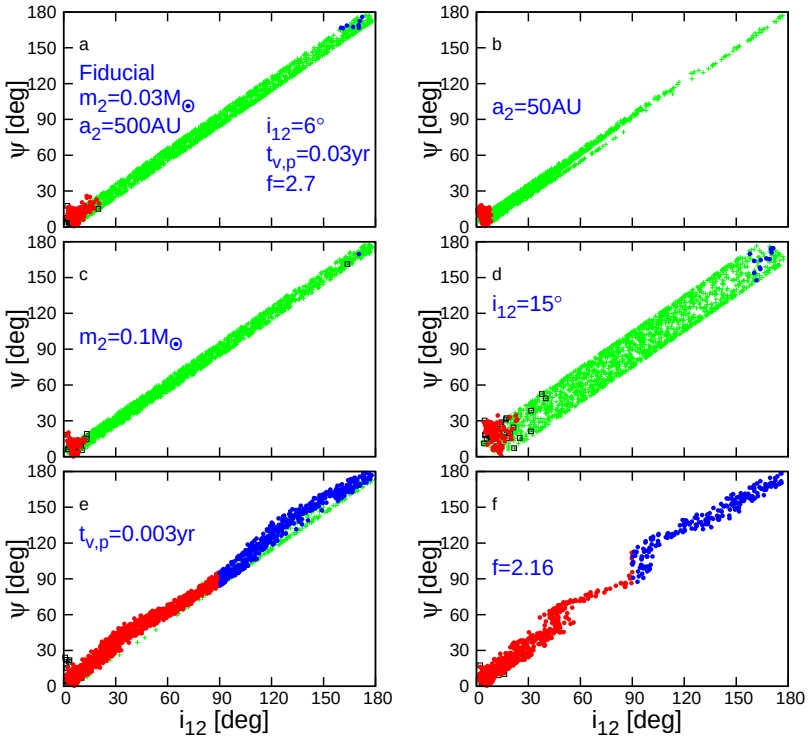

Figure 4.13: Mutual orbital orbital inclination, i_{12} against the spin-orbit angle between the central star and the inner planet, ψ. The different colors correspond to the different final outcomes of the inner planet; PHJ (red), RHJ (blue), NM (black), and TD (green).

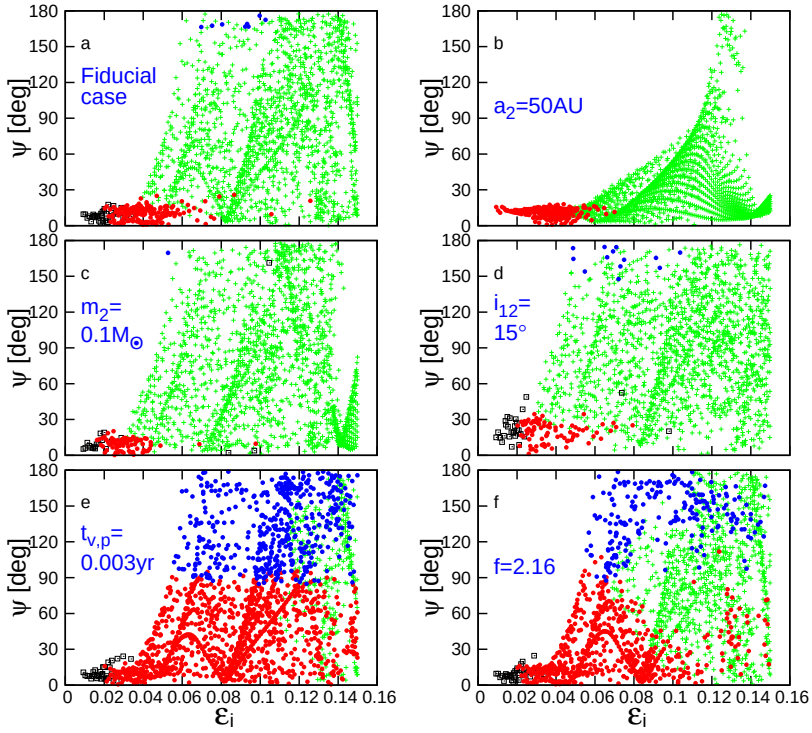

Figure 4.14: Spin-orbit angle between the central star and the inner planet, ψ. for our models; a: fiducial, b: a50, c: m01, d: i15, e: t00030, and f: f216. The different colors correspond to the different final outcomes of the inner planet; PHJ (red), RHJ (blue), NM (black), and TD (green).

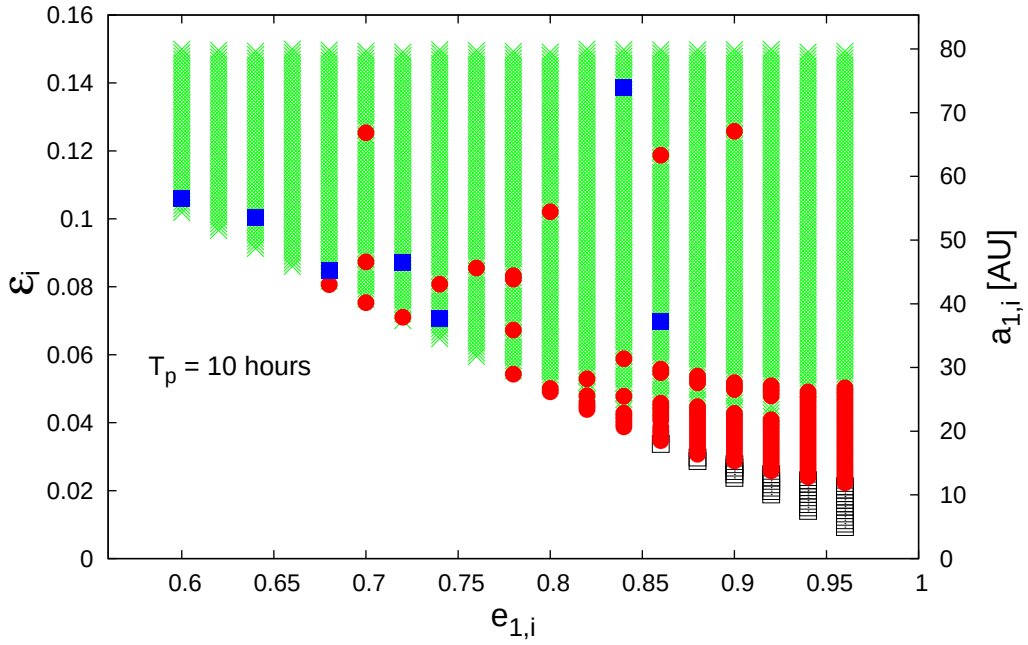

Figure 4.15: Same as Figure 4.3 but with $T_p = 10$ hours as the planetary spin rotation period.

4.4 Giant Gas Inner Planet with a Planetary Outer Perturber

In this section, we consider a planetary object as the outer perturber, and perform a series of numerical simulations to study the orbital evolution of hierarchical triple systems in CHEM similarly as previous section with a sub-stellar outer perturber. We first present the model parameters and our fiducial case in subsection 4.4.1, and then consider how to interpret the numerical results in terms of the analytical argument in subsection 4.4.2. Finally we discuss the parameter dependence and the final distribution of the orbital elements in subsections 4.4.3 and 4.4.4.

4.4.1 Simulation Parameters and Fiducial Results

In previous section, we considered the sub-stellar perturber ($10M_{\rm J} < m_2 < 1M_\odot$), but here we consider the planetary perturber ($1M_{\rm J} < m_2 < 10M_{\rm J}$). In this subsection, we consider $m_2 = 5M_{\rm J}$ and $a_2 = 50$ AU as the fiducial value and discuss the m_2 and a_2 dependence in subsection 4.4.3. In this section, we adopt 0.5 days as the initial spin period for the inner planet based on our Jupiter. Other parameters are identical with the sub-stellar perturber case. The model parameters and fraction of final fates are summarized in Table 4.2. We first discuss the fiducial case and its implications, then move to the parameter dependence and resulting distribution of the orbital elements.

Figure 4.16 shows the numerical results and analytical predictions of our fiducial case of a planetary perturber on $(e_{1,i}, \epsilon_i)$ plane with $a_2 = 50$ AU, $m_2 = 5M_{\rm J}$, $e_{2,i} = 0.6$, $i_{12,i} = 6^\circ$, $t_{\rm v,p} = 0.03$ yr, and $f = 2.7$. In the current simulation, we adopt a tidal model in which $\Delta t_{\rm p}$ ($t_{\rm v,p}$) is constant. In this case, the tidal quality factor, $Q_{\rm p}$, is time-dependent as

$$\begin{aligned} Q_{\rm p} &= \frac{1}{2|\Omega_{\rm p} - n_1|\Delta t} \\ &= \frac{G m_1 t_{\rm v,p}}{6(1+k_{2,1})R_1^3|\Omega_{\rm p} - n_1|} \\ &\approx 3\times10^3 \left(\frac{t_{\rm v,p}}{0.03{\rm yr}}\right)\left(\frac{P_{\rm p}}{0.5{\rm day}}\right)\left(\frac{m_1}{M_{\rm J}}\right)\left(\frac{R_{\rm J}}{R_1}\right)^3, \end{aligned} \tag{4.11}$$

where $P_{\rm p}$ is the period of the inner planet. Because the spin rate of the inner planet, $\Omega_{\rm p}$, soon arrives its equilibrium state, $Q_{\rm p}$ becomes one magnitude larger in a very short timescale. The lower and upper boundaries of ϵ analytically estimated from equation (4.3) are plotted in red dashed lines. Those analytical estimate are different from our numerical results, because the former neglects the SRFs effect. In this figure, we show non-migrating planets (NM), prograde HJs (PHJ), and tidally disrupted planets (TD) in black open squares, red filled circles, and green crosses, respectively.

The most common outcome is tidally disrupted planets (TD; 61.7%). This outcome is preferentially located in the region in which the inner planet has relatively larger ϵ_i

Table 4.2: Summary of parameters and the fates of our simulation runs described in section 4.4.

Model	a_2 au	m_2 $M_{\rm J}$	i_{12}	$t_{\rm v,p}$ yr	f	PHJ	RHJ	NM	TD
fiducial	50	5	6°	0.03	2.7	24.7%	0.0%	13.6%	61.7%
a200	200	5	6°	0.03	2.7	27.5%	0.5%	19.4%	52.7%
m10	50	10	6°	0.03	2.7	19.4%	0.0%	3.9%	76.7%
m07	50	7	6°	0.03	2.7	22.5%	0.0%	4.3%	73.3%
m06	50	6	6°	0.03	2.7	23.8%	0.0%	9.1%	67.1%
m04	50	4	6°	0.03	2.7	29.9%	0.0%	19.0%	51.2%
m03	50	3	6°	0.03	2.7	35.3%	0.0%	40.1%	24.6%
m02	50	2	6°	0.03	2.7	37.0%	0.0%	62.9%	0.1%
m01	50	1	6°	0.03	2.7	5.7%	0.0%	94.2%	0.1%
i30	50	5	30°	0.03	2.7	13.6%	0.0%	11.7%	74.8%
t003	50	5	6°	0.003	2.7	60.1%	0.0%	11.3%	28.6%
f216	50	5	6°	0.03	2.16	86.3%	0.0%	13.6%	0.1%

Note. All the models adopt $m_0 = 1M_\odot$, $r_0 = 1R_\odot$, $m_1 = 1M_{\rm J}$, $r_1 = 1R_{\rm J}$, $\omega_{1,i} = 0°$, $\omega_{2,i} = 0°$, $l_{1,i} = 180°$, $l_{2,i} = 0°$, and $\psi_i = 0°$. The second Love number, k_2, of the central star and inner planet are set to 0.028 and 0.5, respectively. The outcomes are divided into four categories: prograde HJ (PHJ; $a < 0.1$ AU, $e < 0.01$, and $i_{12} < 90°$), retrograde HJ (RHJ; $a < 0.1$ AU, $e < 0.01$, and $i_{12} > 90°$), non-migrating planet (NM; $T_{\rm s} = 10^{10}$ yr) and tidally disrupted planet (TD; $q_1 < R_{\rm roche}$). For each model, we perform ~ 2000 runs by varying ($e_{1,i}$, ϵ_i) systematically.

and therefore $a_{1,i}$, since the stronger gravitational interaction due to the outer perturber produces a more extreme eccentricity.

The second common outcome is prograde HJs (PHJ; 24.7%). PHJs are located in the region between NM and TD. We emphasize that the current simulation produce no RHJ unlike the case with a sub-stellar perturber. First, we note that the strength of tides is determined by the pericenter distance of the inner planet, $q_1 = a_1(1-e_1)$. If a_1 is smaller, e_1 does not have to be so close to the unity for the efficient tidal circularization. On the other hand, the orbital flip requires very extreme eccentricity. In the current simulations, we consider a planetary perturber, and therefore we adopt smaller $a_{1,i}$ relative to the previous study to a sub-stellar perturber. Thus, the tidal circularization always happens before the orbital flip. As a result, no RHJ is produced. In the fiducial case, we adopt the disruption radius ≈ 0.0126 AU with $f = 2.7$, thus one may expect the $q_{1,\rm min} = 0.0126$ AU line as the boundary between PHJ and TD. The black line corresponds to our analytical estimate of $q_{1,\rm min} = 0.0126$ AU derived from equation (4.8), which is qualitatively consistent with the simulation results. The detailed consideration is presented in subsection 4.4.2.

Non-migrating planets (NM; 13.6%) are located around the edge of bottom-left and upper-right region in Figure 4.16, but the migration boundaries between NM and PHJ/TD do not simply follow the analytical extreme eccentricity condition (red dashed lines). Instead, the migration boundaries between NM and PHJ/TD are determined by the maximum simulation time that we adopted (*i.e.*, $T_{\rm max} = 10^{10}$ yr). The detailed analytical consideration is presented in subsection 4.4.2.

In summary, our simulations indicate that CHEM can not produce counter-orbiting HJs, but produces PHJs to some degree for systems with a giant gas inner planet and a planetary outer perturber. We also reconfirm that the SRFs are important on the orbital evolution of the inner planet in such systems. The detailed analytical consideration incorporating the SRFs will be presented in the next subsection.

4.4.2 Analytical Interpretation of the Fiducial Case

Boundary between PHJ and TD

The boundary between PHJ and TD is determined basically by the Roche limit. In the fiducial case, we adopt $f = 2.7$ and thus the Roche limit becomes ≈ 0.0126 AU. We attempt to set $q_{1,\rm min} = R_{\rm roche}$ derived from equation (4.8) with $\varpi_f = 0$ to analytically estimate this boundary. The result is plotted with the black solid line in Figure 4.16.

We observe that our analytical estimate of this boundary is qualitatively in agreement with the numerical results. This analytical estimate is accurate for $e_{1,i} < 0.75$, but becomes less accurate for $e_{1,i} > 0.75$; in the latter case, our simulations indicate that HJs can form in the region where $q_{1,\rm min} < R_{\rm roche}$.

The following two effects change the analytical estimate of $q_{1,\rm min}$ on the basis of equation (4.8), which may account for the discrepancy. One is dissipative tides, which decreases e_1 further. Thus, the actual $q_{1,\rm min}$ tends to be larger than the analytical estimate based on equation (4.8), and the boundary between PHJ and TD moves upwards. The importance of dissipative tides increases for a higher $e_{1,i}$, since the inner planet spends more time in a high-e phase. The other is the break down of the exact coplanar condition. Equation (4.8) is based on the assumption of the exact coplanar orbit, but we adopt $i_{12,i} = 6^\circ$ in the fiducial case of our simulations. The non-zero $i_{12,i}$ increases the maximum achievable eccentricity due to the angular momentum conservation, and moves the boundary between PHJ and TD downwards. Since the amplitude of the inclination oscillation increases as $e_{1,i}$ decreases, this effect plays a more important role in the lower $e_{1,i}$ region.

Boundaries between NM and PHJ/TD

The lower boundary between NM and PHJ is determined by the epoch when the inner planet migrates to become a HJ within $T_{\rm max} = 10^{10}$ yr. The upper boundary between NM and TD is similarly determined, but in this case, the orbital angular momentum loss of the inner planet is rapid, and thus there is no stable HJ in between. We will explain

the behavior in detail in Figure 4.17 later. As shown in Figure 4.16, $q_{1,\min} = 0.05$ AU plotted in blue solid lines empirically shows good agreement with both the lower and upper migration boundaries in the numerical simulation. This consistency may reflect some correlation between $q_{1,\min}$ and the migration timescale, the timescale for the planet becoming a HJ.

Indeed, the basic mechanism to determine the migration boundary is tides, which are very sensitive to $q_{1,\min}$. A more precise approach to determine the migration boundary is to use the equations of motion directly. The migration timescale is determined by the evolution equations of a_1 and e_1 governed by planetary tides, which are given as (Correia et al. 2011)

$$\dot{a}_1 = 2\frac{\tilde{K_1}}{a_1^7}\left(f_2(e_1)\cos\theta_1\frac{\Omega_\mathrm{p}}{n_1} - f_3(e_1)\right), \tag{4.12}$$

$$\dot{e}_1 = 9\frac{\tilde{K_1}}{a_1^8}\left(\frac{11}{18}f_4(e_1)\cos\theta_1\frac{\Omega_\mathrm{p}}{n_1} - f_5(e_1)\right)e_1, \tag{4.13}$$

where θ_1 is the angle between the spin of the inner planet and the inner orbit, n_1 is mean motion of the inner planet, and

$$\tilde{K_1} = \Delta t_\mathrm{p}\frac{3k_{2,1}Gm_0(m_0+m_1)R_1^5}{m_1}, \tag{4.14}$$

$$f_2(e) = \frac{1+15e^2/2+45e^4/8+5e^6/16}{(1-e^2)^6}, \tag{4.15}$$

$$f_3(e) = \frac{1+31e^2/2+255e^4/8+185e^6/16+25e^8/64}{(1-e^2)^{15/2}}, \tag{4.16}$$

$$f_4(e) = \frac{1+3e^2/2+e^4/8}{(1-e^2)^5}, \tag{4.17}$$

$$f_5(e) = \frac{1+15e^2/4+15e^4/8+5e^6/64}{(1-e^2)^{13/2}}, \tag{4.18}$$

where Δt_p is the tidal delay time of the inner planet which is related to the viscous timescale by $t_{\mathrm{v,p}} = 3(1+k_{2,1})R_1^3/(Gm_1\Delta t_\mathrm{p})$.

Because of the quick tidal realignment due to efficient planetary tides, the spin-orbit angle of the inner planet, θ_1, effectively vanishes, and the spin rate of the inner planet, Ω_p, reaches the following equilibrium state in a very short timescale (Correia et al. 2011):

$$\frac{\Omega_\mathrm{p}}{n_1} = \frac{f_2(e_1)}{f_1(e_1)}, \tag{4.19}$$

where

$$f_1(e) = \frac{1+3e^2+3e^4/8}{(1-e^2)^{9/2}}. \tag{4.20}$$

Therefore, equations (4.12) and (4.13) reduce to the following simpler form

$$\dot{a}_1 = 2\frac{\tilde{K}_1}{a_1^7}\left(\frac{f_2^2(e_1)}{f_1(e_1)} - f_3(e_1)\right), \tag{4.21}$$

$$\dot{e}_1 = 9\frac{\tilde{K}_1}{a_1^8}\left(\frac{11}{18}\frac{f_4(e_1)f_2(e_1)}{f_1(e_1)} - f_5(e_1)\right)e_1. \tag{4.22}$$

Nevertheless, equations (4.21) and (4.22) cannot be yet solved analytically. In order to analytically estimate the migration timescale, we further assume that the migration process may be divided into two stages, eccentricity oscillation and circularization, based on the orbital evolution of the inner planet.

Figure 4.17a plots a typical example of the dynamical evolution near the lower boundary between NM and PHJ, corresponding to point A in Figure 4.16. During the eccentricity oscillation ($t \leq 3 \times 10^8$yrs), the maximum eccentricity of the inner planet in each cycle, $e_{1,\max}$, is approximately constant against time, while the amplitude of the eccentricity variation damps. Eventually, the eccentricity oscillation stops ($t \geq 3 \times 10^8$ yrs) and the inner planet starts its circularization stage.

To distinguish the behavior of the two different stages, we introduce the dimensionless orbital angular momentum of the inner planet:

$$\frac{p}{p_i} = \sqrt{\frac{a_1(1-e_1^2)}{a_{1,i}(1-e_{1,i}^2)}}, \tag{4.23}$$

which is plotted in the third panel of Figure 4.17a. It indicates that the eccentricity oscillation stage also corresponds to the oscillation of p/p_i, where p/p_i is constant during the circularization stage.

Now, the migration timescale is simply approximated by the sum of the timescales of the above two stages:

$$t_{\rm mig,1} = t_{\rm eo} + t_{\rm cir}. \tag{4.24}$$

We present how to compute $t_{\rm eo}$ and $t_{\rm cir}$ separately below.

We first consider $t_{\rm eo}$. In the eccentricity oscillation stage, $e_{1,\max}$ is constant and can be computed from equation (4.8). The minimum eccentricity of the inner planet in each cycle, $e_{1,\min}$, steadily increases. The end of the eccentricity oscillation stage is the epoch that the amplitude of the eccentricity variation approximately vanishes. In order to separate the two stages, we denote $e_{1,\rm min,crit}$ as the value of $e_{1,\min}$ at the end of the eccentricity oscillation stage. According to Anderson et al. (2016), we rewrite $e_{1,\min}$ in terms of Δj, where

$$\Delta j = j_{1,\min} - j_{1,\max} = \sqrt{1-e_{1,\min}^2} - \sqrt{1-e_{1,\max}^2}. \tag{4.25}$$

Then we attempt to parameterize $e_{1,\mathrm{min,crit}}$ by assuming a constant critical value of Δj_{crit} as follows:

$$e_{1,\mathrm{min,crit}} = \sqrt{1 - \left(\Delta j_{\mathrm{crit}} + \sqrt{(1 - e_{1,\mathrm{max}}^2)}\right)^2}. \tag{4.26}$$

Once $e_{1,\mathrm{min,crit}}$ and $e_{1,\mathrm{max}}$ are specified, the semi-major axis of the inner planet at the end of its eccentricity oscillation stage, $a_{1,\mathrm{crit}}$, is obtained from equation (4.8), combined with the conservation of the potential energy during each eccentricity oscillation cycle.

Using this $a_{1,\mathrm{crit}}$, t_{eo} is written as

$$t_{\mathrm{eo}} = \int_{t(a_{1,i})}^{t(a_{1,\mathrm{crit}})} dt \tag{4.27}$$

The integral in the right-hand-side of the above equation is estimated as follows.

During the eccentricity oscillation cycle, the damping of a_1 due to the tidal interaction happens only for a short period when e_1 is close to $e_{1,\mathrm{max}}$. Except for that period, a_1 is approximately constant. Anderson et al. (2016) found that the fraction of the time that the inner planet is in the high-e phase ($e_1 \approx e_{1,\mathrm{max}}$) in each eccentricity oscillation cycle is given by $\sqrt{1 - e_{1,\mathrm{max}}^2}$. In reality they derived the above result in the Lidov-Kozai regime, but it is also applicable for the near-coplanar configuration that we consider here. Therefore t_{eo} should be given as

$$t_{\mathrm{eo}} = \frac{\Delta t(e_{1,\mathrm{max}})}{\sqrt{1 - e_{1,\mathrm{max}}^2}}. \tag{4.28}$$

where $\Delta t(e_{1,\mathrm{max}})$ is the total duration when the inner planet has $e_1 \approx e_{1,\mathrm{max}}$ during the entire eccentricity oscillation stage:

$$\Delta t(e_{1,\mathrm{max}}) \approx \int_{a_{1,\mathrm{crit}}}^{a_{1,i}} \left|\frac{dt}{da_1}\right|_{e_1 = e_{1,\mathrm{max}}} da_1. \tag{4.29}$$

Equation (4.29) is further approximated and evaluated using equations (4.21):

$$\begin{aligned}
\Delta t(e_{1,\mathrm{max}}) &\approx \int_{a_{1,\mathrm{crit}}}^{a_{1,i}} \left|\frac{dt}{da_1}\right|_{e_1 = e_{1,\mathrm{max}}} da_1 \\
&= \int_{a_{1,\mathrm{crit}}}^{a_{1,i}} \frac{a_1^7}{2\tilde{K}_1} \left(\frac{f_2^2(e_{1,\mathrm{max}})}{f_1(e_{1,\mathrm{max}})} - f_3(e_{1,\mathrm{max}})\right)^{-1} \\
&= \frac{a_{1,i}^8 - a_{1,\mathrm{crit}}^8}{16\tilde{K}_1} \left(\frac{f_2^2(e_{1,\mathrm{max}})}{f_1(e_{1,\mathrm{max}})} - f_3(e_{1,\mathrm{max}})\right)^{-1}.
\end{aligned} \tag{4.30}$$

Next, we move to the calculation of t_{cir}. The equilibrium value of the dimensionless orbital angular momentum of the inner planet in the circularization stage, p_{eq}/p_i, can be

obtained at the end of the eccentricity oscillation stage as

$$\frac{p_{\rm eq}}{p_i} = \sqrt{\frac{a_{1,\rm crit}(1-e_{1,\rm max}^2)}{a_{1,i}(1-e_{1,i}^2)}}. \tag{4.31}$$

Then, we define the end of the circularization stage when the inner planet becomes a HJ with $e_1 < 0.01$. Thus, from equation (4.22), $t_{\rm cir}$ can be written as

$$\begin{aligned} t_{\rm cir} &= \int_{0.01}^{e_{1,\rm max}} \left|\frac{dt}{de_1}\right|_{a_1=p_{\rm eq}^2/(1-e_1^2)} de_1 \\ &= \int_{0.01}^{e_{1,\rm max}} \frac{p_{\rm eq}^{16}}{9\tilde{K}_1}\frac{1}{e_1(1-e_1^2)^8}\left(\frac{11}{18}\frac{f_4(e_1)f_2(e_1)}{f_1(e_1)} - f_5(e_1)\right)^{-1} de_1. \end{aligned} \tag{4.32}$$

The migration boundary is determined by the epoch when $t_{\rm mig,1}$ is equal to $T_{\rm max}$ (10^{10} yrs in our simulations). The resulting lower and upper migration boundaries of ϵ in the fiducial case from equations (4.24), (4.30), and (4.32) are shown in Figure 4.16 by magenta lines. We observe that they are in good agreement with the numerical simulations. This analytical estimate is useful in interpreting the present simulation results. In addition, it provides a useful guidance for future numerical simulations in near-coplanar hierarchical triple systems and the same result is also applicable to the Lidov-Kozai regime.

In Figure 4.16 and also Figure 4.19 below, we plot the boundary corresponding to $\Delta j_{\rm crit} = 0.04$. Indeed, the results turn out to be fairly insensitive to the value of $\Delta j_{\rm crit}$ in a certain range. In the upper panel of Figure 4.17a, the black, magenta, and blue vertical lines show the analytical estimates for $t_{\rm eo}$ and $t_{\rm mig,1}$ with $\Delta j_{\rm crit} = 0.03, 0.04$, and 0.05, respectively. We observe that the smaller $\Delta j_{\rm crit}$ implies a longer timescale of the eccentricity oscillation stage and a shorter timescale of the circularization stage. The dependence of $\Delta j_{\rm crit}$ on the migration timescale is determined by the above two competitive effects. Nevertheless, we confirm that adopting different $\Delta j_{\rm crit}$ does not qualitatively change the estimated timescale.

Stopping Time of NM and PHJ

The stopping time, $T_{\rm s}$, the time at which each simulation is stopped, provides an important hint on the stability of the system. Figure 4.18 presents the stopping time of NM and PHJ (left), and TD (right) corresponding to our fiducial runs in Figure 4.16. In this subsection, we discuss the stopping time of NM and PHJ.

Since NMs stay almost at the initial position until the maximum simulation time, $T_{\rm max}$, the stopping time of NM is simply $T_{\rm max}$ that we adopt. The stopping time of PHJ is determined by the epoch when the inner planet satisfies $a_{1,f} < 0.1$ AU and $e_{1,f} < 0.01$ simultaneously, which is equal to the migration timescale. As shown in the left panel of Figure 4.18, the stopping time of PHJ almost monotonically decreases from $T_{\rm max} = 10^{10}$ yr to $\sim 10^6$ yr as ϵ_i increases.

Depending on the migration timescale, we adopt two different analytical approaches to understand the above behavior. For $T_s = 10^{10}$ yr and 10^9 yr, we use equation (4.24), but for $T_s = 10^8$ yr and 10^7 yr, we have to use a different approach because the orbit evolves in a different manner than in the previous case. In PHJ region, as ϵ_i increases, the path to PHJ happens over a much smaller timescale. The time evolution for an example of PHJ systems in that region, corresponding to point B in Figure 4.16, is plotted in Figure 4.17b with $T_s \sim 10^7$ yr. As shown in its second panel, $1 - e_1$ monotonically decreases and reaches less than 10^{-2}, when tides dominate the orbital evolution of the inner planet and circularize its orbit within several million years. During the circularization stage, the inner orbital angular momentum is conserved. Unlike the systems near the lower migration boundary (Figure 4.17a), the eccentricity oscillation does not happen in this region. Thus, the migration timescale becomes the sum of the timescales of the first eccentricity growth, $t_{\rm eg}$, and subsequent tidal circularization with the constant inner orbital angular momentum. Following Petrovich (2015b), we compute $t_{\rm eg}$ from his $\tau_{\rm in}/\alpha$:

$$t_{\rm eg} = \frac{4}{3n_1}\left(\frac{m_0}{m_2}\right)\left(\frac{a_2}{a_1}\right)^4. \tag{4.33}$$

The circularization timescale can be computed from equation (4.32). Then, the total migration timescale in this region is given by

$$t_{\rm mig,2} = t_{\rm eg} + t_{\rm cir}. \tag{4.34}$$

The left panel of Figure 4.18 plots the analytical estimate of the four migration timescales: for 10^{10} yr and 10^9 yr, we use equation (4.24), and for 10^8 yr and 10^7 yr, we adopt equation (4.34). Combining above two methods, we find that the results are roughly consistent with our numerical simulation.

Stopping Time of TD

The stopping time of TD is determined by the epoch when q_1 reaches less than the Roche limit. The results corresponding to the fiducial runs in Figure 4.16 are shown in the right panel of Figure 4.18. It implies the stopping time of the majority of TDs is $\sim 10^6$ yr, indicating that these planets fall into the Roche limit at the first few extreme eccentricity approaches. In the region close to the upper migration boundary, T_s becomes longer as ϵ_i increases. The time evolution for an example of TD systems in that region, corresponding to point C in Figure 4.16, is shown in Figure 4.17c. This system has $T_s \sim 10^9$ yr. As shown in its bottom panel, $|\omega_1 - \omega_2|$ librates with decreasing amplitude, and then starts circulating at $\sim 7 \times 10^8$ yr. Exactly at the transition between libration and circulation, the inner planet acquires extreme eccentricity and therefore becomes TD.

4.4.3 Fate of the Inner Planet in Non-fiducial Models

The previous subsections presented the simulation result and its implications in the fiducial case. Next we consider the parameter dependence of the final outcomes. The results

on $(e_{1,i}, \epsilon_i)$ plane for selected six different cases are plotted in Figure 4.19 (see also Table 4.2).

The parameter dependence can be understood by comparing each model with the fiducial case. In the case a200 ($a_2 = 200$ AU), shown in the left upper panel of Figure 4.19, the fraction of NMs increases since for the same ϵ_i, a larger $a_{1,i}$ corresponds to a larger $q_{1,\min}$. The right upper panel of Figure 4.19 plots the case i30 ($i_{12,i} = 30°$). The fraction of TDs increases since the larger amplitude of $i_{12,i}$ oscillation induces a higher maximum achievable eccentricity of the inner planet. In the case t00030 ($t_{\rm v,p} = 0.003$ yr), shown in the left middle panel of Figure 4.19, the stronger tides on the inner planet cause it to suffers from the very efficient tidal dissipation even at a relatively larger pericenter distance, resulting in a higher fraction of PHJs. The middle right panel of Figure 4.19 corresponds to the case f216 (f=2.16), in which the smaller disruption radius results in less TDs and more PHJs.

Such dependence on m_2, $i_{12,i}$, $t_{\rm v,p}$, and f is similar to the sub-stellar perturber case considered in previous section, but the dependence on m_2 generates a different feature. Thus, in this subsection, we mainly focus on the dependence on m_2. Here we restrict our attention to the planetary perturber. We perform eight different sets of runs with $m_2 = 10M_{\rm J}$, $7M_{\rm J}$, $6M_{\rm J}$, $5M_{\rm J}$ (fiducial), $4M_{\rm J}$, $3M_{\rm J}$, $2M_{\rm J}$, and $1M_{\rm J}$. The final states of the inner planet for those models are summarized in Table 4.2. Also, two examples with $m_2 = 3M_{\rm J}$ and $1M_{\rm J}$ on $(e_{1,i}, \epsilon_i)$ plane are plotted in the left and right bottom panels of Figure 4.19.

Table 4.2 shows the fraction of NMs increases as m_2 decreases. As shown in the right panel of Figure 4.1, the extreme eccentricity region becomes narrower as m_2 decreases. In addition, the relative importance of GR increases as m_2 decreases according to equation (4.5). Therefore the SRFs more efficiently limit the extreme eccentricity growth for smaller m_2. The above two facts account for the anti-correlation between the fraction of NMs and the value of m_2.

The fraction of TDs decreases as m_2 decreases, which can be understood as follows. The orbital interaction is the major driving source for the inner planet acquiring the extreme eccentricity. The weaker interaction (smaller m_2) leads to the smaller maximum achievable eccentricity of the inner planet, and therefore to the larger $q_{1,\min}$. As a result, less systems suffer from the tidal disruption.

As m_2 decreases, the fraction of NMs increases but that of TDs decreases. Thus the change of the fraction of PHJs depends on these competitive effects. In our simulations, the fraction of PHJs increases as m_2 decreases from $10M_{\rm J}$ to $2M_{\rm J}$, and even more significantly decreases as m_2 decreases from $2M_{\rm J}$ to $1M_{\rm J}$. In the latter case, the migration region becomes significantly narrower as shown in the right bottom panel of Figure 4.19. Most of simulation runs end up with NMs. The above mentioned trends suggest that in order to form HJ in CHEM, the outer perturber should be neither too small to over-limit the migration region, nor too large to be dominated by disruption. An intermediate massive perturber is preferred.

Recently, Anderson et al. (2016) examined the dependence of the final spin-orbit

angle on the mass of the central star in the Lidov-Kozai migration with a circular outer perturber. They found that the systems with more massive central stars have broader distribution of the spin-orbit angle. Thus, we attempt to see the possible dependence of the spin-orbit angle on the mass of the central stars in CHEM. The comparison of cases $m_0 = 0.4M_\odot$ and $1.4M_\odot$ cases against our fiducial case ($m_0 = 1M_\odot$) indicates very similar distribution for the spin-orbit angle as shown in Figure 4.20. This is indeed consistent with the sub-stellar perturber case; see Figure 4.13. Therefore, the spin-orbit angle in CHEM does not seem to be sensitive to the mass of the central star.

4.4.4 Distribution of Final Semi-major Axis $a_{1,f}$

The final distribution of the orbital elements in our simulations provide possible hints in distinguishing CHEM from the other HJ formation mechanisms. In this subsection, we discuss the distribution and its parameter dependence of the final semi-major axis of the resulting HJs, $a_{1,f}$, in our simulations. Figure 4.21 presents $a_{1,f}$ against ϵ_i in six selected simulation sets. The colors represent the stopping time $T_{\rm s}$ in log scale. Note, in the case of PHJs, $T_{\rm s}$ is equivalent to their migration timescale.

We plot $a_{1,f}$ in the fiducial case in the left upper panel of Figure 4.21. There are mainly two important features. One is that $a_{1,f}$ is distributed with $\sim 0.025 - 0.096$ AU, which is qualitatively consistent with the observation. The other is that $T_{\rm s}$ basically increases as $a_{1,f}$. The detailed explanation of the above two features is presented below.

In the fiducial case, the lower boundary of $a_{1,f} \sim 0.025$ AU is roughly consistent with twice the Roche limit ~ 0.0126 AU. It comes from the fact that $a_{1,f} \approx 2q_{1,\rm min}$ during tidal circularization due to the constant inner orbital angular momentum as described in subsection 4.4.2. Here $q_{1,\rm min}$ of the resulting HJs is larger than the Roche limit in order to survive the disruption. In the case of f216 ($f = 2.16$) with less restrictive disruption radius shown in the bottom right panel of Figure 4.21, the lower boundary of $a_{1,f}$ reduces to ~ 0.02 AU. The upper boundary of $a_{1,f}$ increases as the efficiency of tides, since the planetary orbit is circularized within $T_{\rm max}$ even at a larger distance if tides are stronger. In the case of t00030 ($t_{\rm v,p} = 0.003$ yr) with stronger tides shown in the left bottom panel of Figure 4.21, the upper boundary is extended to ~ 0.13 AU. Compared with the fiducial case, the range of $a_{1,f}$ is fairly insensitive to the change of the parameters of the outer perturber, a_2, m_2, and i_{12}, as shown in the right upper, the left middle, and the right middle panels of Figure 4.21, respectively.

The trend that $T_{\rm s}$ (also the migration timescale) basically increases as $a_{1,f}$ holds for all the cases. This trend can be explained by the correlation between $q_{1,\rm min}$ and the migration timescale. During the tidal circularization, the correlation $a_{1,f} \approx 2q_{1,\rm min}$ holds , where $q_{1,\rm min}$ is very sensitive to the strength of tides, and therefore to the migration timescale. This trend is broken for the systems near the upper migration boundary, which are located in $\epsilon_i > 0.1$ as shown in Figure 4.21. In that region, the systems take a longer time to reach $q_{1,\rm min}$. This is the case for point C in Figure 4.16, and its dynamical behavior is plotted in Figure 4.17c. The system reaches $q_{1,\rm min}$ at the transition epoch of $|\omega_1 - \omega_2|$

from libration to circulation as discussed in subsection 4.4.2. Since a smaller amplitude of libration for $|\omega_1 - \omega_2|$ has a strongly modulated envelope of e_1, the time spent near $q_{1,\min}$ becomes smaller to avoid fast circularization or disruption (Dawson et al. 2014).

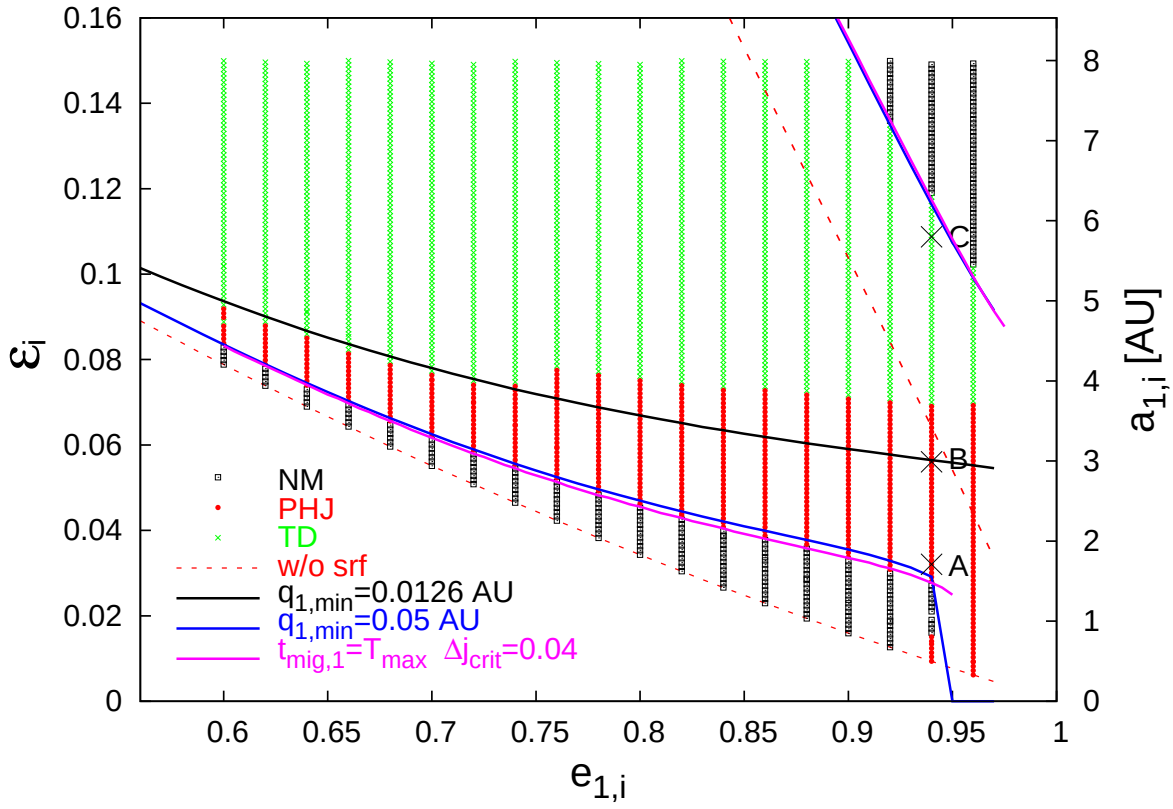

Figure 4.16: Results of the inner planet on $(e_{1,i}, \epsilon_{1,i})$ plane for the fiducial case in systems with a giant gas inner planet and a planetary outer perturber: $m_0 = 1M_\odot, m_1 = 1M_\mathrm{J}, m_2 = 5M_\mathrm{J}, e_{2,i} = 0.6, a_2 = 50$ AU, $t_{\mathrm{v,p}} = 0.03$ yr, and $f = 2.7$. $e_{1,i}$ is varied between 0.6 and 0.96 with a constant interval of 0.02, and ϵ_i is varied between ϵ_L derived from equation (4.3) and 0.15 with a constant interval of 0.001. The final states are indicated by black open squares for non-migrating planets (NM), red filled circles for prograde HJs (PHJ), and green crosses for tidally disrupted planets (TD), respectively. The red dashed lines correspond to the extreme eccentricity condition derived from equation (4.3). The blue and black lines correspond to the desired ϵ_i $(a_{1,i})$ to reach $q_{1,\mathrm{min}} = 0.05$ and 0.0126 AU including the SRFs effect. The magenta lines correspond to the migration boundary $(t_{\mathrm{mig},1} = 10^{10}$ yrs) of the analytical estimate derived from equations (4.24), (4.30), and (4.32) with $\Delta j_{\mathrm{crit}} = 0.04$. The points A, B, and C correspond to Figure 4.17a, b, and c, respectively.

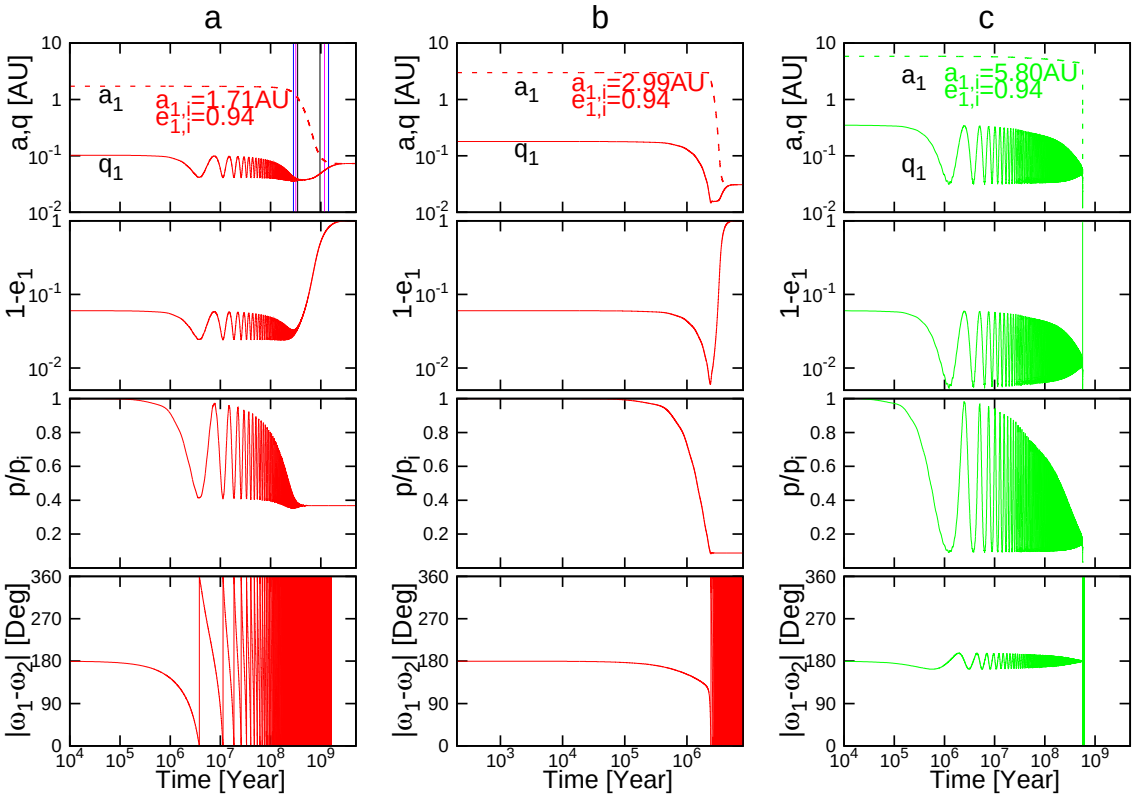

Figure 4.17: Orbital evolution of PHJ and TD in the fiducial case with $e_{1,i} = 0.94$ for three different $a_{1,i}$. The evolution of a_1 and q_1, e_1, p/p_i, and $|\omega_1 - \omega_2|$ are presented from top to bottom, where a_1 is plotted in dashed lines, q_1, e_1, p/p_i, and $|\omega_1 - \omega_2|$ are shown in solid lines, respectively. Panel a is $a_{1,i} = 1.71$ AU which corresponds to the region close to the lower migration boundary (point A in Figure 4.16); Panel b has $a_{1,i} = 2.99$ AU, which is inside the PHJ region with intermediate ϵ_i (point B in Figure 4.16); Panel c is $a_{1,i} = 5.80$ AU, which corresponds to the tidal disruption region near the upper migration boundary (point C in Figure 4.16). The solid vertical lines in the upper plot of Panel a refer to our analytical estimate of the migration boundary of $t_{\rm eo}$ and $t_{\rm mig,1}$, where black, magenta, and blue lines correspond to $\Delta j_{\rm crit} = 0.03, 0.04$, and 0.05, respectively.

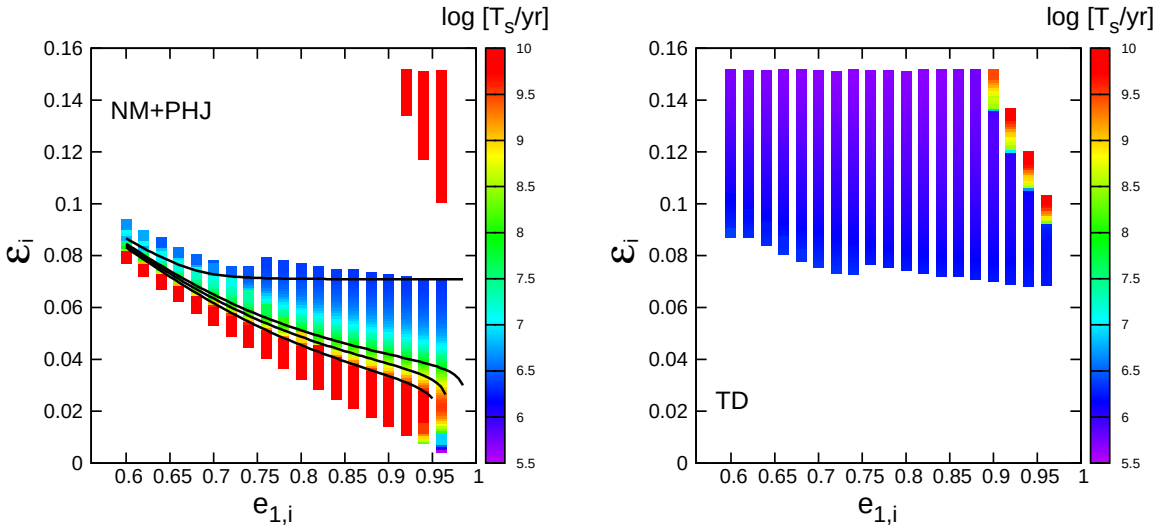

Figure 4.18: Stopping time, $T_{\rm s}$, time at which each simulation is stopped is plotted in log scale in the fiducial case. $T_{\rm s}$ is defined as $T_{\rm max}$ for NMs, the migration timescale for PHJs, and the timescale to reach less than the Roche limit for TDs. The left panel refers to $T_{\rm s}$ of NMs and PHJs. The right panel presents $T_{\rm s}$ of TDs. The black solid lines in the left panel correspond to our analytical estimate of the migration timescale, 10^{10} yr, 10^{9} yr, 10^{8} yr, and 10^{7} yr, from bottom to top.

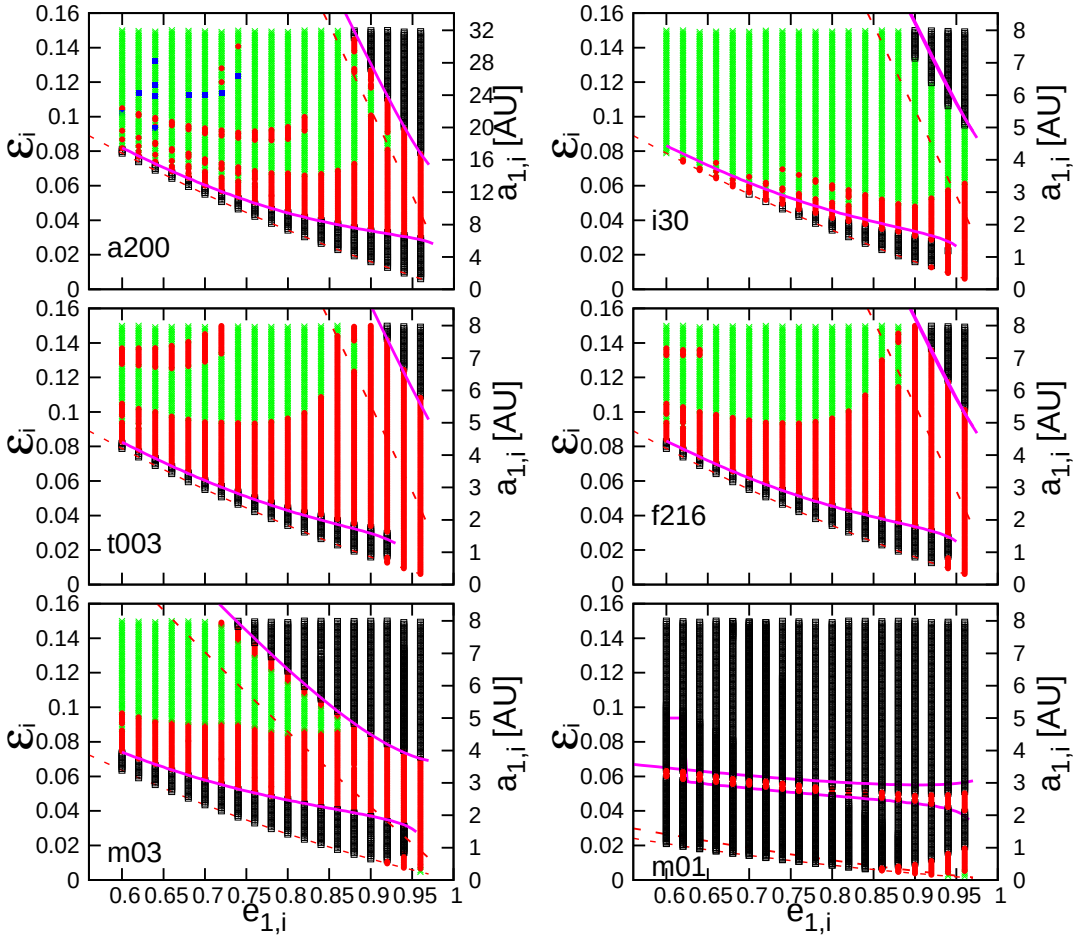

Figure 4.19: Fate of the inner planet on $(e_{1,i}, \epsilon_i)$ plane for six selected sets, left upper: a200 ($a_{2,i} = 200$ AU); right upper: i30 ($i_{12,i} = 30°$); left middle: t003 ($t_{\rm v,p} = 0.03$ yr); right middle: f216 ($f = 2.16$); left bottom: m03 ($m_2 = 3M_{\rm J}$); and right bottom: m01 ($m_2 = 1M_{\rm J}$), respectively. The red dashed lines show the extreme eccentricity condition derived from equation (4.3). The magenta solid lines correspond to the analytical estimate of the migration boundary obtained from equation (4.24) with $\Delta j_{\rm crit} = 0.04$.

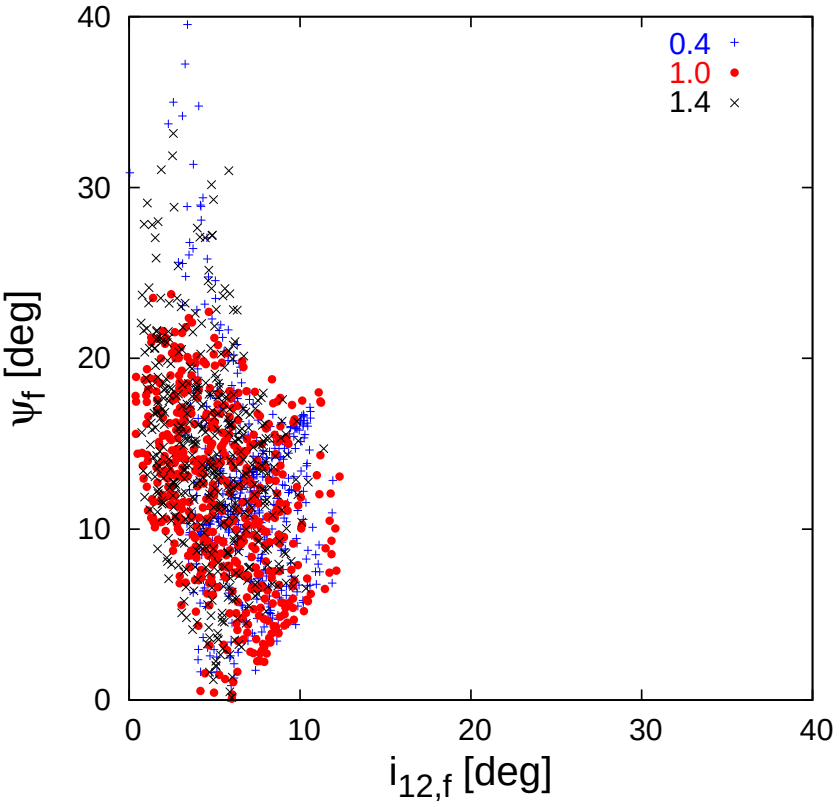

Figure 4.20: Orbital mutual orbital inclination, $i_{12,f}$, against the spin-orbit angle between the central star and the inner planet, ψ_f, for resulting PHJs among $m_0 = 0.4M_\odot$ (blue plus), the fiducial case ($m_0 = 1M_\odot$, red dot), and $m_0 = 1.4M_\odot$ (black cross).

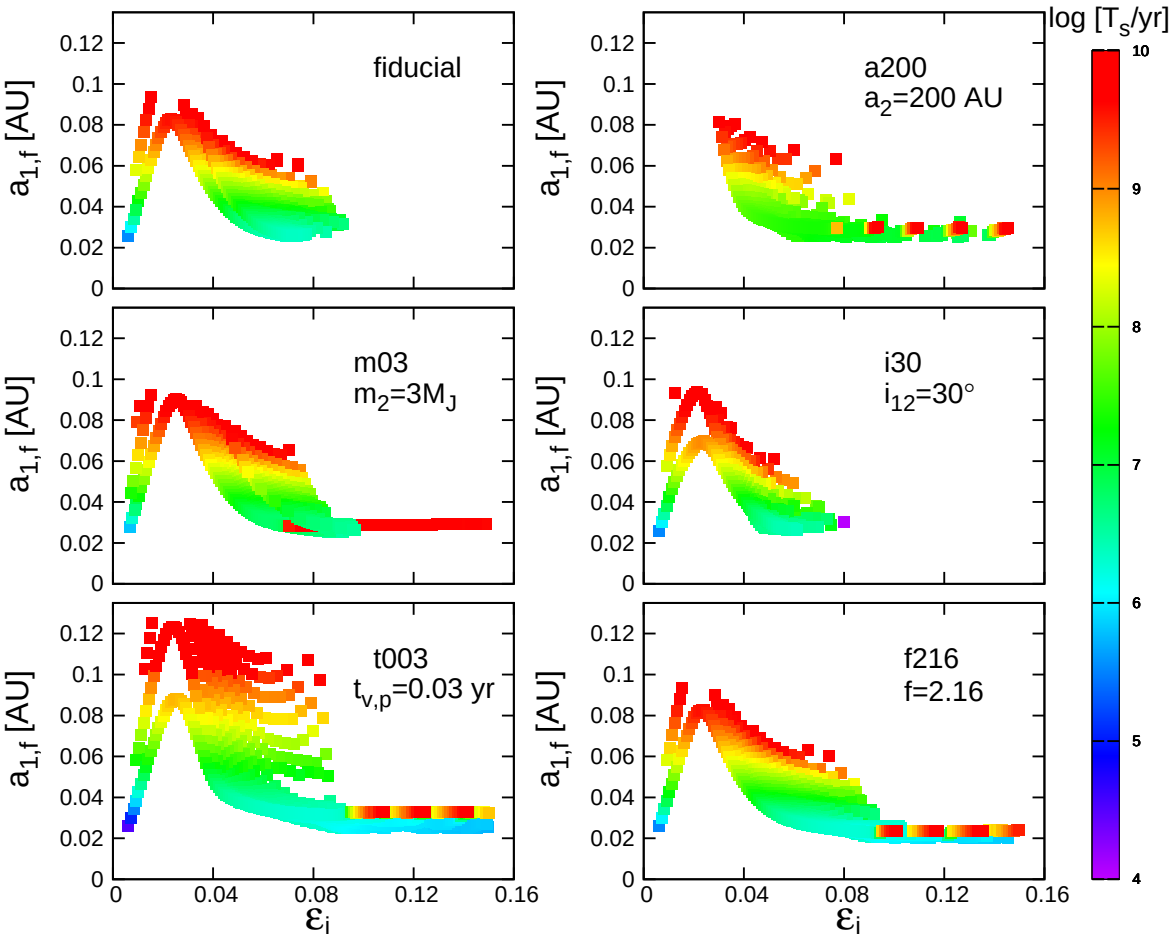

Figure 4.21: Final semi-major axis of resulting HJs, $a_{1,f}$, of six selected cases against ϵ_i, left upper: fiducial; right upper: a200 ($a_{2,i} = 200$ AU); left middle: m03 ($m_2 = 3M_J$); right middle: i30 ($i_{12,i} = 30°$); left bottom: t003 ($t_{v,p} = 0.03$ yr); and right bottom: f216 ($f = 2.16$), respectively. The different colors indicate the different stopping time T_s in log scale.

4.5 Super-Earth with a Planetary Outer Perturber

About forty close-in super-Earths ($a_1 < 0.1$ AU) have been observed by Kepler so far. The origin of those planets is also an open question similarly as HJs. It was proposed that close-in super-Earths may form in situ or by disk migration, but neither of them can fully explain the current observation. The former scenario requires that the protoplanetary disk should be at least 20 times more massive than that in the minimum-mass solar nebula (Raymond & Cossou 2014). The latter scenario predicts that the multi-planets should be in low-order mean motion resonance, but it is not supported by the observation (Chatterjee et al. 2015). Recently, Rice (2015) suggested that the ultrashort-period super-Earth Kepler-78b with $a = 0.009$ AU may be explained by the Lidov-Kozai migration, which implies that the dynamical processes may also contribute to the formation of close-in super-Earths at least partially. In this section, therefore, we examine to see if CHEM can produce close-in super-Earths. To be more specific, we consider an inner super-Earth at ~ 1 AU and an outer eccentric planetary perturber at ~ 10 AU initially, because super-Earths are almost preferentially found within the snow line from the observation. Our initial condition differs from Rice (2015) in considering the planetary perturber instead of the stellar perturber, and such a configuration may result from planet-planet scattering.

We perform the numerical simulations following the procedure described in subsection 4.3.1, but we change the inner planetary mass and radius, tidal strength, and disruption radius in order to adjust to the current situation. We adopt initially $m_1 = 5M_\oplus$, $i_{12} = 6°$, $\psi = 0°$, $\omega_1 = 0°$, $\omega_2 = 0°$, $l_1 = 180°$, $l_2 = 0°$, and $f = 2.44$ for all the models. The radius of the inner planet is determined by the planet mass-radius relationship: $M/M_\oplus = 2.69(R/R_\oplus)^{0.93}$ (Weiss & Marcy 2014). We perform ~ 300 different runs by systematically varying $(e_{1,i}, \epsilon_i)$. $e_{1,i}$ is varied between 0.6 and 0.96 with a constant interval of 0.04, and ϵ_i is varied between $\epsilon_{\rm L}$ derived from equation (4.3) and 0.16 with a constant interval of 0.004. The other parameters for six different models are summarized in Table 4.3 together with the final fraction of the different outcomes. The resulting $(e_{1,i}, \epsilon_i)$ maps are presented in Figure 4.22. We first discuss the result in the fiducial case, and then consider the dependence on m_2, a_2, e_2, $t_{\rm v,p}$, and m_0.

In the fiducial case, SE-fid, we adopt $m_0 = 1.0M_\odot$, $a_2 = 10$ AU, $e_2 = 0.6$, $m_2 = 1M_{\rm J}$, and $t_{\rm v,p} = 0.001$ yr. The viscous timescale of the inner planet, $t_{\rm v,p} = 0.001$ yr, is taken from the value of Earth (Murray & Dermott 1999), which corresponds to the quality factor $Q \sim 100$ for a 1 yr orbital period. The resulting $(e_{1,i}, \epsilon_i)$ map of the fiducial case is shown in the left upper panel of Figure 4.22. Clearly, the overall distribution is very similar to the case of a giant gas inner planet with a planetary outer perturber as shown in Figure 4.16. The final outcomes are NM (19.9%), PSE (22.2%), and TD (57.9%), where PSE refers to the prograde close-in super-Earth ($a_{1,f} < 0.1$ AU, $i_{12,f} < 90°$). We note that we do not find any retrograde close-in super-Earth (RSE, $a_{1,f} < 0.1$ AU, $i_{12,f} > 90°$). The absence of RSE is supposed to be generic because the initial location of super-Earth is likely within the snow line, and therefore tides circularize the orbit before super-Earth acquires the extreme eccentricity necessary for the orbital flip. The migration boundary

between NM and PHJ for $t_{\rm mig,1} = 10^{10}$ yr based on equation (4.24) is plotted in magenta line, which is in good agreement with our numerical simulation.

Next, we consider the parameter dependence by comparing with the fiducial case. We find that the dependence on m_2, a_2, $e_{2,i}$, and $t_{\rm v,p}$ are similar to the cases for systems consisting of a giant gas inner planet with a sub-stellar outer perturber in section 4.3 and with a planetary outer perturber in section 4.4. In the case SE-5mj ($m_2 = 5M_{\rm J}$) shown in the right upper panel of Figure 4.22, decrease of NM and increase of TD are due to the stronger mutual orbital interaction that leads to a more extreme eccentricity. In the case SE-a50 ($a_2 = 50$ AU) plotted in the left middle panel of Figure 4.22, NM increases because a larger $a_{1,i}$ corresponds to a larger $q_{1,\rm min}$. The right middle panel of Figure 4.22 refers to the case SE-e08 ($e_{2,i} = 0.8$). PSE increases due to the smaller $a_{1,i}$ by scaling law according to equation (3.8). In the case SE-tv01 ($t_{\rm v,p} = 0.00001$ yr) shown in the left bottom panel of Figure 4.22, more systems survive as PSEs due to very strong tides.

In the case of simulations for super-Earth systems, we additionally consider the case with smaller m_0, because super-Earths are often found around M-dwarfs. The related case SE-04ms is shown in the right bottom panel of Figure 4.22, where we decrease the mass of the central star to $m_0 = 0.4M_\odot$. In this case, PSEs have a similar fraction compared with the fiducial case, but form in the lower ϵ_i region. The fraction of NM decreases from 19.9% in the fiducial case to 4.4%. This trend is due to decrease of the relative importance of the SRFs effect. The potential energy of GR ($\tilde{\phi}_{\rm GR}$) and tides ($\tilde{\phi}_{\rm tide}$) decrease with m_0, but that of orbital interaction ($\tilde{\phi}$) remains constant. Therefore the extreme eccentricity growth is less suppressed than in the fiducial case.

In summary, the overall distribution and parameter dependence in simulations are similar between super-Earth systems and giant gas planetary systems. No RSE is observed in our simulations, but CHEM can produce PSE to some degree. Thus, we conclude that CHEM is a possible channel to form close-in super-Earths.

4.6 Formation of Close Binaries

Binary configurations are very common in our universe, however, recent analysis of the eclipse time variation of Kepler binaries indicates that many of binaries are probably triples (Borkovits et al. 2016). Indeed, these must be hierarchical triples by considering the dynamical stability. Thus, many close binaries are likely produced in hierarchical triple evolution. Naoz et al. (2014) systematically studied the Lidov-Kozai migration in stellar triples with a large set of Monte Carlo simulations. They found that $\sim 21\%$ of all simulated systems end up with close binaries (< 16 days), and $\sim 4\%$ become merged systems. These merged systems have been proposed to explain the formation of blue stragglers.

In this section, we consider the possibility of forming close binaries in CHEM. We consider triple star system consisting of a sun-like primary star ($m_0 = 1M_\odot$, and $R_0 = 1R_\odot$), a second star ($m_1 = 0.5M_\odot$) and a distant stellar outer perturber ($m_2 = 1M_\odot$).

Table 4.3: Summary of parameters and the facts of simulation runs described in section 4.5.

Model	m_0 $M_\odot$	a_2 au	e_2	m_2 M_J	$t_{\mathrm{v,p}}$ yr	PSE	RSE	NM	TD
SE-fid	1.0	10	0.6	1	0.001	22.2%	0.0%	19.9%	57.9%
SE-5mj	1.0	10	0.6	5	0.001	12.5%	0.0%	0.0%	87.5%
SE-a50	1.0	50	0.6	1	0.001	16.6%	0.0%	22.7%	60.7%
SE-e08	1.0	10	0.8	1	0.001	55.6%	0.0%	12.0%	32.4%
SE-tv01	1.0	10	0.6	1	0.00001	100.0%	0.0%	0.0%	0.0%
SE-04ms	0.4	10	0.6	1	0.001	23.9%	0.0%	4.1%	72.0%

Note. PSE and RSE refer to prograde close-in super-Earth ($a_{1,f} < 0.1$ AU, $i_{12,f} < 90°$) and retrograde close-in super-Earth ($a_{1,f} < 0.1$ AU, $i_{12,f} > 90°$), respectively. All the models adopt $m_1 = 5M_\oplus$, $i_{12,i} = 6°$, $\omega_{1,i} = 0°$, $\omega_{2,i} = 0°$, $l_{1,i} = 180°$, $l_{2,i} = 0°$, $f = 2.44$, and $\psi_i = 0°$. For each model, we perform $\sim$ 300 runs by varying ($e_{1,i}$, ϵ_i) systematically.

We adopt $e_{2,i} = 0.6$, $i_{12,i} = 6°$, the viscous timescale for the inner pairs, $t_\mathrm{v} = 50$ yr, and $f = 2.44$ as the fiducial value. We survey ($e_{1,i}$, ϵ_i) following the methodology described in subsection 4.3.1. $e_{1,i}$ is varied between 0.6 to 0.9 with constant interval 0.1, and ϵ_i is varied between 0.015 to 0.15 with constant interval 0.008, respectively.

The results are shown in Figure 4.23. The left and right panels correspond to $a_2 =$ 5000 and 500 AU cases. We observe that the results are fairly insensitive to a_2. In both cases, most of the resulting systems remain their initial configurations; few end up with disruption; but no close binary form. Since tides on the stellar body is much weaker than on the planet, more systems tend to be tidally disrupted during the extreme eccentricity excursion. In addition, the extreme eccentricity region is significantly limited due to their comparable masses as described in subsection 4.2.1. In conclusion, the above results imply the difficulty to form close binaries in CHEM.

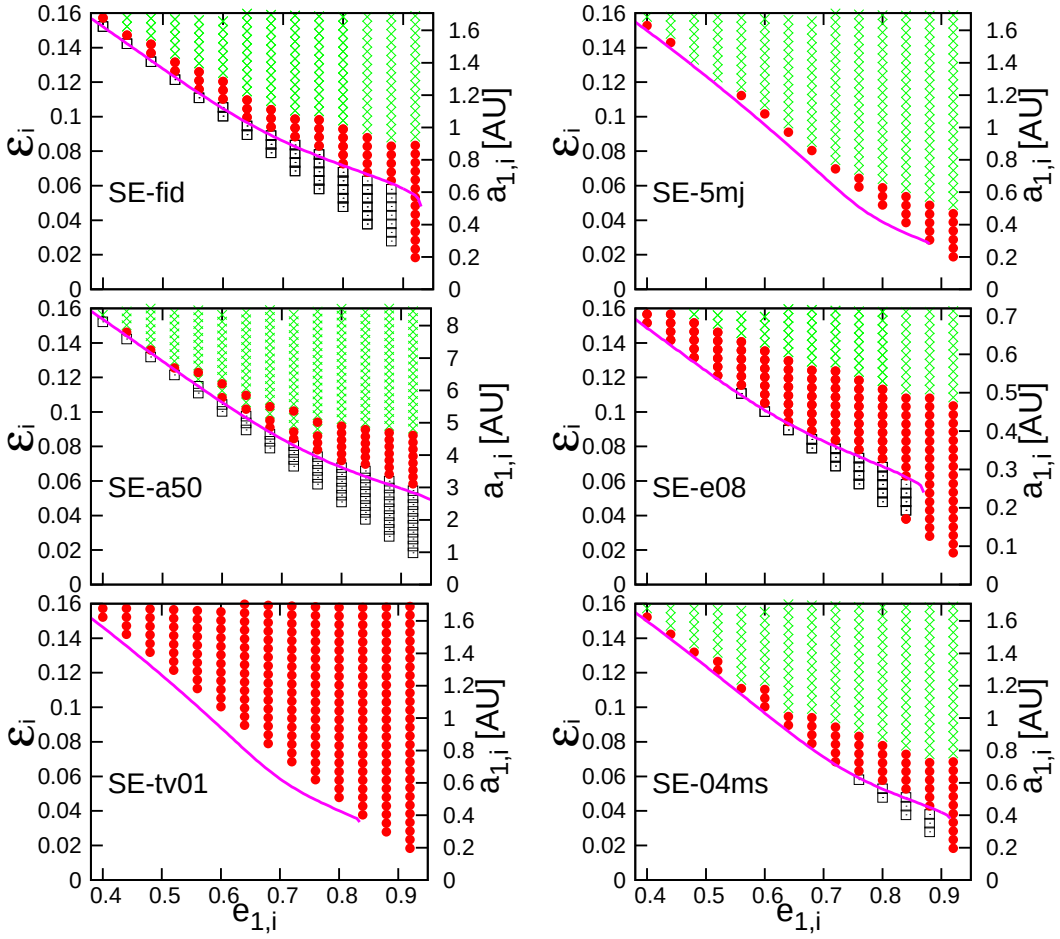

Figure 4.22: Fate of the inner planets on $(e_{1,i}, \epsilon_i)$ plane for six different cases in super-Earth system simulations, SE-fid, SE-5mj, SE-a50, SE-e08, SE-tv01, and SE-04ms. The final states are indicated by black open squares for non-migrating planets (NM), red filled circles for prograde super-Earth (PSE), green crosses for tidally disrupted planets (TD), respectively. The magenta solid lines correspond to the migration boundary $t_{\rm mig,1} = 10^{10}$ yr based on the analytical estimate derived from equation (4.24).

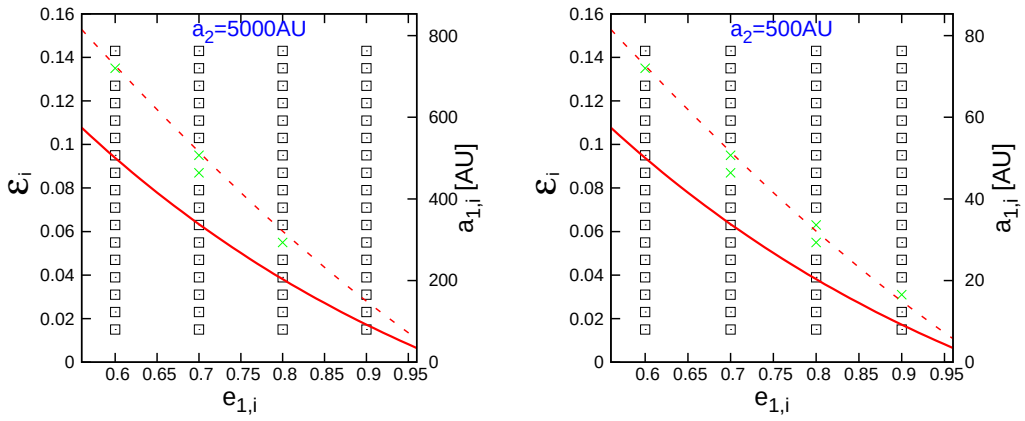

Figure 4.23: Fate of the inner planet on $(e_{1,i}, \epsilon_i)$ plane for triple star systems. The left and right panels refer to $a_2 = 5000$ and 500 AU. The solid and dashed lines correspond to the lower and upper boundaries of the extreme eccentricity condition derived from equation (4.3). The final states are indicated by green crosses for tidally disrupted systems (TD) and black open squares for non-migrating systems (NM).

4.7 Application to Observed Exoplanetary Systems

So far, we have theoretically explored the fate of near-coplanar hierarchical triple systems and their parameter dependence in CHEM, but it has not been clear if this scenario can indeed explain the observed exoplanetary systems. In order to answer this question, we apply CHEM to two distinct groups of the observed exoplanetary systems: hierarchical triple and counter-orbiting HJ systems.

Table 4.4 lists the observed parameters for the systems selected in our simulations. For hierarchical triple systems, we choose three close-in super-Earth systems, Kepler-93, Kepler-97, and Kepler-407 out of 22 Kepler systems in Marcy et al. (2014). In addition, four HJ systems are selected from Knutson et al. (2014). They reported possible outer companions for 14 HJ systems, and four of them, HAT-P-2, HAT-P-4, HAT-P-17, and WASP-22, have $\lambda < 20^\circ$. Note that the true spin-orbit angle is larger than the projected one, λ, as illustrated in the footnote of section 5.1. For simplicity, however, we assume these four systems are well-aligned. Thus, we consider these four systems in our simulations as possible candidates for CHEM. Among the currently known HJ systems with measured λ, two of them are possibly counter-orbiting ($\lambda > 160^\circ$), so we also consider these two systems; HAT-P-6 with $\lambda = 165^\circ \pm 6^\circ$ (Albrecht et al. 2012) and HAT-P-14 with $\lambda = 189^\circ.1 \pm 5^\circ.1$ (Winn et al. 2011).

We fix the values of m_0, m_1, m_2, and a_2 as in Table 4.5 for definiteness. We basically set the eccentricity of the outer perturber, e_2, as 0.6, and consider the dependence on e_2 in the case of Kepler-97 simulations. Following sections 4.3 to 4.5, we adopt initially $i_{12} = 6^\circ$, $\omega_1 = 0^\circ$, $\omega_2 = 0^\circ$, $l_1 = 180^\circ$, $l_2 = 0^\circ$, and $\psi = 0^\circ$ for all the systems. The viscous timescale of the inner planet $t_{\rm v,p}$ is set to 0.03 yr for HJ systems and 0.001 yr for super-Earth systems; the disruption control parameter f is 2.7 for HJ systems and 2.44 for super-Earth systems, respectively. For all systems listed in Table 4.5, we survey $(e_{1,i}, \epsilon_i)$ plane similarly as in the previous sections; $e_{1,i}$ is varied between 0.4 and 0.92 (0.96) with a constant interval of 0.04 (0.02), and ϵ_i is varied between $\epsilon_{\rm L}$ derived from equation (4.3) and 0.15 with a constant interval of 0.005 (0.001) for hierarchical triple systems (counter-orbiting HJ systems).

We aim to examine if those observed systems can be reproduced by CHEM. For hierarchical triple systems, we require that the final semi-major axis of the inner planet, $a_{1,f}$, should be within the observed range. For counter-orbiting HJ systems, we further require that the final spin-orbit angle, $\psi_f > 160^\circ$, in addition to $a_{1,f}$ being within the observed range. Note, however, that the inner planets of HAT-P-2 and HAT-P-17 have finite eccentricities of 0.517 and 0.346, respectively. They are supposed to be still during the tidal circularization stage with a constant inner orbital angular momentum. Therefore, the final semi-major axis of the inner planet after the circularization stage should be $a_{\rm eq} = a_{1,\rm obs}(1 - e_{1,\rm obs}^2)$, which is 0.0494 AU for HAT-P-2, and 0.0776 AU for HAT-P-17, respectively. We require that $a_{1,f}$ should be sufficiently close to $a_{\rm eq}$ for these two systems.

We first focus on Kepler-97, a typical close-in super-Earth system, by running a variety of simulation models with different orbital parameters. This is also useful in understanding

the parameter dependence in general.

4.7.1 Kepler-97

Kepler-97 consists of a sun-like central star, a close-in super-Earth with $a \sim 0.036$ AU in a circular orbit, and a recently detected distant outer perturber. The orbital elements of the outer perturber are not well determined and there are week constraints only; $m_2 > 344 M_\oplus$ and $a_2 > 1.637$ AU (Marcy et al. 2014). Therefore, we consider three sets of parameters for m_2 and a_2, the results of which are plotted in Figure 4.24; $(m_2, a_2) = (1.08 M_{\rm J}, 1.67$ AU), $(2 M_{\rm J}, 2$ AU), and $(10 M_{\rm J}, 10$ AU) from left to right. For each set of parameters, we run simulations with three different values of $e_{2,i}$; $e_{2,i} = 0.4, 0.6$, and 0.8, corresponding to the top, middle, and bottom panels in Figure 4.24.

As before, we run the simulations for $\epsilon_i > \epsilon_{\rm L}$ estimated from equation (4.3). In this region, there are NMs, PSEs and TDs. In Figure 4.24 we plot only PSEs with different colors according to $a_{1,f}$. All the results lead to $a_{1,f} \sim (0.01 - 0.06)$ AU, so we plot the simulations in three colors with black, red, and blue circles for the range of 0.01 AU $< a_{1,f} < a_{1,\rm obs,min}$, $a_{1,\rm obs,min} < a_{1,f} < a_{1,\rm obs,max}$, and $a_{1,\rm obs,max} < a_{1,f} < 0.06$ AU, respectively, where $a_{1,\rm obs,min}$ and $a_{1,\rm obs,max}$ refer to the lower and upper limits in Table 4.4.

As Figure 4.24 indicates, the resulting PSE region becomes narrower as m_2 increases. Nevertheless, the range of $a_{1,f}$ is fairly insensitive to the choice of the orbital parameters. Independently of the orbital parameters, all the sets of simulations reproduce the observed range of $a_{1,f}$, *i.e.*, 0.036 ± 0.007 AU. Therefore we conclude that the current configuration of Kepler-97 can be explained over a wide range of parameters in CHEM.

4.7.2 Other Hierarchical Triple Systems: Kepler-93, Kepler-407, HAT-P-2, HAT-P-4, HAT-P-17, and WASP-22

We repeat the same simulations on $(e_{1,i}, \epsilon_i)$ plane for the other six hierarchical triple systems and the results of $a_{1,f}$ against ϵ_i are plotted in Figure 4.25. Each panel in Figure 4.25 exhibits several distinct sequences, which correspond to the different value of $e_{1,i}$; we plot the observed value of $a_{1.\rm obs}$ in blue solid lines and their lower and upper limits in black dashed lines.

According to our simulations, three of them, Kepler-407, HAT-P-4, and WASP-22 are reproduced in CHEM, but the remaining other three systems, Kepler-93, HAT-P-2, and HAT-P-17 are not; the above three unsuccessful systems lead to $a_{1,f}$ smaller than their current values. As described in subsection 4.4.4, stronger tides are necessary for systems to achieve the larger $a_{1,f}$. The left bottom panel of Figure 4.21 indicates that $a_{1,f}$ increases by $\sim 30\%$ if $t_{\rm v,p}$ is decreases by a factor of 10 from the fiducial value ($t_{\rm v,p} = 0.03$ yr). In order to explain Kepler-93 and HAT-P-17 in the framework of CHEM, 10 times stronger tides are required. Such extreme tides seem to be unrealistic. Therefore, we conclude that those systems are unlikely to result from CHEM.

We find that only 4 out of 7 are possibly reproduced, but the other 3 are difficult. Although the 7 systems we consider here may not represent the fair sample of the hierarchical triple systems, this may imply that CHEM can reproduce a reasonable fraction of close-in prograde planets in the observed hierarchical triple systems, but it is also likely that the other migration processes should operate including the Lidov-Kozai migration and disk migration.

4.7.3 Counter-orbiting HJ Systems: HAT-P-6 and HAT-P-14

In this subsection, we apply CHEM to two counter-orbiting HJ systems, HAT-P-6 and HAT-P-14. Since the possible outer perturbers for these systems are not confirmed, we assume a hypothetical outer perturber in a hierarchical triple configuration and examine if the counter-orbiting HJ can be reproduced in this scenario. Again, we repeat the same simulations on $(e_{1,i}, \epsilon_i)$ plane. The hypothetical perturber we adopt has $a_{2,i} = 1000$ AU, $m_2 = 0.03 M_\odot$, and $e_{2,i} = 0.6$. Although there are a variety of possible configurations for the outer perturber, we follow a set of parameters for a sub-stellar perturber according to section 4.3. In section 4.3, however, we found that the formation of counter-orbiting HJs is difficult for such a configuration. In our simulations, we increase the formation efficiency by adopting less restrictive disruption radius; we use the disruption control factor $f = 2.16$, instead of the fiducial value $f = 2.7$.

The results are shown in Figure 4.26. We plot the distribution of $a_{1,f}$ for RHJs with final spin-orbit angle, $\psi_f > 160^\circ$ and those RHJs on $(e_{1,i}, \epsilon_i)$ plane in the upper and bottom panels for above two systems. We use different colors in the bottom panels according to $a_{1,f}$. The left panels refer to HAT-P-6. In this case, we adopt black for $0.025 < a_{1,f} < 0.035$ AU, red for $0.035 < a_{1,f} < 0.045$ AU, blue for $0.045 < a_{1,f} < 0.055$ AU, and green for $0.055 < a_{1,f} < 0.065$ AU, respectively. While a non-negligible fraction of counter-orbiting HJ systems are produced, only one case satisfies the current observation with $a_{1,i} = 60.2$ AU, $e_{1,i} = 0.84$, and $a_{1,f} = 0.0523$, $\psi_f = 165.1^\circ$. Most of RHJs have $a_{1,f}$ smaller than $a_{1,\rm obs}$. In conclusion, it is difficult to produce counter-orbiting HJ systems that are consistent with the current observation of HAT-P-6.

The right panels are for HAT-P-14. In this case, we choose black for $0.02 < a_{1,f} < 0.025$ AU, red for $0.025 < a_{1,f} < 0.03$ AU, blue for $0.03 < a_{1,f} < 0.035$ AU, and green for $0.035 < a_{1,f} < 0.04$ AU, respectively. The maximum $a_{1,f}$ in the simulations, 0.038 AU, is only $\sim 65\%$ of $a_{1,\rm obs} = 0.0594$ AU. Therefore, it is completely impossible for HAT-P-14 to be reproduced in CHEM.

These results are supposed to be generic regardless of the orbital parameters of the outer perturber, because the range of $a_{1,f}$ is fairly insensitive to them, if we assume the tendency of $a_{1,f}$ in RHJs is similar as in PHJs shown in Figure 4.21. We expect that in general it is very difficult to form counter-orbiting HJs without fine tuning, so we conclude that even CHEM is difficult to explain the observed candidates of counter-orbiting HJ systems. This implies that the observed candidate counter-orbiting HJ systems may be

simply due to the projection effect like HAT-P-7 or another physical mechanism other than CHEM is responsible to produce them. This is still an open question.

4.8 Summary of This Chapter

In this chapter, we have investigated a possibility that HJs form in near-coplanar eccentric hierarchical triple systems via the secular interaction between an inner planet and an outer perturber (Coplanar High-eccentricity Migration, CHEM). Our results are summarized in the following 8 main findings.

1) We generalize the analytic extreme eccentricity condition in purely gravitational interaction that was derived by Li et al. (2014) and Petrovich (2015b) neglecting the mass of the inner planet, m_1, on the dynamics of the central star, m_0. We find that the extreme eccentricity region is significantly limited when the finite mass of m_1 is taken into account. Therefore, the significant migration in CHEM is possible only when $m_1 \ll m_0$ and $m_1 \ll m_2$.

2) We perform a series of numerical simulations in CHEM for systems consisting of a sun-like central star, giant gas inner planet, and sub-stellar outer perturber, including the short-range forces (GR, stellar and planetary non-dissipative tides, and stellar and planetary rotational distortion) and stellar and planetary dissipative tides. We find that most of the near-coplanar hierarchical triple systems that satisfy the analytical extreme eccentricity condition do not produce counter-orbiting planets. Instead, the inner planets in those systems are tidally disrupted. A small fraction of the systems end up with the prograde HJs, and very few retrograde HJs are produced. Systems that do not satisfy the analytical extreme eccentricity condition do not exhibit any significant migration of the inner planet.

3) The break-down of the the analytical extreme eccentricity condition is due to the SRFs, which suppresses the extreme eccentricity evolution of the inner planet that is required for the orbital flip. The results for systems with a sub-stellar perturber are almost independent of the model parameters, and thus fairly generic unless unrealistically strong tidal effect is assumed. The mutual orbital inclination angle between the inner planet and outer perturber, and the spin-orbit angle between the central star and the inner planet are almost the same. Their distribution for the survived HJs is bimodal; $\sim 0^\circ - 20^\circ$ for prograde, and $\sim 160^\circ - 180^\circ$ for retrograde planets, and virtually nothing in-between.

4) We perform a series of similar numerical simulations in CHEM for systems with a planetary outer perturber similarly as the case with a sub-stellar perturber. We find that the overall results is similar with the sub-stellar perturber case, but no retrograde HJ forms (see Figure 4.16). The short-range forces suppress the extreme eccentricity growth, and significantly affect the orbital evolution of the inner planet. These results are fairly independent of the orbital elements of the outer perturber.

5) We present an analytical model that explains the numerical results approximately. We analytically estimate the location when the minimum pericenter distance of the inner

planet, $q_{1,\min}$, reaches the Roche limit, which determines the condition of the inner planet being tidally disrupted. In addition, we provide an analytical estimate of the migration timescale including short-range forces and planetary dissipative tides, which qualitatively explains the result of our numerical simulation. These estimates are useful in interpreting the simulation results.

6) We apply CHEM to super-Earth systems around a sun-like central star with a giant gas planetary outer perturber. As in the giant gas inner planetary case, we find that the majority end up with tidally disrupted planets, but a small fraction is survived as a prograde close-in super-Earth.

7) We apply CHEM to binary systems with a stellar perturber. We find that no close binary forms in CHEM due to weak stellar tides and limited extreme eccentricity region.

8) We apply CHEM to the observed 7 hierarchical triple systems (Kepler-93, Kepler-97, Kepler-407, HAT-P-2, HAT-P-4, HAT-P-17, and WASP-22) and 2 counter-orbiting HJ systems (HAT-P-6 and HAT-P-14). We find that 4 out of 7 hierarchical triple systems (Kepler-93, Kepler-407, HAT-P-4, and WASP-22) are possibly reproduced in CHEM, but the other 3 hierarchical triple systems and 2 counter-orbiting HJ systems are unlikely to be explained in CHEM.

Our simulation runs span the parameter space that satisfy the analytical extreme eccentricity condition, and more importantly uniformly sample the $(e_{1,i}, \epsilon_{1,i})$ plane without assuming any prior distribution for their realistic values. Therefore predicted statistics for the fate of the inner planet under such configurations may be significantly biased. Having emphasized such warnings, however, it might be instructive to present some statistics simply illustrating the difficulty of forming the counter-orbiting planets in the near-coplanar hierarchical triple system.

Figure 4.27 plots the fraction of four different final outcomes of the inner planet for systems with a giant gas inner planet and a sub-stellar perturber; NM (non-migrating planet) in black, PHJ (prograde HJ) in red, RHJ (retrograde HJ) in blue, and TD (tidally disrupted planet) in green. The left panel corresponds to a number fraction of each fate simply from the numbers out of ~ 1800 runs for each model summarized in Table 5.1. The right panel is computed from their sub-sample with $10\text{AU} < a_{1,i} < 30\text{AU}$ so as to sample the $(a_{1,i}, e_{1,i})$ plane assuming the eccentric inner gas giant planets orbiting at reasonable distances from the central star just for the comparison purpose.

Our simulation results for the case of a planetary perturber seems to be slightly different from the case of a sub-stellar perturber. Indeed, very small fraction can end up with retrograde HJs for a sub-stellar perturber. This is simply because of the initial semi-major axis of the inner planet, $a_{1,i}$. The range of $a_{1,i}$ is very different in the two models; we consider $0.3 < a_{1,i} < 8$ AU for a perturber planetary , but $3 < a_{1,i} < 80$ AU for a sub-stellar perturber. In the former case, the inner planet suffers from tidal circularization before acquiring the required extreme eccentricity for the orbital flip, and therefore, no retrograde HJ forms in a planetary perturber.

In any case, our basic conclusion remains the same even if the statistics shown here

just for example may be highly biased; CHEM can produce some fraction of close-in prograde planets, but no retrograde one.

In this chapter, we have systematically studied the CHEM for the formation of HJ till the tidal circularization. In reality, the later evolution due to the tides on the central star after the formation stage also significantly affects the spin and orbital evolution of HJs. In particular, tides continuously modify the spin-orbit angle in a secular timescale as described in section 2.5. These valuable topics will be discussed in detail in the next chapter.

Table 4.4: Orbital parameters of selected hierarchical triple and candidate counter-orbiting HJ systems.

	m_0 $M_\odot$	m_1	m_2	a_1 AU	a_2 AU	e_1	λ	Ref.
Hierarchical triple								
Kepler-97	0.94 ± 0.06	$3.5 \pm 1.9 M_\oplus$	$> 344 M_\oplus$	0.036 ± 0.007	> 1.637	0.0	...	1
Kepler-93	0.91 ± 0.06	$2.59 \pm 2.0 M_\oplus$	$> 954 M_\oplus$	0.053 ± 0.007	> 2.441	0.0	...	1
Kepler-407	1.0 ± 0.06	$< 3.1999 M_\oplus$	$4000 \pm 2000 M_\oplus$	0.01497 ± 0.0003	$4.068^{+0.441}_{-0.466}$	0.0	...	1
HAT-P-2	1.34 ± 0.09	$8.74 \pm 0.26 M_\mathrm{J}$	$8 - 200 M_\mathrm{J}$	0.0674 ± 0.00081	4-31	0.517 ± 0.0033	$9° \pm 13.4°$	2,3
HAT-P-4	1.26 ± 0.14	$0.68 \pm 0.04 M_\mathrm{J}$	$1.5 - 310 M_\mathrm{J}$	0.0446 ± 0.0012	5-60	0.0	$-4.9° \pm 11.9°$	2,4
HAT-P-17	0.857 ± 0.039	$0.534 \pm 0.018 M_\mathrm{J}$	$2.8 - 3.7 M_\mathrm{J}$	0.0882 ± 0.00147	4.7-8.3	0.346 ± 0.007	$19°^{+14.°}_{-16.°}$	2,5
WASP-22	1.1 ± 0.3	$0.56 \pm 0.103 M_\mathrm{J}$	$7 - 500 M_\mathrm{J}$	0.04698 ± 0.00037	6-40	0.0	$22° \pm 1$	2,6
Counter-orbiting HJs								
HAT-P-6	1.29 ± 0.06	$1.057 \pm 0.119 M_\mathrm{J}$	...	0.05235 ± 0.00087	...	0.0	$165° \pm 6$	7
HAT-P-14	1.386 ± 0.045	$2.2 \pm 0.04 M_\mathrm{J}$	...	0.0594 ± 0.0004	...	0.0	$189.1° \pm 3.1°$	8

Note. The observations reported at http://exoplanet.org include data from the references as follows: (1) Marcy et al. (2014); (2) Knutson et al. (2014); (3)Pal et al. (2010); (4) Kovacs et al. (2007); (5) Howard et al. (2012); (6)Maxted et al. (2010); (7) Noyes et al. (2010); (8) Torres et al. (2010).

Table 4.5: Orbital parameters of hierarchal triple and counter-orbiting HJ systems in our simulations.

	m_0 $M_\odot$	m_1	m_2	a_2 AU	e_2	Y/N
Hierarchical triple						
Kepler-97v1	$0.94M_\odot$	$3.5M_\oplus$	$344M_\oplus$	1.637	0.4,0.6,0.8	$\surd$
Kepler-97v2	$0.94M_\odot$	$3.5M_\oplus$	$2M_\mathrm{J}$	2	0.4,0.6,0.8	$\surd$
Kepler-97v3	$0.94M_\odot$	$3.5M_\oplus$	$10M_\mathrm{J}$	10	0.4,0.6,0.8	$\surd$
Kepler-93	$0.91M_\odot$	$2.59M_\oplus$	$954M_\oplus$	2.441	0.6	$\times$
Kepler-407	$1.0M_\odot$	$1.0M_\oplus$	$4000M_\oplus$	4.068	0.6	$\surd$
HAT-P-2	$1.34M_\odot$	$8.74M_\mathrm{J}$	$60M_\mathrm{J}$	5	0.6	$\times$
HAT-P-4	$1.26M_\odot$	$0.68M_\mathrm{J}$	$100M_\mathrm{J}$	30	0.6	$\surd$
HAT-P-17	$0.857M_\odot$	$0.534M_\mathrm{J}$	$3.3M_\mathrm{J}$	6.5	0.6	$\times$
WASP-22	$1.1M_\odot$	$0.56M_\mathrm{J}$	$30M_\mathrm{J}$	12	0.6	$\surd$
Counter-orbiting HJs						
HAT-P-6	$1.29M_\odot$	$1.057M_\mathrm{J}$	$0.03M_\odot$	1000	0.6	$\surd$
HAT-P-14	$1.386M_\odot$	$2.2M_\mathrm{J}$	$0.03M_\odot$	1000	0.6	$\times$

Note. m_0, m_1, m_2, and a_2 are fixed to be consistent with Table 4.4. e_2 is basically set to 0.6, and varied to 0.4 and 0.8 in Kepler-97 simulations to see the parameter dependence. The column Y/N indicates if the observed range can be recovered by the simulations or not with symbols $\surd$ and $\times$.

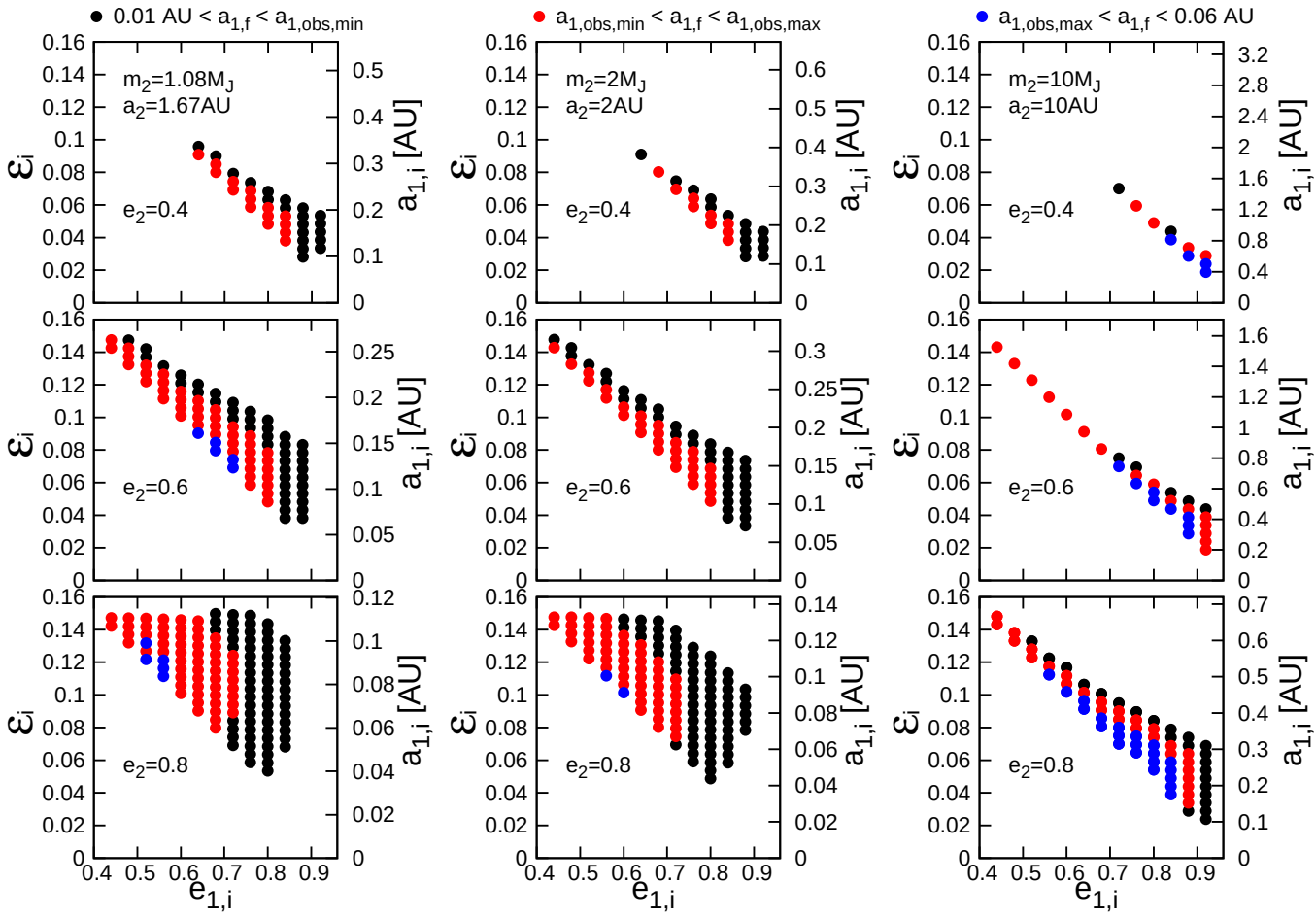

Figure 4.24: Resulting prograde super-Earths of Kepler-97 simulations on $(e_{1,i}, \epsilon_i)$ plane. Different colors correspond to different range of $a_{1,f}$ with black 0.01 AU $< a_{1,f} <$ $a_{1,\mathrm{obs,min}}$, red $a_{1,\mathrm{obs,min}} < a_{1,f} < a_{1,\mathrm{obs,max}}$, and blue $a_{1,\mathrm{obs,max}} < a_{1,f} <$ 0.06 AU, respectively, where $a_{1,\mathrm{obs,min}}$ and $a_{1,\mathrm{obs,max}}$ refer to the lower and upper limits in Table 4.4. All the models adopt $m_0 = 0.94 M_\odot$, $m_1 = 3.5 M_\oplus$, $i_{12,i} = 6°$, $\psi_i = 0°$, $t_{\mathrm{v,p}} = 0.001$ yr, and $f = 2.44$, respectively. The initial values of m_2 and a_2 are $(m_2, a_2) = (1.08 M_\mathrm{J}, 1.67$ AU), $(2 M_\mathrm{J}, 2$ AU), and $(10 M_\mathrm{J}, 10$ AU) from left to right, respectively. The initial value of e_2 is 0.4, 0.6, 0.8, from top to bottom, respectively.

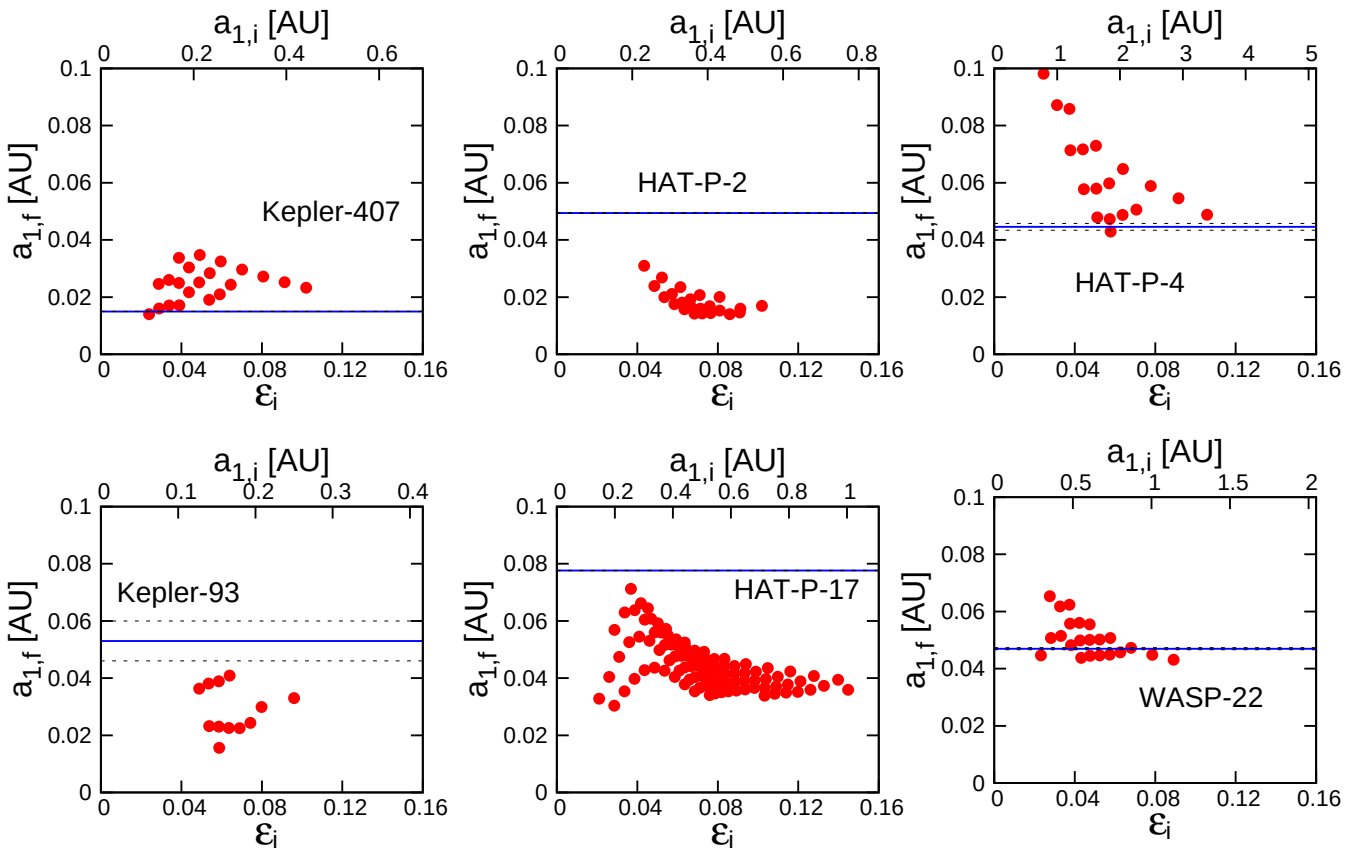

Figure 4.25: Final semi-major axis of resulting PHJs, $a_{1,f}$, for Kepler-93, Kepler-407, HAT-P-2, HAT-P-4, HAT-P-17, and WASP-22 simulations against ϵ_i. For each panel, the observed value, $a_{1,\mathrm{obs}}$, is plotted in the blue solid line and its lower and upper limits are shown in black dashed lines. All the models adopt $e_{2,i} = 0.6$, $i_{12} = 6°$, $\psi_i = 0°$.

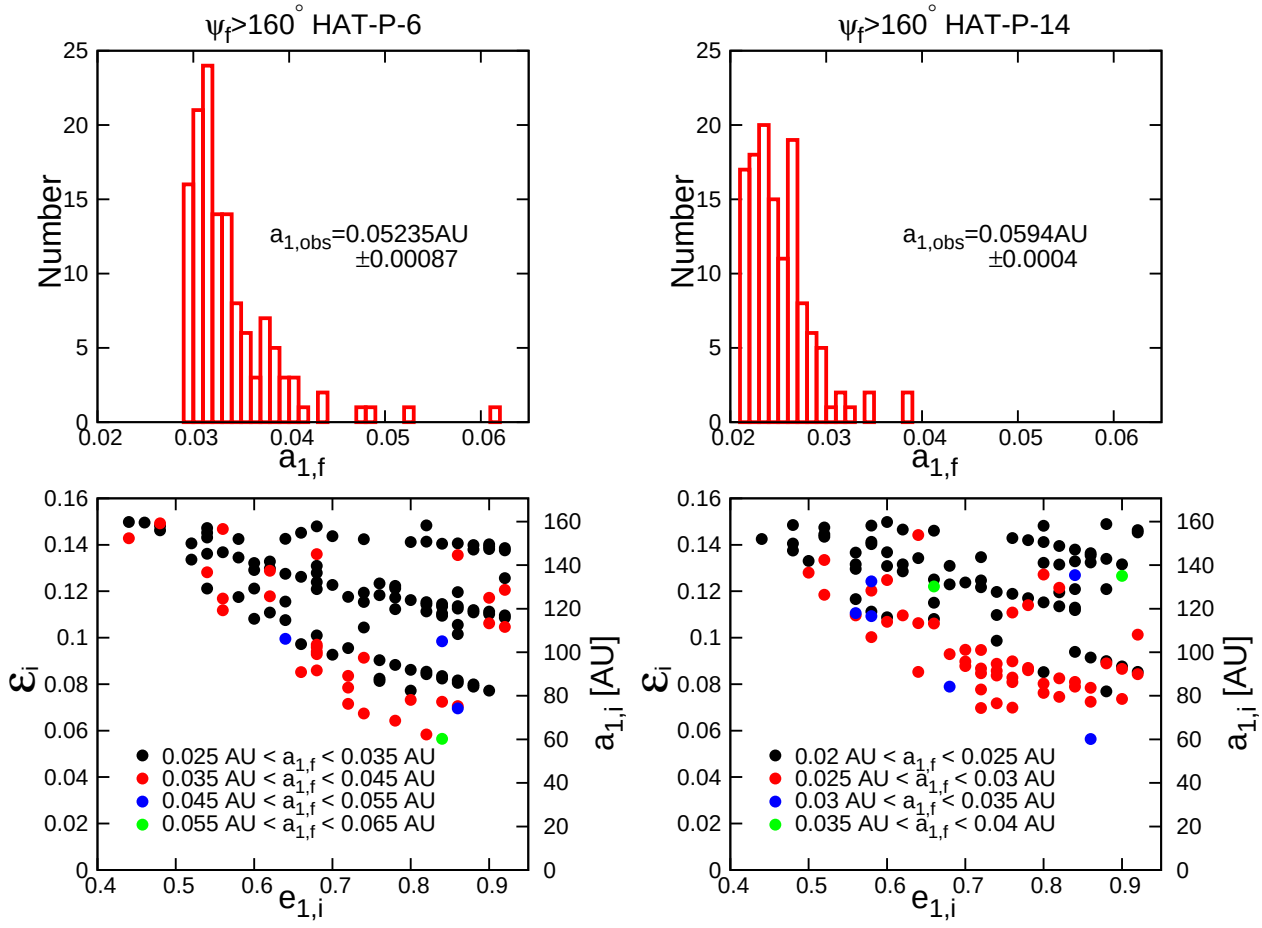

Figure 4.26: Distribution of $a_{1,f}$ for resulting RHJs with $\psi > 160°$ in HAT-P-6 and HAT-P-14 simulations (*upper*) and those RHJs on $(e_{1,i}, \epsilon_i)$ plane (*bottom*). Different colors correspond to different $a_{1,f}$. All the models adopt $m_2 = 0.03 M_\odot$, $a_2 = 1000$ AU, $e_{2,i} = 0.6$, $i_{12,i} = 6°$, $\psi_i = 0°$, $t_{\rm v,p} = 0.03$ yr, and $f = 2.16$, respectively. Left: HAT-P-6 with black $0.025 < a_{1,f} < 0.035$ AU, red $0.035 < a_{1,f} < 0.045$ AU, blue $0.045 < a_{1,f} < 0.055$ AU, and green $0.055 < a_{1,f} < 0.065$ AU, respectively; Right: HAT-P-14 with black $0.02 < a_{1,f} < 0.025$ AU, red $0.025 < a_{1,f} < 0.03$ AU, blue $0.03 < a_{1,f} < 0.035$ AU, and green $0.035 < a_{1,f} < 0.04$ AU, respectively.

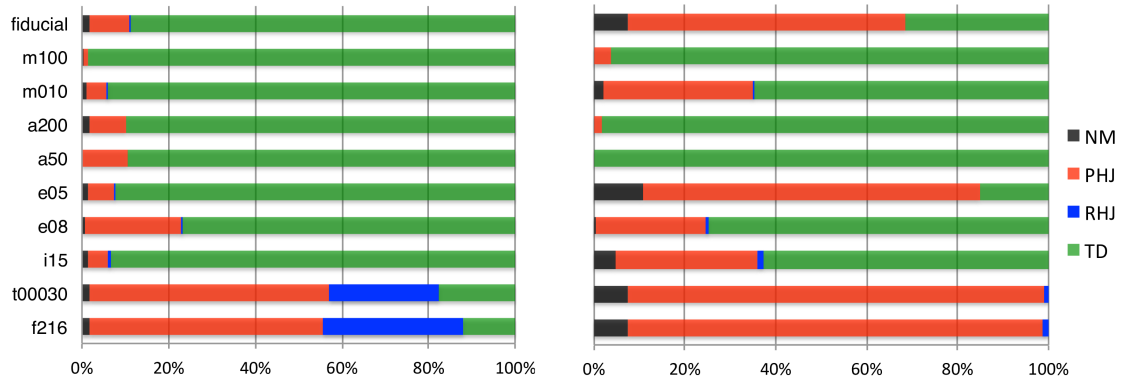

Figure 4.27: The fraction of the for different outcomes of the inner planets with a sub-stellar perturber. Left panel: All simulations. Right panel: 10AU $< a_{1,i} <$ 30AU. We plot NM (non-migrating planet) in black, PHJ (prograde HJ)) in red, RHJ (retrograde HJ) in blue, and TD (tidally disrupted planet) in green, respectively.

Chapter 5

Spin-orbit Angle Realignment: the Lai Model

5.1 Introduction

So far, we have examined the formation stage of HJs in CHEM in chapter 4, but later tidal evolution of HJs (realignment stage) is not included. As discussed in section 2.5, after tidal circularization, tides on the central star modify HJ systems in a secular timescale. In particular, they affect the spin-orbit angle for a misaligned system. The spin-orbit angle distribution is a useful discriminator of the HJ migration mechanisms. In order to properly compare the simulations with the observation, the realignment stage should be carefully taken into account, but its detailed model is still unknown.

As explained by subsection 2.5.2, the conventional equilibrium tide model can realign the system, but inevitably accompanies the orbital decay of the planet within a similar timescale (Barker & Ogilvie 2009; Levrard et al. 2009; Matsumura et al. 2010); see equation (3.57). Therefore a simple equilibrium tide model does not explain the majority of the realigned systems with finite semi-major axis. Recently, Lai (2012) proposed a new model to overcome the equilibrium tide problem, in which the damping timescale of the spin-orbit angle could be significantly smaller than that of the planetary orbit.

In this chapter, we use a full set of equations to trace the three-dimensional orbit of a planet (we assume that this represents the innermost planet in the case of multi-planetary systems) and the spin vector of the central star simultaneously, and examine the tidal evolution of exoplanetary systems on a secular timescale. We present a detailed comparison with the previous results by Rogers & Lin (2013), and argue that the full set of equations is important in understanding the long term evolution of the tidal model.

We briefly review the two tidal models, the equilibrium tide and the inertial wave dissipation, in section 5.2, and describe how to combine the two models in our treatment. The basic set of equations is summarized explicitly in section 3.3 and Appendix D. After comparing with the previous result in subsection 5.3.1, we present the evolution in the

combined tidal model in subsection 5.3.2. We also consider there the dependence on the fairly uncertain parameters of the model. Section 5.4 is devoted to summary and discusses implications of the present result. This chapter is based on Xue et al. (2014).

5.2 Tidal Evolution of Star–HJ Systems

The entire dynamical evolution of planetary systems has many unresolved aspects including the initial structure of proto-planetary disks, formation of proto-planets, planetary migration, planet-planet gravitational scattering, and the tidal interaction between the central star and orbiting planets. It is definitely beyond the scope of the present thesis to consider such complicated processes in a self-consistent fashion. Thus we consider a very simple system comprising a star and a HJ, and focus on their tidal interaction in order to examine the dynamical behavior of the stellar spin and the planetary orbit. Just for definiteness, we fix the mass and radius of the star and the planet as $m_{\rm s} = 1M_{\odot}$, $m_{\rm p} = 10^{-3}M_{\odot}$, and $R_{\rm s} = 1R_{\odot}$. The initial semi-major axis of the planetary orbit is set as $a_i = 0.02$AU.

We do not assume any specific formation mechanism, but the above configuration is expected generically from any successful models for HJs formation. The eccentricity and inclination of the HJs would depend on the details of the formation mechanism. The present study, however, focuses on the tidal evolution between the star and the HJ after the orbit circularization. Then we set the eccentricity of the planet to zero, and consider a wide range of the initial inclination of its orbit with respect to the spin axis of the star.

The fact that a number of well-aligned HJs survive at a finite distance from the star challenges the equilibrium tide model (ET model, hereafter) due to its single timescale. Therefore, one need to refine the ET model to explain the current observation. One possible channel proposed by Winn et al. (2010) is a decoupling model in which the stellar convective envelope is weakly coupled to its radiative core. Thus the convective envelop could aligned with the orbit in a much shorter timescale. Another promising model that we examine in detail below is proposed by Lai (2012), who studied the importance of the inertial waves of the star driven by the Coriolis force and dissipation in the star for the misaligned orbital angular momentum $\mathbf{G}$ and stellar spin angular momentum $\mathbf{L}$. The basic equations are summarized in section 3.3 and Appendix D.

We numerically integrate the set of equations shown in Appendix D for the ET model. For the Lai model, we modify the equations by adding the tidal torque $\mathbf{T}_{10}$ in section 3.3 as

$$\dot{\mathbf{L}} = \dot{\mathbf{L}}_{(\rm e)} + \mathbf{T}_{10} - \mathbf{T}_{10,\rm e}, \tag{5.1}$$

$$\dot{\mathbf{G}} = \dot{\mathbf{G}}_{(\rm e)} - \mathbf{T}_{10} + \mathbf{T}_{10,\rm e}, \tag{5.2}$$

where the subscript (e) indicates the terms for the ET model, and $\mathbf{T}_{10,\rm e}$ is the term that

Parameter	symbol	Star	HJ
mass	$m[M_\odot]$	1	10^{-3}
radius	$R[R_\odot]$	1	—
Love number	k_2	0.028	—
tidal delay time	$\Delta t_{\rm L}$[sec]	0.1	—
principal moment of inertia	C/mR^2	0.08	—

Table 5.1: Fiducial values of the parameters adopted in our simulations.

is introduced to avoid the double counting in the above equations:

$$\frac{\mathbf{T}_{10,\rm e}}{\mathbf{T}_{10}} = \left(\frac{Q_{10}}{Q_{\rm e}}\right)\left(\frac{k_2}{k_{10}}\right). \tag{5.3}$$

The value of $\tau_{10}/\tau_{\rm e}$, however, is difficult to estimate in a reliable fashion. Thus we assume a fiducial value of 10^{-3} at the start of our simulation following Rogers & Lin (2013), and examine the dependence in subsection 5.3.2. Table 5.1 summarizes the fiducial values that we employ in the simulations. We use the same values for the stellar principal moment of inertia, the Love number and the tidal delay time that were adopted by Correia et al. (2011) for $\sim 1M_\odot$ star.

5.3 Numerical Results

5.3.1 Comparison with Previous Results

Before presenting a detailed analysis of the Lai model, we compare typical results arising from different tidal models and approximations. We consider two different tidal models: the ET model and the Lai model. Unlike in Rogers & Lin (2013), we refer to the Lai model which incorporates both the equilibrium tide and the inertial wave dissipation effects.

We numerically integrate the full set of equations (5.1) and (5.2) throughout this chapter. If one focuses on the evolution for a, $\Omega_{\rm s}$, and ψ, the evolution equations in the Lai model can be reduced as follows:

$$\dot{a} = (\dot{a})_{\rm e}, \tag{5.4}$$
$$\dot{\Omega}_{\rm s} = (\dot{\Omega}_{\rm s})_{\rm e} + (\dot{\Omega}_{\rm s})_{10} - (\dot{\Omega}_{\rm s})_{10,\rm e}, \tag{5.5}$$
$$\dot{\psi} = (\dot{\psi})_{\rm e} + (\dot{\psi})_{10} - (\dot{\psi})_{10,\rm e}, \tag{5.6}$$

where

$$\frac{(\dot{\Omega}_{\rm s})_{10,\rm e}}{(\dot{\Omega}_{\rm s})_{10}} = \frac{(\dot{\psi})_{10,\rm e}}{(\dot{\psi})_{10}} = \left(\frac{Q_{10}}{Q_{\rm e}}\right)\left(\frac{k_2}{k_{10}}\right). \tag{5.7}$$

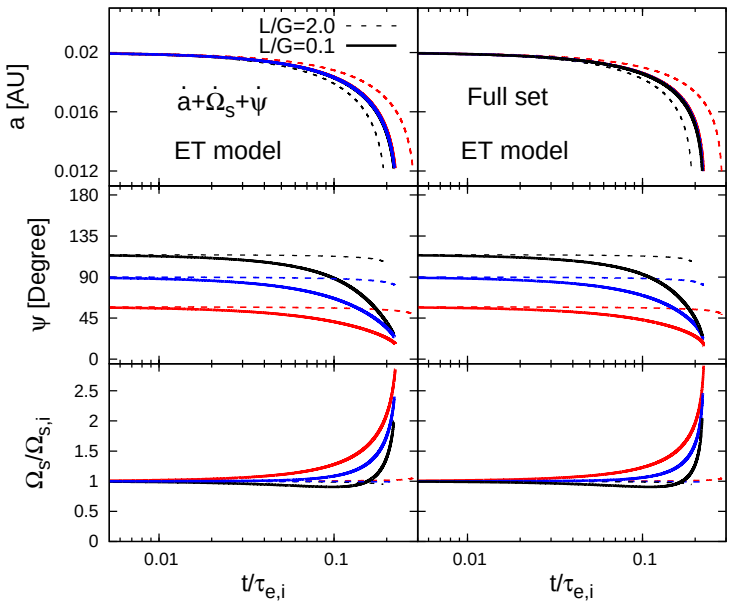

Figure 5.1: Evolution of the semi-major axis (*Top*), the spin-orbit angle (*Center*), and the spin angular frequency (*Bottom*) in the equilibrium tide model. Left and right panels are based on the numerical integration of the simplified and full sets of equations explained in the text. The three different initial spin-orbit angles are assumed; prograde ($\psi_i = 58°$), polar ($\psi_i = 90°$), and retrograde ($\psi_i = 116°$) orbits, shown in red, blue, and black, respectively. The solid and dashed lines indicate the $(L/G)_i = 0.1$ (solid) and 2 (dashed).

In order to compare with the results from the full set of equations, we also integrate the above set of equations assuming the constant value for $(Q_{10}/Q_{\rm e})(k_2/k_{10})$. In practice, we use equation (3.67), and fix its value from the initial values of $\tau_{10}/\tau_{\rm e}$ and L/G:

$$\frac{Q_{10}}{Q_{\rm e}}\frac{k_2}{k_{10}} = \frac{1}{4}\left(\frac{\tau_{10}}{\tau_{\rm e}}\right)_i \left(\frac{L}{G}\right)_i^{-1}. \tag{5.8}$$

In the above simplified set of equations, $m_{\rm s}$ and $m_{\rm p}$ do not show up explicitly, but implicitly in τ_{10}, $\tau_{\rm e}$, and $I_{\rm s}$. For definiteness, we fix $I_s = 0.08 m_{\rm s} R_{\rm s}^2$ (Correia et al. 2011; Wu & Murray 2003). Thus L/G and $\Omega_{\rm s}/\Omega_{\rm p}$ are related to each other as

$$\frac{\Omega_{\rm s}}{\Omega_{\rm p}} \approx 0.23 \left(\frac{M_\odot}{m_{\rm s}}\right)\left(\frac{m_{\rm p}}{10^{-3}M_\odot}\right)\left(\frac{R_\odot}{R_{\rm s}}\right)^2\left(\frac{a}{0.02{\rm AU}}\right)^2\left(\frac{L}{G}\right). \tag{5.9}$$

Figure 5.1 shows evolution of a (*Upper* panels), ψ (*Center*), and $\Omega_{\rm s}/\Omega_{\rm s,i}$ (*Lower*) for the ET model. Left and right panels plot the results on the basis of the simplified set of equations for a, $\Omega_{\rm s}$ and ψ (eqs.(3.54) – (3.56)) and the full equations in Appendix D, respectively. Note that $\tau_{\rm e}$ completely specifies the units of time in the simulations. Thus

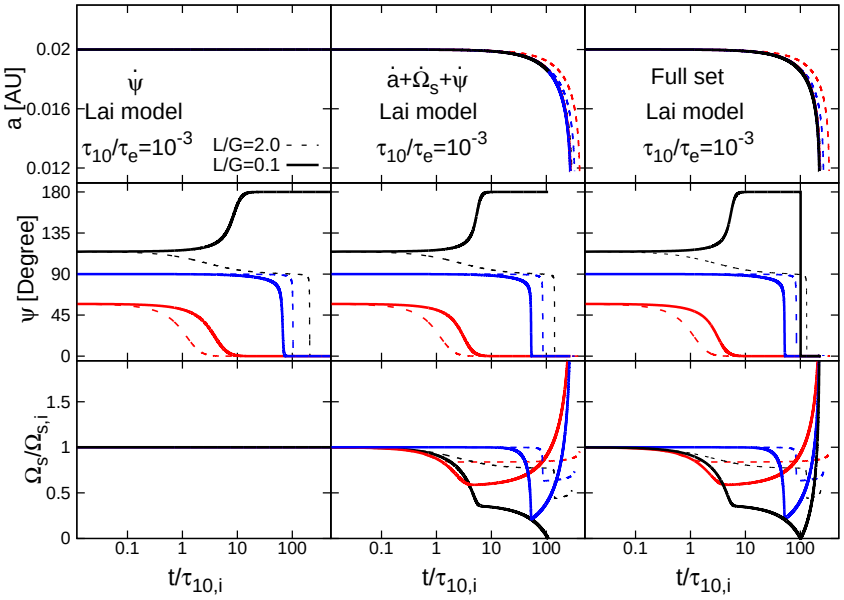

Figure 5.2: Same as Figure 5.1 but for the Lai model that combines the equilibrium tide and the inertial wave dissipation effects simultaneously. We add left panels that correspond to the result neglecting the change of a and $\Omega_{\rm s}$.

the time evolution is scaled with respect to the initial value of $\tau_{\rm e}$. This is why those panels are plotted against $t/\tau_{\rm e,i}$.

In each panel, we start the models with three different initial spin-orbit angles; prograde ($\psi_i = 58°$), polar ($\psi_i = 90°$), and retrograde ($\psi_i = 116°$). They are shown in red, blue, and black lines, respectively. For each initial condition, we plot two cases with the $(L/G)_i = 0.1$ (solid) and 2 (dashed) roughly corresponding to the upper and lower limits of L/G for planets observed via the RM effect (Rogers & Lin 2013). We note here that the system evolved towards $\psi = 0$ regardless of ψ_i.

As pointed out earlier by several authors, the spin-orbit alignment occurs almost simultaneously with the planetary orbital decay. More strictly, equations (3.54) and (3.56) indicate that the damping timescales of the orbit and the spin-orbit angle are given by $\tau_{\rm e}$ and $(L/G)\tau_{\rm e}$, respectively. This explains the dependence on $(L/G)_i$ in the plots (compare solid and dashed lines).

The situation changes drastically in the Lai model, which introduces an additional timescale τ_{10}. Figure 5.2 shows an example of $(\tau_{10}/\tau_{\rm e})_i = 10^{-3}$. In this case, the orbital decay proceeds according to the timescale of $\tau_{\rm e}$, while the alignment timescale is controlled by τ_{10} as well as $(L/G)\tau_{\rm e}$. Thus if $\tau_{10} \ll \tau_{\rm e}$, one can neglect the change of a during the spin-orbit evolution. This is the approximation adopted by Rogers & Lin (2013), which corresponds to the left panels of Figure 5.2; we numerically integrate equation (5.6) neglecting the time evolution of a and Ω_s.

Rogers & Lin (2013) found that the system has three distinct stable configurations, *i.e.*, anti-parallel ($\psi = \pi$), polar ($\pi/2$), and parallel (0) orbits, which is easily expected from the right-hand-side of equation (5.6) as well. Nevertheless the damping on the order of $\tau_{\rm e}$ shows up in the later stage, and the polar orbit evolves towards $\psi = 0$. This can be hardly recognized in Figure 2 of Rogers & Lin (2013) because we suspect they stop the integration at $t = 100\tau_{10} = 0.1\tau_{\rm e}$, before their approximation $\dot{a} = 0$ becomes invalid.

In reality, the evolution beyond the epoch should be computed taking account of the change of a and $\Omega_{\rm s}$ properly. The middle panels show the result, and confirm that the polar orbit is a metastable configuration. Since the right-hand-sides of both equations (3.56) and (5.6) are proportional to $\sin\psi$, the system should evolve eventually towards either $\psi = 0$ or π, but not $\pi/2$.

We found that the $\psi = \pi$ configuration finally approaches $\psi = 0$ by integrating the full set of equations for the three dimensional planetary orbit. In the anti-parallel case, the spin-orbit angle has a sharp change between π and 0. This is because as the orbit damps, the stellar spin L continuously decreases according to the total angular momentum conservation. At some point, therefore, the stellar spin becomes 0, changes the direction, and then starts to increase (aligned to the orbital axis). Thus the really stable configuration is $\psi = 0$ alone. Nevertheless the duration of such meta-stable configurations is also sensitive to the choice of $\tau_{10}/\tau_{\rm e}$ and/or $(L/G)_i$; see Figure 5.4. Thus the retro-grade and polar-orbit systems can be observed in the real systems depending on their age.

This behavior cannot be traced properly by the simplified approach, which is based on the differential equation for ψ, combining equations (3.56) and (3.66); the right-hand-side of equations (3.56) diverges at $L = 0$ or $\Omega_s = 0$, and cannot be numerically integrated beyond the point. In contrast, the full set of equations in Appendix D computes $\mathbf{L}$ and $\mathbf{G}$ first, and ψ later. Thus one can compute the evolution continuously beyond $\mathbf{L} = 0$. This is one of the advantages of using the full set of equations even in the case of the simple star-planet system.

In any case, we confirm the original claim of Lai (2012) that one can have an aligned system with a finite semi-major axis as long as $\tau_{10}/\tau_{\rm e} \ll 1$ is satisfied.

5.3.2 Spin-orbit Angle Evolution in the Lai Model

Now we examine the Lai model more systematically using the full set of equations. We run 30 models of a planet with a regularly spaced ψ_i between 0° and 180°. We plot the results in Figure 5.3 for $(L/G)_i = 2$ (left), 0.5 (middle), and 0.1 (right). All the simulations adopt $(\tau_{10}/\tau_{\rm e})_i = 10^{-3}$ so as to compare the middle panels of Figure 2 of Rogers & Lin (2013).

As explained in subsection 5.3.1, the system first approaches parallel, polar, or anti-parallel orbits within a timescale of τ_{10}. They are plotted in black, blue, and red, respectively, so that they are easily distinguished visually. Next the polar, and subsequently anti-parallel orbits, approach towards the parallel orbits in a timescale of $\tau_{\rm e}$, eventually

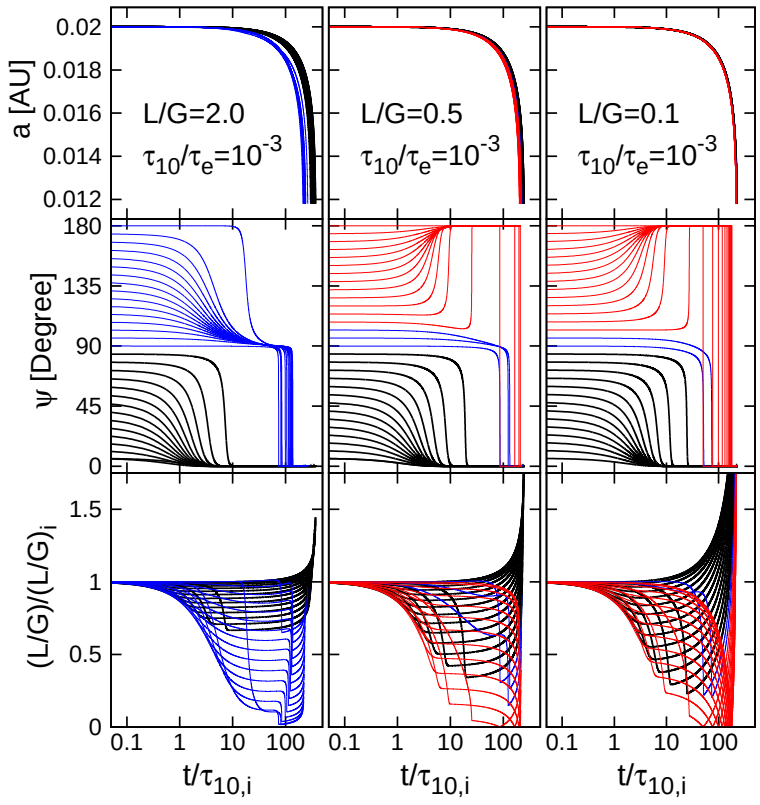

Figure 5.3: Evolution of the semi-major axis (*Top*), the spin-orbit angle (*Middle*), and L/G (*Bottom*) in the Lai model for 30 systems with ψ_i from 0° to 180° with interval 6°. *Left*, *center*, and *right* panels indicate $(L/G)_i = 2$, 0.5, and 0.1, respectively. The $(\tau_{10}/\tau_{\rm e})_i = 10^{-3}$ is assumed. Blue and red lines indicate the systems that show the transition from polar to parallel, anti-parallel to parallel states, respectively.

falling below the Roche limit of the star (0.012 AU in the present case), where we stop the simulations.

The transition from $\psi = 180°$ to 0° (red curves) happens through a state of $\Omega_{\rm s} = 0$, implying that the stellar spin starts counter-rotating due to the tidal effect of the orbiting planet. As mentioned in subsection 5.3.1, the evolution beyond $\Omega_{\rm s} = 0$ is difficult to trace with the simplified set of equations. Thus our simulations on the basis of the full set of equations are essential. Note that the transition to the three meta-stable configurations is fairly rapid. Therefore if the age of the system is larger than τ_{10} and smaller than $\tau_{\rm e}$, one may expect basically three distinct spin-orbit angles, but their broad distribution as observed (*c.f.,* Figure 2.3) is not likely to be explained even taking into account the projection effect; see Figure 3 of Rogers & Lin (2013).

While Figure 5.3 is the main result of this chapter, it remains to consider the dependence on the initial ratios of $(\tau_{10}/\tau_{\rm e})_i$, and $(\Omega_{\rm s}/\Omega_{\rm p})_i$. As we will show below, the behavior

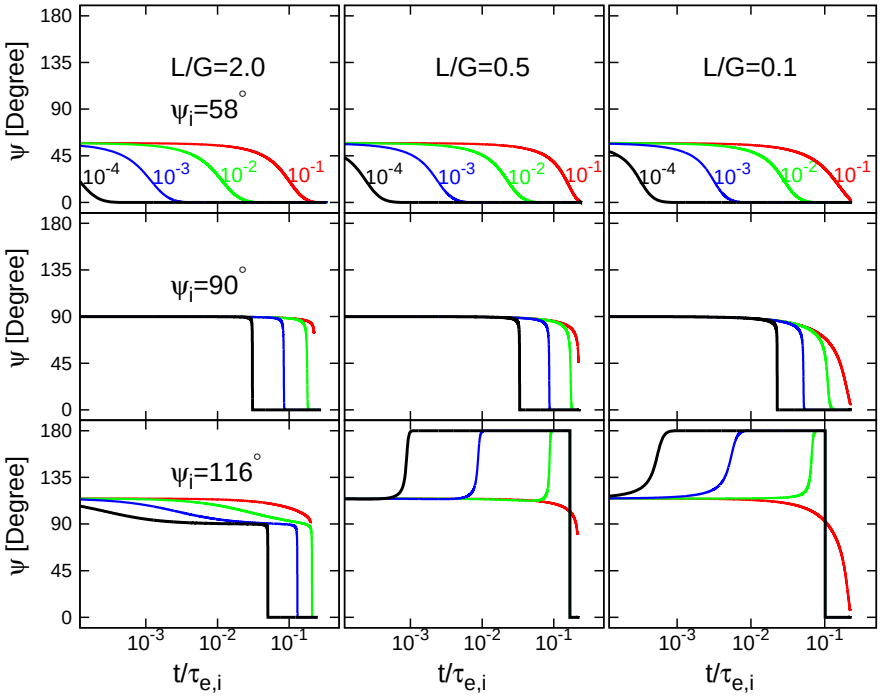

Figure 5.4: Dependence on the tidal dissipation parameter $(\tau_{10}/\tau_{\rm e})_i$ for $(L/G)_i = 2.0$ (*Left*), 0.5 (*Middle*), 0.1 (*Right*). Black, Blue, Green, Red line represent $(\tau_{10}/\tau_{\rm e})_i = 10^{-4}, 10^{-3}, 10^{-2}, 10^{-1}$; *Top*, *center*, and *bottom* panels indicate initially prograde, polar, and retrograde orbits, respectively.

presented in Figure 5.3 is indeed robust against the choice of those parameters.

Figure 5.4 shows results of initially prograde (*Top*), polar (*Center*), and retrograde (*Bottom*), orbits with $(L/G)_i = 2.0$, 0.5, and 0.1 for $(\tau_{10}/\tau_{\rm e})_i = 10^{-4}$ (black), 10^{-3} (blue), 10^{-2} (green), and 10^{-1} (red). The ratio $\tau_{10}/\tau_{\rm e}$ reflects the property of the stellar fluid itself, and thus is not easy to predict in a reliable fashion. Therefore we consider a fairly wide range of its possible value. The initially prograde cases approach $\psi = 0$ with a timescale of τ_{10} fairly clearly. The initially polar-orbit cases stay the configuration for a significantly longer period than τ_{10}, but eventually approach $\psi = 0$. The initially retrograde cases are somewhat intermediate between the two. In any case, the behavior changes systematically with the value of $(\tau_{10}/\tau_{\rm e})_i$ and can be interpolated/extrapolated relatively easily from Figure 5.4.

Figure 5.5 shows the dependence on the planet mass $m_{\rm p}$, or equivalently on $(\Omega_{\rm s}/\Omega_{\rm p})_i$ through equation (5.9). Since our simulations adopt $m_{\rm s} = 1M_\odot$, $R_{\rm s} = 1R_\odot$, and $m_{\rm p} = 10^{-3}M_\odot$, equation (5.9) determines the value of $\Omega_{\rm s}/\Omega_{\rm p}$ uniquely through $(L/G)_i$. In contrast, Rogers & Lin (2013) vary the value randomly in the range of $0.1 < (\Omega_{\rm s}/\Omega_{\rm p})_i < 10$, while they do not describe exactly how. Equation (5.9) implies that the corresponding values of $(\Omega_{\rm s}/\Omega_{\rm p})_i$ in our model with $m_{\rm p} = 10^{-3}M_\odot$ are 0.46, 0.11, and 0.02 for $(L/G)_i = 2$,

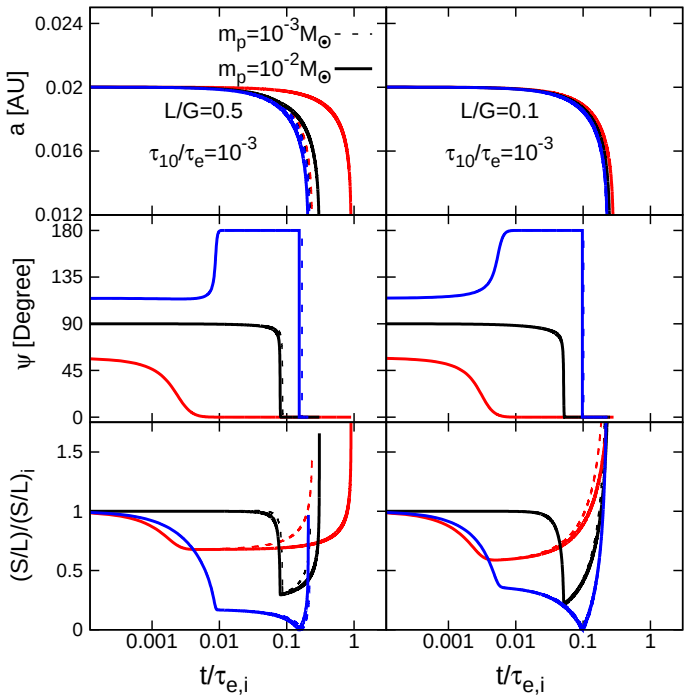

Figure 5.5: Dependence on the planet mass $m_{\rm p}$, or equivalently on $(\Omega_{\rm s}/\Omega_{\rm p})_i$, for $(L/G)_i = 0.5$ (*Left*), 0.1 (*Right*). The blue, black and red lines correspond to initial retrograde, polar and prograde orbit, while the solid and dashed lines to $m_{\rm p} = 10^{-2}M_\odot$ and $10^{-3}M_\odot$, respectively.

0.5, and 0.1, respectively. In order to see the dependence, we simply repeat the simulations with $m_{\rm p} = 10^{-2}M_\odot$, keeping the other parameters exactly the same. Thus the $m_{\rm p} = 10^{-2}M_\odot$ case corresponds to an order of magnitude increase of $(\Omega_{\rm s}/\Omega_{\rm p})_i$ relative to the $m_{\rm p} = 10^{-3}M_\odot$ case. We do not run the case with $m_{\rm p} = 10^{-2}M_\odot$ and $(L/G)_i = 2$ since it does not satisfy the criterion $\Omega_{\rm p} \gg \Omega_{\rm s}$, under which the $(m, m') = (1, 0)$ is the only excitation mode (Lai 2012). Figure 5.5 basically shows that the result depends on $(\Omega_{\rm s}/\Omega_{\rm p})_i$ very weakly.

5.4 Summary of This Chapter

In this chapter, we have investigated the tidal evolution of star–HJ systems with particular attention to their spin-orbit (re)alignment. We focused on the inertial wave dissipation model proposed by Lai (2012), and examined the extent to which the model reproduces the observed distribution of spin-orbit angles for transiting exoplanets.

Basically we confirmed the conclusion of Rogers & Lin (2013) that the Lai model has three distinct stable configurations, anti-aligned, polar, and aligned orbits. In reality,

however, the former two turn out to be meta-stable, and approach the aligned orbits over a longer timescale as the equilibrium tide effect exceeds that of the inertial wave dissipation. We also found that the later evolution stage needs to be examined using direct three dimensional integrations for the spin vector and orbital angular momentum vector of the system, rather than the simplified differential equations for the semi-major axis, spin angular frequency, and spin-orbit angle, even when a simple star–planet system is considered.

The relative importance of the two tidal effects is determined by the ratio of $\tau_{\rm e}$ and τ_{10}. Unfortunately there is a huge uncertainty in predicting the value of each parameter. Nevertheless in order to achieve a spin-orbit alignment at a finite planetary orbit, $\tau_{10} \ll \tau_{\rm e}$ is required. In such cases, however, the alignment due to the inertial wave dissipation works too efficiently, and the observed broad distribution of ψ for transiting planets (more precisely, the projected angle λ of ψ onto the sky plane) is difficult to reproduce.

To illustrate this point, we simulate 50 systems with a planet located initially at 0.02AU and a randomly chosen ψ_i for $(L/G)_i = 2$, 0.5, and 0.1. Figure 5.6 plots resulting ψ against a at four different epochs; $t/\tau_{\rm e,i} = 0$, 0.03, 0.07, and 0.1. While the ET model (*Upper*) predicts a relatively continuous correlation between ψ and a, the Lai model (*Lower*) has the distinct three (meta-)stable states, but they subsequently become completely aligned by $t = 0.1\tau_{\rm e}$. The evolution is so rapid that even the different value of the initial semi-major axis cannot broaden the distribution significantly.

The observation of the projected spin-orbit angle, λ, has revealed a clear tendency of clumping around $0 < \lambda < 30^\circ$, in addition to the dominance of the prograde orbits relative to the retrograde ones (see Figure 2.3). Nevertheless the distribution is rather broad, and does not seem to be consistent with that expected from Figure 5.6. In order to make more quantitative comparison, one needs to consider the effect of projection since λ is different from ψ, but corresponds to its projected angle on the sky. The effect, however, does not change the main conclusion, and we will leave the detailed analysis to our future study. For this purpose, the simplified set of equations is inappropriate, and we need to integrate three dimensional orbits of multi-planets using the full set of equations in chapter 3. Also it is important and interesting to examine three dimensional evolution of the spin and orbital angular momenta directly, instead of that of their mutual angle alone.

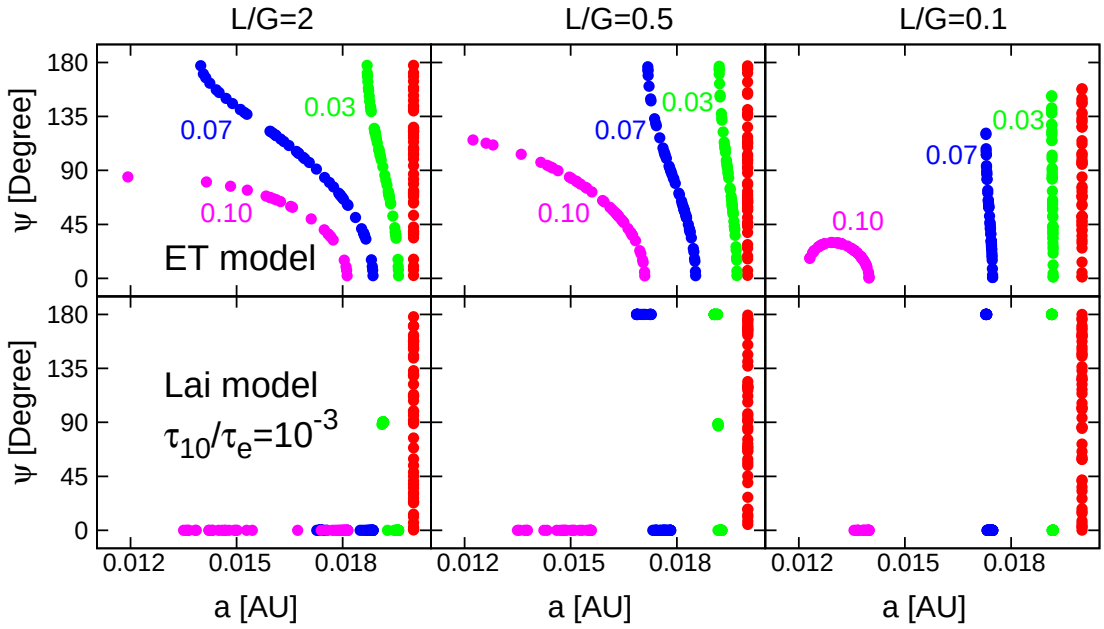

Figure 5.6: Spin-orbit angle plotted against the semi-major axis at different epochs; $t = 0$ (red), $t = 0.03\tau_e$ (green), $t = 0.07\tau_e$ (blue), and $t = 0.1\tau_e$ (magenta). The *upper* and *lower* panels correspond to the equilibrium tide and the Lai models, respectively, for 50 systems with randomly distributed ψ_i. The initial values of L/G are 2 (*Left*), 0.5 (*Center*), and 0.1 (*Right*).

Chapter 6

Summary and Future Prospects

Several formation and migration mechanisms have been proposed to explain the structure of HJs. None of them is fully consistent with observations, but it is also very likely that each of them has contributed to the observed HJs to some degree. Observation of the spin-orbit angle, ψ, may be a useful discriminator of the HJs migration scenarios since each scenario often predicts a different spin-orbit angle distribution.

The projected spin-orbit angle, λ, can be determined through the Rossiter-McLaughlin effect. Indeed, it has revealed about half well-aligned, one-third significant misaligned, and a dozen possible retrograde planets in ~ 90 HJ systems, which have already challenged the conventional theory of planet formation. Although there exists no reliable candidate (yet), the presence of counter-orbiting planets would have an even stronger impact on the formation theory; somewhat conventional migration scenarios including the Lidov-Kozai migration and planet-planet scattering are successful in producing retrograde planets, but fail to explain the counter-orbiting planets in general.

An interesting and attractive possibility is based on the extreme eccentricity evolution expected for the near-coplanar hierarchical triple system. In chapter 4, we investigated such a possibility for the formation of HJs, in particular, counter-orbiting HJs (*Coplanar High-eccentricity Migration, CHEM*). We performed a series of systematic simulations for the sub-stellar and planetary outer perturber cases, and found that most of such systems experience a tidal disruption of the inner planet; a small fraction of prograde HJs are produced; and very few end up with counter-orbiting HJs. We conclude that the formation of counter-orbiting HJs is very difficult even in CHEM. Nevertheless, a reasonable fraction of prograde HJs may have formed through this channel. The survived HJs have bimodal spin-orbit angle distribution; $\sim 0^\circ - 20^\circ$ for prograde, and $\sim 160^\circ - 180^\circ$ for retrograde planets, and virtually nothing in-between. We analytically examined the extreme eccentricity condition and orbital migration timescale in a more realistic situation. In addition, we applied CHEM to the observed exoplanetary systems and found that CHEM can explain a part of hierarchical triple systems, but it is generally very difficult to reproduce counter-orbiting HJ systems.

The difficulty of producing counter-orbiting HJs in CHEM implies that the formation

of counter-orbiting planets imposes an even more serious challenge for the theory. Instead, it could be simply the case that counter-orbiting planet candidates with the projected spin-orbit angle $\lambda \approx 180^\circ$ are mildly misaligned with their true spin-orbit angles ψ being much less than 180° as suggested for HAT-P-7b (Benomar et al. 2014). In this respect, future observational search for the counter-orbiting planets combined with the Rossiter-McLaughlin effect and asteroseismology continues to be important, and hopefully will bring an exciting puzzle for planet formation. Also we note that the presence of numerous tidally disrupted planets is not specific to CHEM, but a fairly generic outcome in planetary migration models and in spin-orbit realignment models (Lai 2012; Li & Winn 2016; Rogers & Lin 2013; Xue et al. 2014). Thus it is of vital importance to look for possible signatures of such tidal disruption events observationally. Indeed recent studies for the determination of the orbital decay rate (Jiang 2016) and for the unusual photometric signals in KIC 8462852 (Bodman & Quillen 2016; Boyajian et al. 2016), for instance, are closely related to such an important direction.

In addition, the range of the semi-major axis of HJs may be another potential discriminator for their formation mechanisms. Our simulation indicates the range of the semi-major axis for HJs in CHEM is mainly determined by the strength of tides. Since in any high-e migration mechanism, the semi-major axis should be similarly determined by the competition between the eccentricity growth and the strength of tides, we expect that the resulting range of the semi-major axis is common for any high-e migration mechanism. On the other hand, disk migration would predict a very different distribution of the semi-major axis because tides are not so important. Therefore, the range of the semi-major axis can potentially distinguish between high-e migration and disk migration. In chapter 4, we find all the three unsuccessful hierarchical triple systems, (Kepler-93, HAT-P-2, and HAT-P-17) have the semi-major axis of the inner planet smaller than their observed values. This implies that those three systems are difficult to form by any high-e migration mechanism, unless tides are unrealistically efficient. Alternatively, those systems may result from disk migration. It is also tempting to apply this prediction of the range of the semi-major axis for other observed close-in planetary systems with a hierarchical triple configuration, so as to estimate the possibility of those systems resulting from high-e migration.

After the tidal circularization of HJs via the orbital migration, stellar tides continuously affect the evolution of the spin-orbit angle, ψ, in a secular timescale, and we focused on this evolution in chapter 5. We performed a series of numerical simulations with a simple star–HJ system in the Lai model, which is a combination of the equilibrium tide model and inertial wave dissipation, and compared with the observed distribution. We found that the Lai model predicts three distinct configurations; anti-aligned, polar, and aligned orbits. In reality, however, both anti-aligned and polar orbits eventually approach the aligned orbit. Our simulation also indicated that the efficient inertial wave dissipation can lead to the realignment prior to the orbital decay.

Due to the total angular momentum conservation, the realignment process leads to an increase of the stellar spin rate. Therefore, the observation of the stellar spin rate with knowing age may reveal some dynamical history of the star (e.g., Bolmont et al.

2012). One limitation of the Lai model is the difficulty to produce intermediate spin-orbit angle, which is not consistent with the current observation. In this sense, the Lai model, at least in the current simple star–planet system, cannot explain the wide range of the observed λ. Also, the current model is unlikely to explain the empirical trend that the realigned systems are preferentially found in the host stars with $T_{\rm eff} < 6250$ K (Winn et al. 2010). Nevertheless we have to recognize that the planetary system considered in chapter 5 is oversimplified; we ignore the outer planets that may influence the dynamics of the innermost planet significantly and the host-star dependence of the tidal parameters. In addition, we totally neglect the dependence on the initial conditions before the tidal realignment. Thus it is premature to make a negative conclusion, and we should explore the wider range of system configurations to our future study.

Appendix A

Notation Sheet

Symbol	**Notation**
m	mass
a	semi-major axis
e	eccentricity
i	inclination
ω	argument of pericenter
l	longitude of ascending node
G	orbital angular momentum
L	spin angular momentum
Ω	rotation frequency
$\Omega_{\rm orb}$	orbital rotation frequency
n	mean motion
ψ	spin-orbit angle
λ	projected spin-orbit angle
$t_{\rm v}$	viscous timescale
Subscript	**Notation**
0	central body
1	inner body
2	outer perturber
s	central star
p	planet
i	initial state
f	final state
e	equilibrium tide
10	inertial wave dissipation

Table A.1: Main notations in the present thesis.

Appendix B

Orbital Average Method

Instead of considering the direct particle evolution, we average the potential over both the inner and the outer orbit, since we are interested in small effects that accumulate over many orbital periods. In this section, we briefly review the orbital average method and its useful formulae following Correia et al. (2011) for completeness.

Considering a function $\mathbf{F}$, its averaged expression over the mean anomaly (M) is

$$\langle \mathbf{F} \rangle_M = \frac{1}{2\pi} \int_0^{2\pi} F dM. \tag{B.1}$$

Also, we can similarly get the averaged expressions over the eccentric anomaly (E), or the true anomaly (f), which are written as

$$\langle \mathbf{F} \rangle_E = \frac{1}{2\pi} \int_0^{2\pi} (1 - e\cos E)\mathbf{F} dE, \tag{B.2}$$

and

$$\langle \mathbf{F} \rangle_f = \frac{1}{2\pi} \int_0^{2\pi} \frac{(1-e^2)^{3/2}}{(1+e\cos f)^2} \mathbf{F} df. \tag{B.3}$$

Substituting equations (B.1) to (B.3) into (3.3) and (3.4), the averaged equations of motion of potential in equations (3.5) and (3.6) can be obtained. Here we give some

useful formulae below,

$$\langle r^2 \rangle = a^2(1+\frac{3}{2}e^2), \tag{B.4}$$

$$\langle \frac{1}{r^3} \rangle = \frac{1}{a^3(1-e^2)^3}, \tag{B.5}$$

$$\langle \frac{1}{r^6} \rangle = \frac{1}{a^6} f_1(e), \tag{B.6}$$

$$\langle \frac{1}{r^8} \rangle = \frac{1}{a^8\sqrt{1-e^2}} f_2(e), \tag{B.7}$$

$$\langle \frac{\cos^2 f}{r^3} \rangle = \frac{1}{2a^3(1-e^2)^3}, \tag{B.8}$$

$$\langle \frac{\sin^2 f}{r^3} \rangle = \frac{1}{2a^3(1-e^2)^3}, \tag{B.9}$$

$$\langle \frac{\cos f \sin f}{r^3} \rangle = 0, \tag{B.10}$$

$$\langle \frac{\mathbf{r}}{r^8} \rangle = \frac{7}{2}\frac{1}{a^9\sqrt{1-e^2}} f_4(e)\mathbf{e}, \tag{B.11}$$

$$\langle \frac{\mathbf{r}}{r^{10}} \rangle = \frac{9}{2}\frac{1}{a^9(1-e^2)} f_5(e)\mathbf{e}, \tag{B.12}$$

$$\langle \frac{(\mathbf{r}\cdot\dot{\mathbf{r}})\mathbf{r}}{r^{10}} \rangle = \frac{n}{2a^7\sqrt{1-e^2}} f_5(e)\hat{\mathbf{k}}\times\mathbf{e}. \tag{B.13}$$

Appendix C

Formation of HJs: the Lidov-Kozai Migration

The Lidov-Kozai migration is a possible formation channel of HJs in hierarchical triple systems, which works in a high mutual inclination configuration in contrast to CHEM. In this section, we briefly review the Lidov-Kozai migration with particular emphasis on the formation of HJs. We summarize the analytical approach in the test particle quadruple approximation and its generalization in the octupole approximation. Then, we discuss the possibility and implication of forming HJs in the Lidov-Kozai migration.

C.1 Test Particle Quadruple Approximation–TPQ

The Lidov-Kozai mechanism, large amplitude modulations between e_1 and i_{12} by the perturbation of the outer perturber when i_{12} passes a threshold value, is first derived from the restricted inner problem in the quadrupole approximation (TPQ) and has been intensively studied by many previous authors. Here we briefly summarize its analytical results in TPQ basically following Fabrycky & Tremaine (2007).

In TPQ, the orbital averaged interaction potential $\langle\Phi\rangle$ becomes

$$\begin{aligned}\langle\Phi\rangle = \langle\Phi_{\rm quad}\rangle &= -\frac{Gm_0m_1m_2}{(m_0+m_1)}\frac{a_1^2}{8a_2^3(1-e_2^2)^{3/2}} \\ &\quad\times[2+3e_1^3-(3+12e_1^2-15e_1^2\cos^2\omega_1)\sin^2 i_{12}], \end{aligned} \tag{C.1}$$

where ω_1 is the argument of pericenter of the inner body. In this limit, there are two conserved quantities in the dimensionless version, which are

$$F = -2-3e_1^2+(3+12e_1^2-15e_1\cos^2\omega_1)\sin^2 i_{12}, \tag{C.2}$$

$$H = \sqrt{(1-e_1^2)}\cos i_{12}, \tag{C.3}$$

and also a useful combination

$$(-1 + 3H^2 + F)/3 = e_1^2(5\sin^2\omega_1 \sin^2 i_{12} - 2). \tag{C.4}$$

Here the constant H suggests that the inner orbital angular momentum along the z-axis is conserved. And since the system is integrable, analytically calculating the value of e_1 and i_{12} at any value of ω_1 is possible. Thus by setting $\dot{e} = 0$, the maximum e_1 and minimum i_{12} are achieved when $\omega_1 = 90°$ or $270°$. If the system is initialized with $e_1 = 0$ and $\omega_1 = 0°$, the maximum eccentricity is

$$e_{1,\max} = \sqrt{1 - \frac{5}{3}\cos^2 i_{12}}. \tag{C.5}$$

And the minimum i_{12} is

$$\cos i_{12,\min} = \pm\sqrt{\frac{3}{5}}, \tag{C.6}$$

which gives $i_{12,\min} \approx 39.2°$. Here we restrict our discussion to $i_{12} < 90°$. The behavior for retrograde systems is identical to prograde systems mirrored across $90°$, with $i_{12,\max} \approx 140.8°$. The large amplitude oscillations of e_1 and i_{12} happen only when the initial inclination falls in $39.2° < i_{12,i} < 140.8°$.

C.2 Eccentric Outer Orbit in Octupole Approximation– EKL

Recently, it has been recognized that the higher order terms, in particular, the octupole term of the interaction potential and an eccentric perturber ($e_2 > 0$) can lead to a much dramatic dynamical behavior comparing to the simplest TPQ (Naoz et al. 2011, 2013). This mechanism is often referred to as the eccentric Lidov-Kozai mechanism (EKL). The octupole term in the Hamiltonian shows up when $e_2 > 0$, and ϵ in equation (3.8) quantifies the importance of the octupole term relative to the quadrupole term.

In the octupole approximation, the z-component of the inner orbital angular momentum is not yet conserved. The evolution becomes chaotic and the eccentricity of the inner body can reach an extremely high value. The extreme eccentricity is often associated with the orbital flip between $i_{12} < 90°$ and $i_{12} > 90°$ in the octupole approximation. Such flip behavior cannot happen in the quadrupole approximation.

The octupole term qualitatively changes the orbital evolution comparing with in the quadrupole approximation, while one may concern that the higher order terms may change the behavior of the system as dramatic as the octupole term, but it is not the case. In the quadrupole approximation, e_2 is a constant value, but it becomes not conserved when including the octupole term. There is no more constancy break-down when moving to even higher orders, and therefore, no more drastic change in the orbital evolution. This statement is confirmed by a comparison of the octupole approximation and the direct N-body integrations by (Naoz et al. 2013).

C.3 Formation of HJs

As an effective mechanism to enhance the eccentricity of the inner orbit, the Lidov-Kozai mechanism has been intensively studied as a potential channel to form HJ. Naoz et al. (2012) studied the formation and evolution of HJs in wide stellar binaries in EKL by a large set of Monte Carlo simulations. They compared the final distribution of the projected spin-orbit angle λ in EKL to λ in planet-planet scattering (Nagasawa & Ida 2011) and the observation. They found that EKL can account for about 30% of the observed HJ population independently of the formation rate. They also found that the distribution of ψ has a characteristic cut-off near 140° due to the seperatrix of the Lidov-Kozai mechanism.

Recently, A similar population synthesis study of EKL in wide stellar binaries has been presented by Petrovich (2015a). He noticed that the distribution of the semi-major axis of HJs produced in EKL is generally smaller than the observation and the formation efficiency largely depends on the disruption radius–the Roche limit.

C.4 Extreme Eccentricity Suppression with SRFs

In this subsection, we review the effect of extreme eccentricity suppression due to SRFs effect in the Lidov-Kozai migration. In the Lidov-Kozai regime, Liu et al. (2015) found that SRFs impose a strict upper limit on the maximum achievable value of e_1. As SRFs become stronger, the orbital flip is more confined to the region where the mutual orbital inclination i_{12} is closer to 90°. The maximum achievable e_1 when including SRFs can be analytically calculated in the test particle quadrupole approximation by assuming that the system starts with $e_1 = 0$ and reaches the maximum eccentricity when $\omega_1 = \pi/2$ or $3\pi/2$ as below.

$$\epsilon_{\rm GR}(\frac{1}{j_{1,\rm min}} - 1) + \frac{\epsilon_{\rm tide}}{15}(\frac{1 + 3e_{1,\rm max}^2 + \frac{3}{8}e_{1,\rm max}^4}{j_{1,\rm min}^9} - 1)$$
$$+\frac{\epsilon_{\rm rot}}{3}(\frac{1}{j_{1,\rm min}^3} - 1) = \frac{9}{8}\frac{e_{1,\rm max}^2}{j_{1,\rm min}^2}(j_{1,\rm min} - \frac{5}{3}\cos^2 i_{12}^2), \tag{C.7}$$

where $j_{1,\rm min} = \sqrt{1 - e_{1,\rm max}}$ and $\epsilon_{\rm GR}, \epsilon_{\rm tide}$, and $\epsilon_{\rm rot}$ are the characteristic parameter for GR, planetary non-dissipative tides, and planetary rotational distortion, respectively.

The maximum achievable value of the eccentricity of the inner body, $e_{1,\rm max}$ is reached when initial $i_{12} = 90°$. This threshold holds even if taking into account the octupole terms, but the range of initial i_{12} for which $e_{1,\rm max}$ can be reached is significantly enlarged. Comparing to purely gravitational interaction, including SRFs effect moves the orbital flip region closer to 90°.

Appendix D

Basic Equations for Tidal Evolution in the Lai Model

In chapter 5, we consider a hybrid tidal model which combines the conventional equilibrium tide model with the inertial tidal dissipation model proposed by Lai (2012). Just for completeness, we explicitly give a full set of basic equations that we numerically integrate.

The full sets of equations for the hierarchical triple systems including SRFs effect and tidal dissipation have been fully described in section 3.1 and 3.3. In chapter 5, we focus on the tidal interaction between the star and the innermost planet. Thus we neglect the distant planet for simplicity. The tide on the planet is not considered either because it should have a very negligible effect on the dynamics of the star and planet. Furthermore since we fix the initial eccentricity as 0 in the current simulations, the GR effect is also neglected.

As Correia et al. (2011) described in detail, the evolution of the system is governed by the conservative motion and the tidal effects. First, the equation for conservative motion is obtained by averaging the equations of motion over the mean anomaly:

$$\dot{\mathbf{G}}_{(\mathrm{c})} = \alpha \cos\psi \hat{\mathbf{s}} \times \hat{\mathbf{k}}, \tag{D.1}$$

$$\dot{\mathbf{L}}_{(\mathrm{c})} = -\alpha \cos\psi \hat{\mathbf{s}} \times \hat{\mathbf{k}}, \tag{D.2}$$

where the subscript (c) refers to conservative motion, and

$$\alpha = \frac{3Gm_{\mathrm{s}}m_{\mathrm{p}}J_{2_s}R_s^2}{2a^3}. \tag{D.3}$$

Second, the equilibrium tidal effect is considered under the quadrupole approximation of the tidal potential assuming the constant delay time Δt_{L} (Mignard 1979). After averaging equations of motion over the mean anomaly, one obtains

$$\begin{aligned} \dot{\mathbf{G}}_{(\mathrm{t})} &= -\dot{\mathbf{L}}_{(\mathrm{t})}, \\ \dot{\mathbf{L}}_{(\mathrm{t})} &= K\Big[\frac{\Omega_{\mathrm{s}}}{2}(\hat{\mathbf{s}} - \cos\psi\hat{\mathbf{k}}) - \Omega_{\mathrm{s}}\hat{\mathbf{s}} + \Omega_{\mathrm{orb}}\hat{\mathbf{k}}\Big], \end{aligned} \tag{D.4}$$

where the subscript (t) refers to equilibrium tidal effects, and

$$K = \Delta t_{\rm L} \frac{3k_2 G m_{\rm p}^2 R_{\rm s}^5}{a^6}. \tag{D.5}$$

Thus the total rates of change of G and L under the equilibrium tidal model are given by the sum of the above terms corresponding to the conservative motion and equilibrium tidal effect:

$$\dot{\mathbf{G}}_{\rm (e)} = \dot{\mathbf{G}}_{\rm (c)} + \dot{\mathbf{G}}_{\rm (t)}, \tag{D.6}$$

$$\dot{\mathbf{L}}_{\rm (e)} = \dot{\mathbf{L}}_{\rm (c)} + \dot{\mathbf{L}}_{\rm (t)}. \tag{D.7}$$

Finally, we add the tidal torque due to the inertial wave dissipation, equations (3.60) to (3.62) to the above equations as in equations (5.1) and (5.2).

Appendix E

Mutual Inclination of Warm Jupiters

In addition to the planetary systems in CHEM and the Lai model, the secular equations set we adopt in chapter 3 can be applied to a wide range of astrophysical systems for various motivations. In this section, we describe the mutual inclination of Warm Jupiters (WJs, hereafter) by adopting secular equations and discuss its implications.

WJs are defined as gas giant with period within $10 - 100$ days in contrast with HJs (< 10 days). The formation of WJs poses similar puzzle like that of HJs. Among WJs detected by radial velocities (RVs), more than half of the eccentric WJs have known Jupiter-like companions, but only $< 20\%$ low-e WJs have detected Jupiter-like companions (Dong et al. 2014). This implies a possibility that two populations of WJs with different characteristics exist; one form in-situ or by disk migration, the other form in high-e migration.

The observed WJs are sufficiently distant from their host stars ($q = a(1 - e) > 0.1$ AU) to avoid of efficient tidal dissipation. However, if the observed eccentric WJs are now involving the Lidov-Kozai oscillation due to the perturbation of the outer companion, the planets may be currently at the low-e stage of the Lidov-Kozai oscillation and circularize over a secular timescale. For this reason, the measurement of the mutual orbital inclination, i_{12}, can be a useful probe in understanding the origin of WJs. However, the direct observation is currently difficult.

Recently, Dawson et al. (2014) claimed that the observed eccentric WJs with eccentric giant companions tend to have mutual orbital inclinations between 35° to 65°. His statement is based on the observation trend that the observed sky-projected pericenter separations between WJs and their companions, $|\Delta\omega_{\rm sky}| = |\omega_{1,\rm sky} - \omega_{2,\rm sky}|$, cluster near 90°. They performed the numerical simulations with different initial mutual orbital inclination, and found that the systems spend excess time on $75° < |\Delta\omega_{\rm sky}| < 135°$ when $35° < i_{12} < 65°$. They suggested that these inclined systems may be undergoing very slow Lidov-Kozai migration due to the modulation of octupole-induced envelope, which results in WJs over HJs.

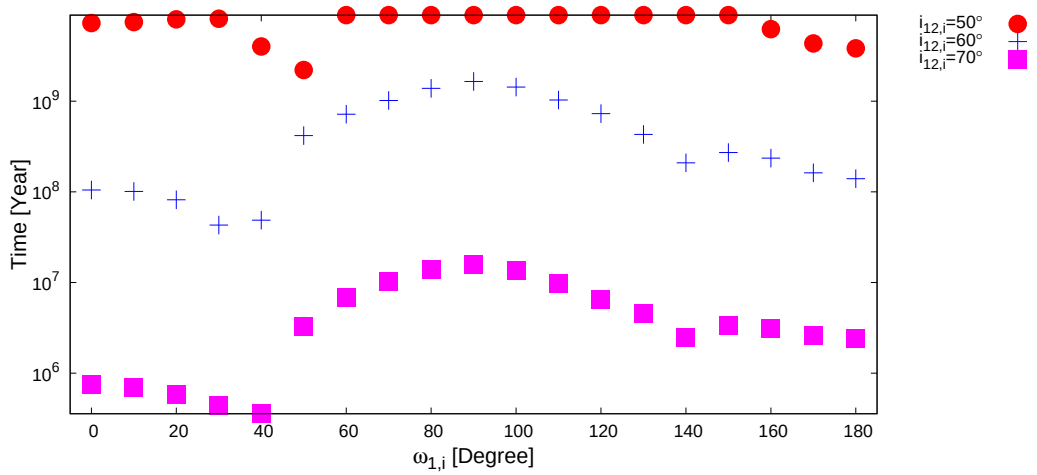

Figure E.1: Circularization timescale ($e < 0.01$) of HD 147018 against $\omega_{1,i}$. The red filled circle, blue plus, and magenta filled square represent $i_{12,i} = 50°$, 60°, and 70°, respectively.

The stability of the hierarchical WJ systems is determined by the circularization timescale ($e_1 < 0.01$), which puts yet another constraint on the mutual orbital inclination. In this section, we examine in detail the stability of one hierarchical WJ system, HD 147018, to constrain its i_{12}, and this methodology can be easily applied to the other hierarchical WJ systems. HD 147018 consists of a sun-like central star ($m_0 = 0.927 M_\odot$), an eccentric WJ ($m_1 = 2.127 M_\mathrm{J}$, $R_1 = 1.23 R_\mathrm{J}$, and $a_1 = 0.239$ AU), and an eccentric planetary distant perturber ($m_2 = 6.59 M_\mathrm{J}$ and $a_2 = 1.92$ AU). We run simulations over the grids of ($i_{12,i}$, $\omega_{1,i}$) plane. $i_{12.i}$ is varied between 35° to 70° with constant interval 5°, and $\omega_{1,i}$ is varied between 0° to 180° with constant interval 10°. We set the tidal delay time for the central star and inner planet to 0.1 s and 40 s, respectively. The initial phase angle are fixed to $\omega_2 = 0°$, $l_1 = 180°$, $l_2 = 0°$. We stop the simulations when the inner planet is fully circularized ($e_1 < 0.01$).

The selected results with $i_{12,i} = 50°, 60°$, and 70° are shown in Figure E.1. The circularization timescale decreases as $i_{12,i}$ increases. $i_{12,i} > 60°$ can be ruled out due to very fast circularization timescale ($< 10^9$ yr). In addition to $i_{12,i}$, $\omega_{1,i}$ also play an important role on determining the timescale. The systems closer to $\omega_{1,i} = 90°$ are more stable. And there are a relatively sharp change of timescale between $\omega_{1,i} = 40°$ (140°) and $\omega_{1,i} = 50°$ (130°). This is related to the separatrix between libration and circulation of $\omega_{1,i}$. As shown in Figure E.2, the planet within libration spends less time near its pericenter, since its eccentricity has a strongly modulated envelope.

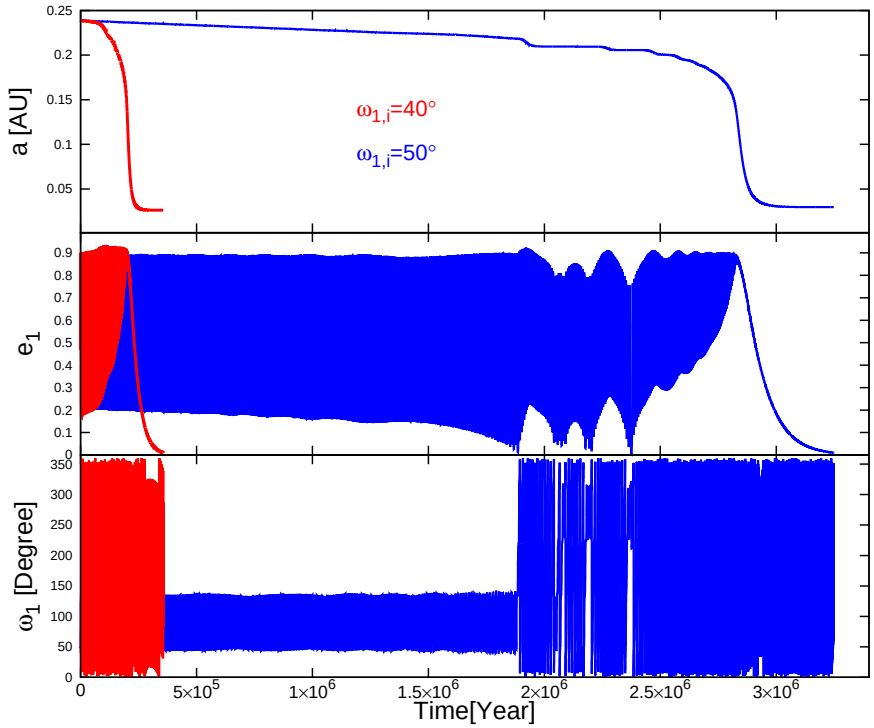

Figure E.2: Orbital evolution of the semi-major axis, a_1, eccentricity, e_1, and argument of pericenter of the inner planet, ω_1, for HD 147018 with $i_{12,i} = 70°$. Red and blue solid lines represent $\omega_{1,i} = 40°$ and $50°$, respectively.

Appendix F

Orbital Elements Conversion

In the simulation, we adopt the z-axis along with the total angular momentum vector (perpendicular to the invariable plane) and the x-axis initially along with the longitude of ascending node of the outer orbit ($l_2 = 0$). Then we can set the initial values of the Lenz vector, $\mathbf{e}$, by the following matrix multiplication (c.f., Murray & Dermott 1999),

$$\mathbf{e} = e \begin{bmatrix} \cos l \cos \omega - \sin l \sin \omega \cos i \\ \sin l \cos \omega + \cos l \sin \omega \cos i \\ \sin \omega \sin i \end{bmatrix}, \tag{F.1}$$

where i is the inclination of the orbit with respect to the invariable plane.

Given the orbital and spin angular momentum vector and the Lenz vector, the eccentricity, semi-major axis, spin rotation frequency, inclination to the invariable plane, mutual inclination, and spin-orbit angle can be directly obtained from the definition. The deduction of the argument of pericenter and longitude of ascending node may not be so intuitive, which we describe as below (c.f., Murray & Dermott 1999).

First, we consider a node vector, $\mathbf{n}$, which points to the ascending node in the orbital plane,

$$\mathbf{n} = \hat{k} \times \mathbf{G}, \tag{F.2}$$

where $\hat{k}$ is the unit vector along with the z-direction.

The longitude of ascending node is the angle between the node vector, $\mathbf{n}$, and the x-axis, $\hat{i}$,

$$l = \cos^{-1}\left(\frac{\hat{i} \cdot \mathbf{n}}{|\mathbf{n}|}\right). \tag{F.3}$$

If $\mathbf{n} \cdot \hat{j} < 0$, $l = 2\pi - l$, where $\hat{j}$ is the unit vector along with the y-direction, since a negative y-component corresponds to l between π and 2π.

The argument of pericenter is the angle between the ascending node and the Lenz vector,

$$\omega = \cos^{-1}\left(\frac{\mathbf{e}\cdot\mathbf{n}}{|\mathbf{n}|e}\right). \tag{F.4}$$

If $\mathbf{e}\cdot\hat{k} < 0$, $\omega = 2\pi - \omega$, since the Lenz vector in the bottom half plane corresponds to ω between π and 2π.

Appendix G

Numerical Method

In this section, we briefly review the Embedded Runge-Kutta method (Numerical Recipes in C 2nd ed.), which is adopted in the simulations to integrate the ordinary differential equations.

The Runge-Kutta method as an important family of iterative methods is often used to obtain numerical solution for a set of first-order differential equations:

$$\frac{dy_i}{dx} = f_i(x, y_1, \cdots, y_N), \qquad (i = 1, \cdots, N). \tag{G.1}$$

The basic idea of all the Runge-Kutta methods is to move from step y_i to y_{i+1} by multiplying some estimated slope with a timestep h. Combining the information from several Euler-style steps, they draw a solution over one interval and match a Taylor series expansion up to a higher order.

The formulae of the simplest second order Runge-Kutta method are

$$\begin{aligned} k_1 &= hf(x_n, y_n), \\ k_2 &= hf(x_n + \frac{h}{2}, y_n + \frac{k_1}{2}), \\ y_{n+1} &= y_n + k_2 + O(h^3). \end{aligned} \tag{G.2}$$

The first-order error term is canceled due to the symmetrization. Indeed, the error terms can be eliminated order by order with the appropriate combination of these, and the Runge-Kutta method reaches a higher order accuracy.

The formulae of the most often used classical 4-th order Runge-Kutta method (RK4)

are

$$\begin{aligned} k_1 &= hf(x_n, y_n), \\ k_2 &= hf(x_n + \frac{h}{2}, y_n + \frac{k_1}{2}), \\ k_3 &= hf(x_n + \frac{h}{2}, y_n + \frac{k_2}{2}), \\ k_4 &= hf(x_n + h, y_n + k_3), \\ y_{n+1} &= y_n + \frac{k_1}{6} + \frac{k_2}{3} + \frac{k_3}{3} + \frac{k_4}{6} + O(h^5), \end{aligned} \tag{G.3}$$

which gives the solution from x_n to $x_{n+1} = x_n + h$ with error term $O(h^5)$. However, in the current simulations, this traditional method may not provide a reasonably good accuracy. Therefore, we consider the modified Runge-Kutta method to increase the precision.

Step-size control is very useful to achieve some predetermined accuracy with given computational efficiency. One plausible way to increase the accuracy is to solve the problem twice using step sizes h and $h/2$. Using this method, we can make the accuracy up to 5-th order, but this method is not efficient enough. It significantly increases the computation time and the truncation error of this method is not guaranteed. Indeed, the higher order does not always mean the higher accuracy.

The higher accuracy can be achieved in another way based on the Embedded Runge-Kutta formulae (Fehlberg 1969). A 5-th order method with 6 function evaluations which was originally given as a 4-th order method has been found. The truncation error can be estimated by the difference between the two methods of $y(x + h)$ in order to adjust the stepsize. And in this sense, the lower order method is embedded to the higher order one.

The general form of a 5-th order Runge-Kutta formulae are given as

$$\begin{aligned} k_1 &= hf(x_n, y_n), \\ k_2 &= hf(x_n + a_2 h, y_n + b_{21} k_1), \\ &\cdots \\ k_6 &= hf(x_n + a_6 h, y_n + b_{61} k_1 + \cdots + b_{65} k_5), \\ y_{n+1} &= y_n + c_1 k_1 + \cdots + c_6 k_6 + O(h^6). \end{aligned} \tag{G.4}$$

The embedded 4-th order formula is

$$y^*_{n+1} = y_n + c^*_1 k^*_1 + \cdots + c^*_6 k^*_6 + O(h^5). \tag{G.5}$$

The error is estimated as follows,

$$\Delta \equiv y_{n+1} - y^*_{n+1} = \sum_{i=1}^{6} (c_i - c^*_i) k_i. \tag{G.6}$$

The particular choice for the unknown parameters of this method are given in Table G.1, which was found by Cash and Karp.

Cash-Karp Parameters for Embedded Runga-Kutta Method								
i	a_i	b_{ij}					c_i	c_i^*
1							$\frac{37}{378}$	$\frac{2825}{27648}$
2	$\frac{1}{5}$	$\frac{1}{5}$					0	0
3	$\frac{3}{10}$	$\frac{3}{40}$	$\frac{9}{40}$				$\frac{250}{621}$	$\frac{18575}{48384}$
4	$\frac{3}{5}$	$\frac{3}{10}$	$-\frac{9}{10}$	$\frac{6}{5}$			$\frac{125}{594}$	$\frac{13525}{55296}$
5	1	$-\frac{11}{54}$	$\frac{5}{2}$	$-\frac{70}{27}$	$\frac{35}{27}$		0	$\frac{277}{14336}$
6	$\frac{7}{8}$	$\frac{1631}{55296}$	$\frac{175}{512}$	$\frac{575}{13824}$	$\frac{44275}{110592}$	$\frac{253}{4096}$	$\frac{512}{1771}$	$\frac{1}{4}$
$j=$		1	2	3	4	5		

Table G.1: Cash-Karp parameters for the Embedded Runge-Kutta method.

The error-estimated equation to control the step size is useful to optimize the simulations. The basic idea is to set a satisfied level of the truncation error and modify the step size to achieve. Suppose a truncation error Δ_1 for step size h_1, if we want to reduce the truncation error to Δ_0, we require a new timestep h_0, which is given by

$$h_0 = h_1(|\frac{\Delta_0}{\Delta_1}|)^{0.2}. \tag{G.7}$$

If $\Delta_1 > \Delta_0$, the stepsize has to be decreased and vice versa. The optimal step control equation can be written as

$$\Delta_0 = \begin{cases} \alpha h_1(|\frac{\Delta_0}{\Delta_1}|)^{0.2} & \Delta_0 \geq \Delta_1, \\ \alpha h_1(|\frac{\Delta_0}{\Delta_1}|)^{0.25} & \Delta_0 < \Delta_1, \end{cases} \tag{G.8}$$

where α is a control parameter and set to 0.1 in the current simulation.

Give above formulae, this Embedded Runge-Kutta Method satisfies our requirement.

Appendix H

Test of Numerical Simulation Robustness

The embedded Runge-Kutta method has been widely used in this field, and simply the question is what value of the error term, Δ, which controls the overall accuracy, should be employed for each single step in the current simulations. We try $\Delta = 10^{-12}$, 10^{-13}, 10^{-14}, and 10^{-15}. The result with $\Delta = 10^{-12}$ is slightly different from the others, but the rest are converged. For instance, we show the result of $\Delta = 10^{-13}$ in Figure H.1, which is identical to Figure 4.3 with $\Delta = 10^{-14}$ of our fiducial choice. We conclude that the error term $\Delta = 10^{-14}$ we adopt in the simulation satisfies our requirement of accuracy.

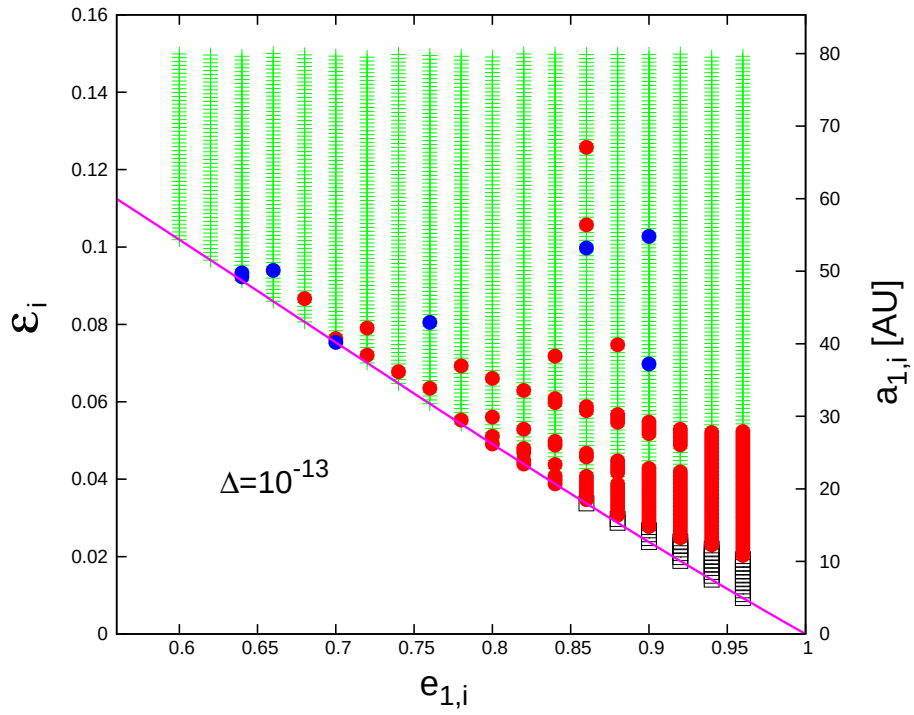

Figure H.1: The initial condition here is identical to the extreme eccentricity region in Figure 4.3 except with the error term $\Delta = 10^{-13}$. Fate of the inner planet on the $(e_{1,i}, \epsilon_{1,i})$ plane; $a_{2,i} = 500$ AU, $m_2 = 0.03 M_\odot$, $e_{2,i} = 0.6$, $t_{\rm v,p} = 0.03$ yr. The final states are indicated by green crosses for Disrupted planets (TD), black open squares for Non-migrating planets (NM), red filled circles for Prograde HJs (PHJ), and blue filled circles for Retrograde HJs (RHJ), respectively. The magenta line is the extreme eccentricity condition in the test particle limit.

Appendix I

Dependence on the Phase Angle

In chapter 4, we adopt fixed phase angles with $\omega_{1,i} = 0°$, $\omega_{2,i} = 0°$, $l_{1,i} = 180°$, and $l_{2,i} = 0°$. This choice is rather arbitrary, but reflects the structure of the extreme eccentricity region. The extreme eccentricity condition depends on the phase angles (see equation (4.8) for example). Indeed, the phase-space trajectory is determined by the potential and total angular momentum. Therefore, different phase angles correspond to the different location on the $(e_{1,i}, \epsilon_{1,i})$ plane, and different analytical extreme eccentricity condition. On the other hand, the fiducial choice we adopt for the phase angles corresponds to the local minimum of the inner orbital eccentricity, which provides the largest parameter space in the extreme eccentricity region on the $(e_{1,i}, \epsilon_{1,i})$ plane. This fiducial choice of phase angles was also adopted by Li et al. (2014) and Petrovich (2015b).

In order to see an example of the dependence on phase angles, we repeat our fiducial runs in subsection 4.3.2 with one set of different values of phase angles with $\omega_{1,i} = 30°$, $\omega_{2,i} = 10°$, $l_{1,i} = 80°$, and $l_{2,i} = 0°$. The final states of the inner planet are plotted in Figure I.1. The result is qualitatively consistent with Figure 4.3 with branching ratios; NM 1.9% PHJ 3.5% RHJ 0.8% TD 93.8%. Thus, we conclude that the different choice of phase angles does not qualitatively change the final result. The main conclusion of the present thesis remains the same.

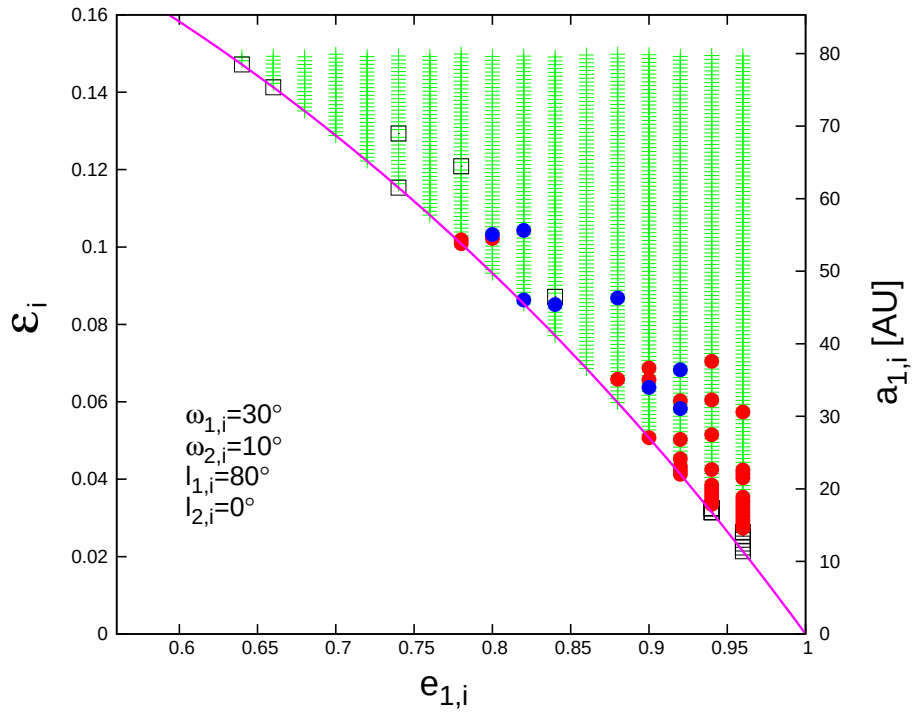

Figure I.1: The initial condition here is identical to the extreme eccentricity region in Figure 4.3 except with phase angles; $\omega_{1,i} = 30°$, $\omega_{2,i} = 10°$, $l_{1,i} = 80°$, and $l_{2,i} = 0°$. Fate of the inner planet on the $(e_{1,i}, \epsilon_{1,i})$ plane; $a_{2,i} = 500$ AU, $m_2 = 0.03 M_\odot$, $e_{2,i} = 0.6$, $t_{\rm v,p} = 0.03$ yr. The final states are indicated by green crosses for Disrupted planets (TD), black open squares for Non-migrating planets (NM), red filled circles for Prograde HJs (PHJ), and blue filled circles for Retrograde HJs (RHJ), respectively. The magenta line is the extreme eccentricity condition in the test particle limit.

References

Albrecht, S., Winn, J. N., Johnson, J. A., et al. 2012, ApJ, 757, 18

Albrecht, S., Winn, J.N., Marcy, G.W., Howard, A.W., Isaacson, H., & Johnson, J.A. 2013, ApJ, 771, 11

Alibert Y., Mordasini C., Benz W., Winisdoerffer C., 2005, A&A, 434, 343

Anderson K. R., Storch N. I., Lai D., 2016, MNRAS, 456, 3671

Barker, A. J., & Ogilvie, G. I. 2009, MNRAS, 395, 2268

Bate, M. R., Lodato, G., & Pringle, J. E. 2010, MNRAS, 401, 1505

Batygin, K. 2013, Natur, 491, 418

Batygin, K., Bodenheimer P. H., Laughlin G. P. 2016, ApJ, 829, 114

Beauge C., & Nesvorny D., 2012, AJ 751, 119

Benomar, O., Masuda, K., Shibahashi, H., & Suto, Y. 2014, PASJ, 66, 94

Bodenheimer, P., & Pollack, J. B. 1986, Icarus, 67, 391

Bodman, E.H., & Quillen, A. 2016, ApJ, 819, 34

Boley A.C., Granados C.B., Gladman B. 2016, ApJ, 817, 17

Bolmont, E., Raymond, S. N., Leconte, J., & Matt, S. P. 2012, A&A, 544, A124

Borkovits, T., Hajdu, T., Sztakovics, J., et al. 2016, MNRAS, 455, 4136

Boyajian, T.S., et al. 2016, MNRAS, 457, 3988

Brewer, J.M., Fischer D.A., & Madhusudhan N., arXiv:1612.0437

Campante, T. L., ph.D.thesis, arXiv:1405.3145

Chambers, J. E., & Wetherill, G. W. 1998, Icarus, 136, 304

Chatterjee, S., Ford, E. B., Matsumura, S., & Rasio, F. A. 2008, ApJ, 686, 580

Chatterjee, S. & Tan, J. C. 2015, ApJL, 798, L32

Christensen-Dalsgaard, J. 2014, Lecture Notes on "Stellar Oscillations", fifth edition, http://astro.phys.au.dk/~jcd/oscilnotes/

Correia ACM., & Laskar J., 2010b, Exoplanets, University of Arizona Press, pp 534-575

Correia, A. C. M., Laskar, J., Farago, F., & Boue, G. 2011, Celest. Mech. Dyn. Astron., 111, 105

Dawson RI, Chiang E. 2014. Science 346:212

Dong, S., Katz, B., & Socrates, A. 2014, ApJ, 781, L5

Faber, J. A., Rasio, F. A., & Willems, B. 2005, Icarus, 175, 248

Fabrycky,D. & Tremaine, S. 2007, ApJ, 669, 1298

Ferraz-Mello, S., Rodrguez, A., & Hussmann, H. 2008, Celest. Mech. Dyn. Astron., 101, 171

Foucart, F., & Lai, D. 2011, MNRAS, 412, 2799

Gizon, L., & Solanki, S.K. 2003, ApJ, 589,1009

Goldreich, P. 1963, MNRAS, 126, 257

Goldreich, P., & Tremaine, S. 1980, ApJ, 241, 425-441

Goodman, J. & Lackner, C. 2009, ApJ, 696, 2054

Greenberg, R. 2009, ApJ, 698, L42

Guillochon, J., Ramirez-Ruiz, E., & Lin, D. 2011, ApJ, 732, 74

Hamers, A.S., et al. 2017, MNRAS, 464, 668

Harrington R. S., 1968, AJ, 73, 190

Hayashi, C. 1981, Progress of Theoretical Physics Supplement, 70, 35

Hirano, T., Suto, Y., Winn, J. N., Taruya, A., Narita, N., Albrecht, S., & Sato, B. 2011, ApJ, 742, 69

Holman M., Touma J., Tremain S., 1997, Nature, 386, 254

Howard, A. W., Bakos, G. A., Hartman, J., et al. 2012, ApJ, 749, 134

Howe, R. 2009, Living Rev. Sol. Phys., 6, 1

Huber, D., et al. 2013, Science, 342, 331

Ida, S., & Lin, D. N. C. 2004, ApJ, 604, 388

Ida, S., & Lin, D. N. C. 2004, ApJ, 616, 567

Jiang, I.G., et al. 2016, AJ, 151, 17

Kaula, W.M. 1964, Rev. Geophys. 2, 661-685

Knutson, H. A., Fulton, B. J., Montet, B. T., et al. 2014, ApJ, 785, 126

Kokubo, E. & Ida, S. 1998. Icarus 131, 171-178.

Kokubo, E. & Ida, S. 2000. Icarus 143, 15-27.

Kokubo, E., Kominami, J., & Ida, S. 2006, ApJ, 642, 1131

Kovacs, G., Bakos, G. A ., Torres, G., et al. 2007, ApJL, 670, L41

Kozai, Y. 1962, AJ, 67, 591

Lai D., Foucart F., Lin D. N. C., 2011, MNRAS, 412, 2790

Lai, D. 2012, MNRAS, 423, 486

Lai, D. 2014, MNRAS, 440, 3532

Lainey, V., Arlot, J., Karatekin, O., & van Hoolst, T. 2009, Nature, 459, 957

Levrard B., Winisdoerffer C., & Chabrier G., 2009, ApJ, 692, L9

Li, G., Naoz, S., Kocsis, B., & Loeb, A. 2014, ApJ, 785, 116

Li, G., & Winn, J. N. 2016, ApJ, 818, 5

Lin, D. N. C., & Papaloizou, J. C. B. 1986, ApJ, 309, 846-857

Lin, D. N. C., Bodenheimer, P., & Richardson, D. 1996, Nature, 380, 606

Lidov, M. L. 1962, P&SS, 9, 719

Liu, B., Munoz, D. J., & Lai, D. 2015, MNRAS, 447, 747

Lubow, S. H., & Ida, S. 2010, in Exoplanets, editor S. Seager, University of Arizona Press, arXiv:1004.4137v1

Luo, L., B. Katz, & S. Dong, 2016, MNRAS, 458, 3060.

MacDonald, G. J. F., 1964. Revs. Geophys. 2, 467-541.

Madhusudhan, N., Amin, M. A., & Kennedy, G. M. 2014, ApJL, 794, L12

Marcy, G. W., Isaacson, H., Howard, A. W., et al. 2014, ApJS, 210, 20

Masuda,K., Hirano,T., Taruya,A., Nagasawa,M., & Suto, Y. 2013, ApJ, 778, 185

Matsumura S., Peale S. J., & Rasio F. A., 2010, ApJ, 725, 1995

Maxted, P. F. L., Anderson, D. R., Gillon, M., et al. 2010, AJ, 140, 2007

Mayor, M., & Queloz, D. 1995, Nature, 378, 355

McLaughlin, D. B. 1924, ApJ, 60, 22

Mignard, F., Moon Planets 1979, 20, 301-315

Mizuno, H. 1980, Progress of Theoretical Physics, 64, 544

Murray, C.D., & Dermott, S.F. 1999, Solar System Dynamics (Cambridge Univ. Press; Cambridge, New York)

Nagasawa, M., Ida, S., & Bessho, T. 2008, ApJ, 678, 498

Nagasawa, M., & Ida, S. 2011, ApJ, 742, 72

Naoz, S., Farr, W. M., Lithwick, Y., Rasio, F. A., & Teyssandier, J. 2011, Nature, 473, 187

Naoz, S., Farr, W. M., & Rasio, F.A., 2012, ApJ, 754, L36

Naoz, S., Farr, W. M., Lithwick, Y., Rasio, F. A., & Teyssandier, J. 2013, MNRAS, 431, 2155

Naoz, S., & Fabrycky, D. C. 2014, ApJ, 793, 137

Noyes, R. W., Bakos, G. A., Torres, G., et al. 2008, ApJL, 673, L79

Ohta, Y., Taruya, A., & Suto Y. 2005, ApJ, 622, 1118

Pal, A., Bakos, G. A ., Torres, G., et al. 2010, MNRAS, 401, 2665

Papaloizou, J. C. B., Nelson, R. P., & Masset, F. 2001, A&A, 366, 263

Petrovich C., 2015a, ApJ, 799, 27

Petrovich C., 2015b, ApJ, 805, 75

Pollack, J. B., Hubickyj, O., Bodenheimer, P., Lissauer, J. J., Podolak, M., & Greenzweig, Y. 1996, Icarus, 124, 62

Queloz, D., Eggenberger, A., Mayor, M., Perrier, C., Beuzit, J. L., Naef, D., Sivan, J. P., & Udry, S. 2000, A&A, 359, L13

Rasio, F. A., & Ford, E. B., 1996, Science, 274, 954

Raymond, S. N., & Cossou, C. 2014, MNRAS, 440, L11

Rice K., 2015, MNRAS, 448, 1729

Rogers, T. M., Lin, D. N. C., & Lau, H. H. B. 2012, ApJ, 758, L6

Rogers, T.M. , & Lin, D.N.C. 2013, ApJL, 769:L10

Rossiter, R. A. 1924, ApJ, 60, 15

Socrates, A., Katz, B., & Dong, S. 2012, arXiv:1209.5724

Spalding C., & Batygin K., 2014, ApJ, 790, 42

Steffen, J. H., Ragozzine, D., Fabrycky, D. C., et al. 2012, Proceedings of the National Academy of Science, 109, 7982

Storch, N. I., & Lai, D. 2014, MNRAS, 438, 2

Teyssandier, J., Naoz, S., Lizarraga, I., & Rasio, F. 2013, ApJ, 779, 166

Timpe M. L., Barnes R., Raymond S. N., and Gorelick N. 2012, in: American Astronomical Society Meeting Abstracts, vol. 219 of American Astronomical Society Meeting Abstracts, p.339.12.

Torres, G., Bakos, G. A., Hartman, J., et al. 2010, ApJ, 715, 458

Triaud A., 2011, A&A, 534, L6

Trilling, D. E., Benz, W., Guillot, T., Lunine, J. I., Hubbard, W. B., & Burrows, A. 1998, ApJ, 500, 428

Unno, W., Osaki, Y., Ando, H., Saio, H., & Shibahashi, H. 1989, Nonradial Oscillation of Stars (Tokyo: University of Tokyo Press)

Xue, Y., Suto, Y., Taruya, A., Hirano, T., Fujii, Y., & Masuda, K. 2014, ApJ, 784, 66

Xue, Y., & Suto, Y., 2016, ApJ, 820, 55

Xue, Y., Masuda, K., & Suto, Y., 2016, ApJ, 820, 55

Weiss, L. M., & Marcy, G. W. 2014, ApJ, 783, L6

Winn, J. N., Noyes, R.W., Holman, M.J., Charbonneau, D., Ohta, Y., Taruya, A., Suto, Y., Narita, N., Turner, E.L., Johnson, J.A., Marcy, G.W., Butler, R.P., & Vogt, S.S. 2005, ApJ, 631, 1215

Winn J. N., Fabrycky D., Albrecht S., & Johnson J. A., 2010, ApJ, 718, L145

Winn, J. N., Howard, A. W., Johnson, J. A., et al. 2011, AJ, 141, 63

Wu, Y., & Murray, N. 2003, ApJ, 589, 605

Wu, Y., & Lithwick, Y. 2011, ApJ, 735,109

Xue, Y., Suto, Y., Taruya, A., Hirano, T., Fujii, Y., & Masuda, K. 2014, ApJ, 784, 66

Xue, Yuxin & Suto, Yasushi, 2016, ApJ, 820, 55

Xue, Y., Masuda, K., & Suto, Y. 2016, ApJ, Accepted

Zhang, K., & Hamilton, D. P. 2008, Icarus, 193, 267